In-medium nuclear interactions of low-energy hadrons *

E. Friedman[†1] and A. Gal[‡1]

[1]*Racah Institute of Physics, The Hebrew University, Jerusalem 91904, Israel*

(Dated: February 1, 2008)

Abstract

Exotic atoms provide a unique laboratory for studying strong interactions and nuclear medium effects at zero kinetic energy. Experimental and theoretical developments of the last decade in the study of exotic atoms and some related low-energy reactions are reviewed. The exotic atoms considered are of π^-, K^-, $\bar{p}$, Σ^-, and also the so far unobserved Ξ^- atoms. The analysis of these atomic systems consists of fitting density dependent optical potentials $V_{\rm opt} = t(\rho)\rho$ to comprehensive sets of data of strong-interaction level shifts, widths and yields across the periodic table. These provide information on the in-medium hadron-nucleon t matrix $t(\rho)$ over a wide range of densities up to central nuclear densities. For pions the review focuses on the extraction of the πN in-medium s-wave interaction from pionic atoms, which include also the recently observed at GSI deeply bound π^- atomic states in isotopes of Sn and Pb. Also included are recent measurements at PSI of elastic scattering of $\pi^\pm$ on Si, Ca, Ni and Zr at 21.5 MeV. The experimental results are analyzed in the context of chirally motivated π-nuclear potentials, and the evidence for partial restoration of chiral symmetry in dense nuclear matter is critically discussed. For antikaons we review the evidence from K^- atoms, and also from low-energy K^-p scattering and reaction data for and against a *deep* $\bar{K}$-nucleus potential of 150-200 MeV attraction at nuclear matter density. The case for relatively narrow deeply bound K^- *atomic* states is made, essentially independent of the potential-depth issue. Recent experimental suggestions from KEK and DAΦNE (Frascati) for signals of $\bar{K}$-nuclear deeply bound states are reviewed, and dynamical models for calculating binding energies and widths of $\bar{K}$-*nuclear* states are discussed. For kaons we review the evidence, from K^+ total and reaction cross section measurements at the AGS (BNL) on Li, C, Si and Ca at $p_{\rm lab} = 500 - 700$ MeV/c, for significant absorptivity of $t_{KN}(\rho)$ beyond that expected from $t_{KN}^{\rm free}$ within the impulse approximation. Attempts to explain the extra absorptivity for the relatively weak interaction of K mesons in terms of a hypothetical exotic $S = +1$ pentaquark Θ^+ strength are reviewed. For antiprotons the exceptionally broad data base due to the recent results of the PS209 collaboration at CERN are analyzed, together with results of radiochemical experiments. We discuss the dependence of the phenomenological $\bar{p}$-nucleus interaction on the model adopted for the neutron density, showing how the neutron densities favored by our comprehensive analysis are compatible with densities from other sources, including our own analysis of pionic atoms. It is also shown how the strong absorptivity of the $\bar{p}$-nucleus interaction, which leads to the prediction of saturation of widths in deeply-bound $\bar{p}$- atom states, also explains the observed saturation effects in low-energy $\bar{p}$ annihilation on nuclei. For Σ hyperons we review the evidence, from continuum Σ^- hypernuclear (π^-, K^+) spectra obtained recently at KEK on C, Si, Ni, In and Bi, for substantial repulsion in the Σ-nucleus interaction, and the relationship to the inner repulsion established earlier from the density-dependence analysis of Σ^- atoms and by analyses of past $(K^-, \pi^\pm)$ AGS experiments.

* Physics Reports, in press

† email: elifried@vms.huji.ac.il

‡ email: avragal@vms.huji.ac.il

Lastly, for Ξ hyperons we review prospects of measuring X-ray spectra in Ξ^- atoms and thereby extracting meaningful information on the Ξ-nucleus interaction. The significance of the latter to the physics of $\Lambda\Lambda$ hypernuclei and to extrapolation into multistrange hypernuclei are briefly reviewed.

PACS numbers: 24.10.Ht; 36.10.Gv
Keywords: Exotic atoms; Optical potential; Strong interaction; Density dependence; In-medium interactions

Contents

I. INTRODUCTION

A. Preview

In 1997 we published together with Chris Batty a Physics Reports review *Strong Interaction Physics from Hadronic Atoms* [1] that has had a substantial impact on the progress made in the last decade on the study and understanding of in-medium nuclear interactions for various hadrons at low energy. The most spectacular advance on the experimental side has been perhaps the discovery and study of deeply bound pionic-atom states using the 'recoil-free' $(\mathrm{d}, {}^3\mathrm{He})$ reaction near the pion production threshold on isotopes of Sn and Pb at GSI. Another potentially promising advance, very recently, concerns the as yet weak evidence for the existence of deeply bound antikaon-nuclear states gathered from stopped K^- reactions studied at KEK and at DAΦNE, Frascati. These advances were triggered by, and have stimulated related theoretical work in which low-energy in-medium hadronic properties were considered in terms of a systematic chiral-perturbation expansion. This holds not only for pions, owing to their relatively small mass, but also for antikaons where the dominant effect of the $S = -1$ subthreshold quasi-bound state $\Lambda(1405)$ was treated by a unitarized coupled-channel approach based on chiral-perturbation expansion. Significant advances in the study of nuclear interactions of other hadrons at low energy, for kaons, antiprotons and Σ hyperons, have also been made. A good evidence for the wide interest within the nuclear physics and hadronic physics communities in these subjects is provided by the large number of recent topical reviews devoted to the overall theme of in-medium nuclear interactions of hadrons, including energy regimes higher than considered here. A representative list of such Reviews during the last five years covers the following subjects: *chiral symmetry in nuclei and dense nuclear matter* [2], *pions in nuclei, a probe of chiral symmetry restoration* [3], *chiral symmetry and strangeness at SIS energies* [4], *medium modifications of hadrons - recent experimental results* [5], *kaon production in heavy ion reactions at intermediate energies* [6], *nucleon and hadron structure changes in the nuclear medium and impact on observables* [7].

In the present Review we discuss and summarize the developments in understanding the in-medium properties of several hadron-nucleon systems at low energy as unraveled by our recent phenomenological studies and related ones by other authors in this field. This brief Preview subsection is followed by brief introductory subsections on wave equations and optical potentials, on nuclear densities, and on in-medium interactions.

B. Wave equations and optical potentials

The interaction of hadrons in nuclear medium of density ρ is traditionally described by a dispersion relation based on the Klein-Gordon (KG) equation

$$E^2 - \mathbf{p}^2 - m^2 - \Pi(E, \mathbf{p}, \rho) = 0 \ , \qquad \Pi = 2EV_{\rm opt} \ , \tag{1}$$

where $\Pi(E, \mathbf{p}, \rho)$ is the hadron self-energy, or polarization operator and $V_{\rm opt}$ is the optical potential of the hadron in the medium [8]. Here m, $\mathbf{p}$ and E are the rest mass of the hadron, its three-momentum and energy, respectively. For finite nuclei, and at or near threshold as applicable to most exotic-atom applications, Eq. (1) gives rise to the following KG equation:

$$\left[\nabla^2 - 2\mu(B + V_{\rm opt} + V_c) + (V_c + B)^2\right]\psi = 0 \quad (\hbar = c = 1) \tag{2}$$

where μ is the hadron-nucleus reduced mass, B is the complex binding energy and V_c is the finite-size Coulomb interaction of the hadron with the nucleus, including vacuum-polarization terms, added according to the minimal substitution principle $E \to E - V_c$. A term $2V_cV_{\rm opt}$ and a term $2BV_{\rm opt}$ were neglected in Eq. (2) with respect to $2\mu V_{\rm opt}$; the term $2BV_{\rm opt}$ has to be reinstated in studies of deeply-bound states.

The simplest class of optical potentials $V_{\rm opt}$ is the generic $t\rho(r)$ potential, which for underlying s-wave hadron-nucleon interactions assumes the form:

$$2\mu V_{\rm opt}(r) = -4\pi(1 + \frac{A-1}{A}\frac{\mu}{M})\{b_0[\rho_n(r) + \rho_p(r)] + \tau_z b_1[\rho_n(r) - \rho_p(r)]\} \ . \tag{3}$$

Here, ρ_n and ρ_p are the neutron and proton density distributions normalized to the number of neutrons N and number of protons Z, respectively, M is the mass of the nucleon and $\tau_z = +1$ for the negatively charged hadrons considered in the present Review[1]. In the impulse approximation, b_0 and b_1 are minus the hadron-nucleon isoscalar and isovector scattering lengths, respectively. Generally these 'one-nucleon' parameters are functions of the density ρ, but often the density dependence may be approximated by fitting effective values for b_0 and b_1 to low-energy data. Extensions to situations which require 'two-nucleon' terms representing absorption and dispersion on pairs of nucleons, or which are motivated by p-wave hadron-nucleon interactions, will be dealt with in the next section, for pionic atoms.

For scattering problems, the applicable form of the KG equation is given by:

$$\left[\nabla^2 + k^2 - (2\varepsilon_{\rm red}^{(A)}(V_{\rm c} + V_{\rm opt}) - V_{\rm c}^2)\right]\psi = 0 \tag{4}$$

in units of $\hbar = c = 1$, where k is the wave number in the center-of-mass (c.m.) system. For the simplest possible $t\rho$ s-wave term, the optical potential $V_{\rm opt}$ is of the form

$$2\varepsilon_{\rm red}^{(A)}V_{\rm opt}(r) = -4\pi F_A\{b_0[\rho_n(r) + \rho_p(r)] + \tau_z b_1[\rho_n(r) - \rho_p(r)]\} \ , \tag{5}$$

where $\varepsilon_{\rm red}^{(A)}$ is the c.m. reduced energy,

$$(\varepsilon_{\rm red}^{(A)})^{-1} = E_p^{-1} + E_A^{-1} \tag{6}$$

[1] $\tau_z = -2t_z$ for isodoublets and $-t_z$ for isotriplets, where t_z is the value of the z th projection of isospin for the hadron considered.

in terms of the c.m. total energies E_p for the projectile and E_A for the target, and

$$F_A = \frac{M_A\sqrt{s}}{M(E_A + E_p)} \tag{7}$$

is a kinematical factor resulting from the transformation of amplitudes between the hadron-nucleon and the hadron-nucleus c.m. systems. Here M_A is the mass of the target nucleus and $\sqrt{s}$ the total projectile-nucleon energy in their c.m. system. These forms of the potential and the equation take into account $1/A$ corrections, which is an important issue when handling light nuclear targets. The kinematical factor F_A reduces at threshold to the kinematical term $(1 + (1 - 1/A)\mu/M)$ appearing in Eq. (3) for the one-nucleon s-wave potential term in exotic-atom applications.

For Fermions, such as antiprotons or Σ hyperons, one might ask why the KG equation is here used in going into the relativistic domain instead of the Dirac equation. Indeed when interpreting experimental transition energies, in order to extract the strong interaction effects, it is essential to use the Dirac equation with finite size nuclear charge distribution and vacuum polarization terms, e.g. Ref. [9] for antiprotonic atoms. However, strong interaction effects are normally given as proper averages over the fine structure components. The use of the KG equation rather than the Dirac equation is numerically justified when fine-structure effects are negligible or are treated in an average way, as for the X-ray transitions considered here. The leading j dependence ($j = l \pm \frac{1}{2}$) of the energy for solutions of the Dirac equation for a point-charge $1/r$ potential goes as $(j + \frac{1}{2})^{-1}$, and on averaging it over the projections of j gives rise to $(l + \frac{1}{2})^{-1}$ which is precisely the leading l dependence of the energy for solutions of the KG equation. The higher-order contributions to the spin-orbit splitting are suppressed by $\mathrm{O}(Z\alpha/n)^2$ which, e.g., is of order 1% for the high-n X-ray transitions encountered for antiprotons. It was checked numerically for few typical cases that the spin-orbit averaged shifts and widths thus obtained differ by less than 1% from the $(2j+1)$-average of the corresponding quantities obtained by solving the Dirac equation. This difference is considerably smaller than the experimental errors placed on the measured X-ray transition energies and widths.

C. Nuclear densities

The nuclear densities are an essential ingredient of the optical potential. The density distribution of the protons is usually considered known as it is obtained from the nuclear charge distribution [10] by unfolding the finite size of the charge of the proton. The neutron distributions are, however, generally not known to sufficient accuracy. A host of different methods have been applied to the extraction of root-mean-square (rms) radii of neutron distributions in nuclei but the results are sometimes conflicting, e.g. Refs. [11, 12, 13, 14, 15, 16]. For many nuclei there is no direct experimental information whatsoever on neutron densities and one must then rely on models. To complicate things further we note that there is a long history of conflict between values of neutron rms radii derived from experiments using hadronic projectiles and neutron rms radii obtained from theoretical calculations. For that reason we have adopted a semi-phenomenological approach that covers a broad range of possible neutron density distributions.

Experience with pionic atoms showed [17] that the feature of neutron density distributions which is most relevant in determining strong interaction effects in pionic atoms is the radial

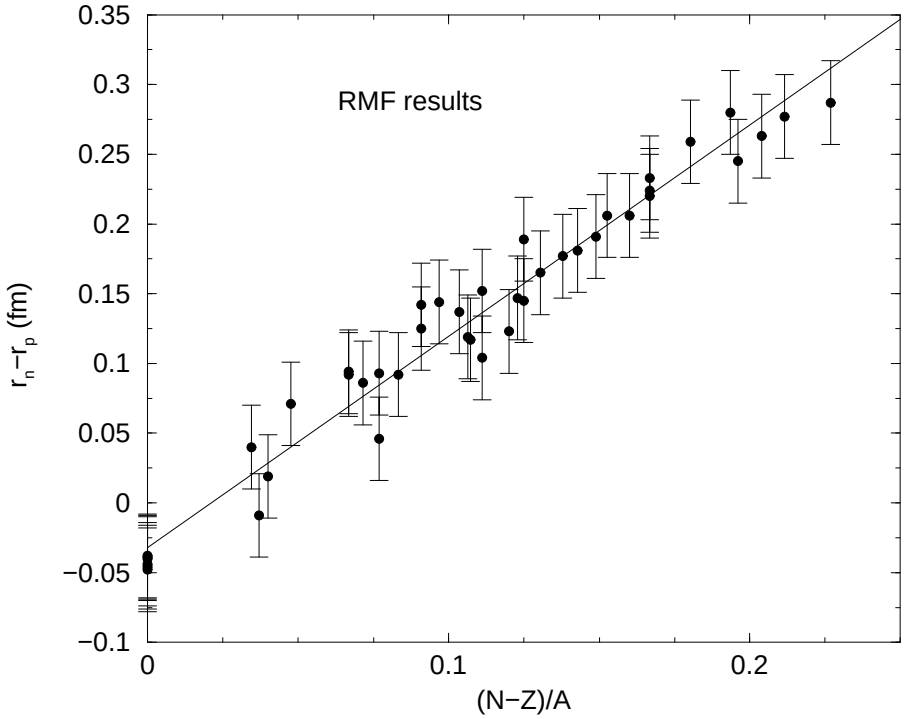

FIG. 1: Fit of a linear expression in the asymmetry parameter to RMF values of $r_n - r_p$.

extent, as represented e.g. by r_n, the neutron density rms radius. Other features such as the detailed shape of the distribution have only minor effect. For that reason we chose the rms radius as the prime parameter in the present study. Since r_p, the rms radius for the proton density distribution, is considered to be known, we focus attention on values of the difference $r_n - r_p$. A linear dependence of $r_n - r_p$ on $(N - Z)/A$ has been employed in $\bar{p}$ studies [16, 18, 19], namely

$$r_n - r_p = \gamma \frac{N - Z}{A} + \delta \ , \tag{8}$$

with γ close to 1.0 fm and δ close to zero. The same expression with γ close to 1.5 fm was found [17] to represent well the results of relativistic-mean-field (RMF) calculations [20] for stable nuclei, as shown in Fig. 1, but these values of $r_n - r_p$ are larger by about 0.05-0.10 fm than the 'experimental' values in medium-weight and heavy nuclei used in recent relativistic Hartree-Bogoliubov (RHB) versions of mean-field calculations [21, 22]. Expression (8) has been adopted in the present work and, for lack of better global information about neutron densities, the value of γ was varied over a reasonable range in fitting to the data. This procedure is based on the expectation that for a large data set over the whole of the periodic table some local variations will cancel out and that an average behavior may be established. Phenomenological studies of in-medium nuclear interactions are based on such averages.

In order to allow for possible differences in the shape of the neutron distribution, the 'skin' and 'halo' forms of Ref. [18] were used, as well as an average between the two. Adopting a two-parameter Fermi distribution both for the proton (unfolded from the charge distribution) and for the neutron density distributions

$$\rho_{n,p}(r) = \frac{\rho_{0n,0p}}{1 + \exp((r - R_{n,p})/a_{n,p})} \ , \tag{9}$$

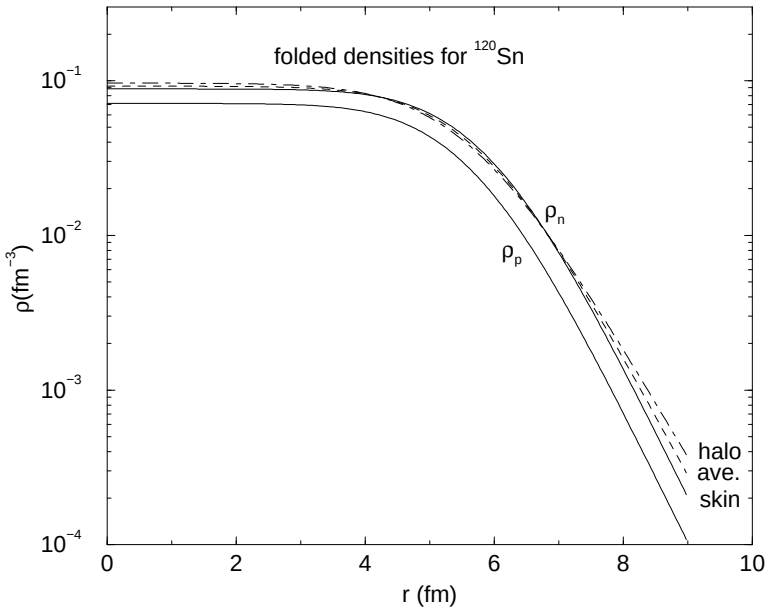

FIG. 2: Proton and neutron finite-range folded densities for ^{120}Sn with $\beta = 0.85$ fm. Neutron densities are calculated for $\gamma = 1.2$ fm, see Eqs. (8, 10).

then for each value of $r_n - r_p$ in the 'skin' form the same diffuseness parameter for protons and neutrons, $a_n = a_p$, was used and the R_n parameter was determined from the rms radius r_n. In the 'halo' form the same radius parameter, $R_n = R_p$, was assumed and $a_n^{\rm h}$ was determined from r_n. In the 'average' option the diffuseness parameter was set to be the average of the above two diffuseness parameters, $a_n^{\rm ave} = (a_p + a_n^{\rm h})/2$, and the radius parameter R_n was then determined from the rms radius r_n. In this way we have used three shapes of the neutron distribution for each value of its rms radius all along the periodic table. These shapes provide sufficient difference in order to be tested in global fits.

Another sensitivity that may be checked in global fits is to the radial extension of the hadron-nucleon interaction when folded together with the nuclear density. The resultant 'finite range' density is defined as

$$\rho^{\rm F}(r) \;\; = \;\; \int d\mathbf{r}'\rho(\mathbf{r}')\frac{1}{\pi^{3/2}\beta^3}e^{-(\mathbf{r}-\mathbf{r}')^2/\beta^2} \quad , \tag{10}$$

assuming a Gaussian interaction. Other forms such as a Yukawa function may also be used. Figure 2 shows for example finite-range folded proton and neutron densities in ^{120}Sn, calculated using the three models listed above for generating neutron densities. The difference between these three models becomes pronounced from about 8 fm on, a radial extent to which $\bar{p}$ atoms are particularly sensitive.

D. In-medium interactions

The $t\rho$ form of the optical potential, where t is the two-body hadron-nucleon t matrix and ρ is the nuclear density (more precisely, the nucleon-center distribution density), holds at high collision energy where most of the nuclear medium effects such as the Pauli principle are negligible. At low energy, and particularly near threshold, nuclear medium effects may and

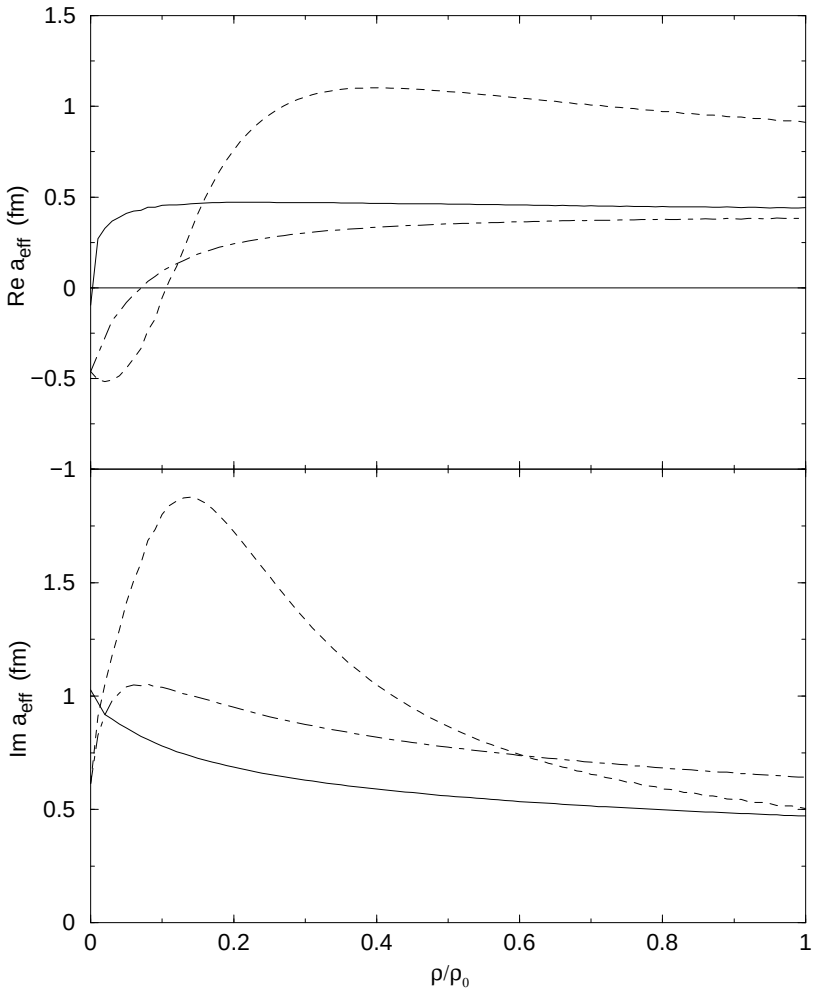

FIG. 3: Real (top) and imaginary (bottom) parts of the in-medium isospin-averaged K^-N (effective) threshold scattering amplitude as function of density, calculated in Ref. [24] including the effects of the Pauli principle (dashed lines), plus the effect of self consistency for K^- propagation (dot-dashed lines), and also the effect of self consistency for N propagation (solid lines).

often do assume special importance. To demonstrate the scope of medium effects we use as an example the case of K^- nuclear interaction near threshold ($\sqrt{s} \sim m_{K^-} + M_p = 1432$ MeV), for which the underlying two-body $\bar{K}N$ system is strongly coupled to the $\pi\Sigma$ and $\pi\Lambda$ reaction channels, all in s waves. In particular, the interaction in the $I = 0$ $\bar{K}N$-$\pi\Sigma$ coupled-channel system is so strong as to generate a subthreshold quasibound $\bar{K}N$ state about 27 MeV below threshold with a width approximately 50 MeV. This $\Lambda(1405)$ is observed as a resonance in $\pi\Sigma$ final-state interaction spectra [23]. The K^- nuclear optical potential in the large A limit, from Eq. (3), assumes the form:

$$2\mu V_{\rm opt}(r) = -4\pi(1 + \frac{\mu}{M})[a_{K^-p}(\rho)\rho_p(r) + a_{K^-n}(\rho)\rho_n(r)] \ , \tag{11}$$

where

$$a_{K^-p} \ = \ b_0 \ - \ b_1 \ , \quad a_{K^-n} \ = \ b_0 \ + \ b_1 \tag{12}$$

in the particle basis. The density dependent effective scattering amplitudes $a_{K^-p}(\rho)$, $a_{K^-n}(\rho)$ are complex due to the coupling to the reaction channels. For $\rho \to 0$, the low-density limit asserts their limiting values a_{K^-p}, a_{K^-n} respectively, where the latter are (strictly speaking minus) the corresponding scattering lengths. Figure 3 shows the density dependence of the *effective* isoscalar threshold scattering amplitude $a_{\rm eff} = \frac{1}{2}[a_{K^-p}(\rho) + a_{K^-n}(\rho)]$ for three cases: (*i*) no medium effects beyond Pauli blocking are included (dashed line); (*ii*) a self-consistent calculation including the $\bar{K}$ self energy (dot-dashed line); and (*iii*) including also the nucleon self energy (solid line). The change of the sign of Re$a_{\rm eff}$ from negative to positive corresponds to the transition from an apparently repulsive free-space interaction to an attractive one in the nuclear medium. The underlying physics is that the Pauli principle suppresses the contribution from Pauli forbidden intermediate states, thus weakening the in-medium t matrix which no longer supports a subthreshold quasibound state; thus, the $\Lambda(1405)$ gets pushed up above threshold [25, 26]. The inclusion of $\bar{K}$ and N (self energy) medium modifications pushes this transition to a lower density, as first shown by Lutz [27], but the free-space ($\rho = 0$) threshold scattering amplitude remains negative, reflecting the dominance of the $\Lambda(1405)$ $I = 0$ subthreshold resonance. The figure shows that apart from the very low density regime, the K^- optical potential $V_{\rm opt} = t(\rho)\rho$ evaluated within such self consistent models is well approximated over a wide range of densities by a $t_{\rm eff}\rho$ form, where $t_{\rm eff} = -(2\pi/\mu)(1 + \mu/M)a_{\rm eff} = {\rm const}$. A genuine ρ dependence of $t_{\rm eff}$ appears only at very low densities. The strength of Re$a_{\rm eff}$ is seen to be reduced to about 50% of its initial value upon imposing self consistency. This is due to the suppressive effect of Im$t_{\rm eff}$ in the K^- propagator of the Lippmann-Schwinger equation for $t(\rho)$:

$$t = v + v\frac{1}{E - H^{(0)}_{\rm mB} - t\rho - V_N + {\rm i}0}t \ . \tag{13}$$

Here v and t are coupled-channel meson-baryon (mB) potential and t matrix, respectively, and $H^{(0)}$ is the corresponding kinetic energy operator which depends implicitly on the density ρ through the imposition of the Pauli principle in $\bar{K}N$ intermediate states. The K^- optical potential $t\rho$ and the nucleon potential V_N act only in $\bar{K}N$ intermediate states. A sizable Imt leads to an exponential decay of the propagator $(E - H^{(0)}_{\rm mB} - t\rho - V_N + {\rm i}0)^{-1}$, so that $t \approx v$ thus losing the cooperative coupling effect to the πY channels in higher-order terms of v.

II. EXPERIMENTAL BACKGROUND

In this section we outline experimental results, relevant to the topic of the present work, that have been obtained since the publication of Ref. [1] which was focused on the strong interaction physics involved in exotic atoms of mostly medium weight and heavy nuclei. As before, most of the information on the interaction of low energy hadrons with nuclei which provides insight to in-medium properties, comes from strong interaction effects in exotic atoms. Here we include only a brief reminder of exotic atoms, referring to other reviews for more details [1, 28].

An exotic atom is formed when a negatively charged particle stops in a target and is captured by a target atom into an outer atomic orbit. It will then emit Auger electrons and characteristic X-rays whilst cascading down its own sequence of atomic levels until, at some state of low principal quantum number n, the particle is absorbed due to its interaction with

the nucleus. The lifetimes of all the particles considered here, namely π^-, K^-, $\bar{p}$ and Σ^-, are much longer than typical slowing down times and atomic time scales. Therefore, following the stopping of the hadron in matter, well-defined states of an exotic atom are established and the effects of the hadron-nucleus strong interaction can be studied. The overlap of the atomic orbitals with the nucleus covers a wide range of nuclear densities thus creating a unique source of information on the density dependence of the hadronic interaction.

In the study of strong interaction effects in exotic atoms, the observables of interest are the shifts (ϵ) and widths (Γ) of the atomic levels caused by the strong interaction with the nucleus. These levels are shifted and broadened relative to the electromagnetic case but the shifts and widths can usually only be measured directly for one, or possibly two levels in any particular exotic atom. The broadening due to the nuclear absorption usually terminates the atomic cascade at a low value of the radial quantum number n, thus limiting the experimentally observed X-ray spectrum. In some cases the width of the next higher $n+1$ 'upper' level can be obtained indirectly from measurements of the relative yields of X-rays when they depart from their purely electromagnetic values. Shifts and widths caused by the interaction with the nucleus may be calculated by adding an optical potential to the Coulomb interaction. The study of the strong interaction in exotic atoms thus becomes the study of this additional potential. On the experimental side, studies of strong interaction effects in exotic atoms have been transformed over the years with the introduction of increasingly more advanced X-ray detectors and with increasing the efficiency of stopping the hadrons, such as with a cyclotron trap [28]. In recent years exotic atom physics has turned into precision science.

With the present topic of in-medium interactions of low energy hadrons we include not only data on exotic atoms but also data on the interaction of hadrons with nuclei at low kinetic energies where the interaction models have similarities to the models used with exotic atoms. In such cases features of the interaction may be studied across threshold, thus enhancing our knowledge of the hadron-nucleus interaction. Moreover, the respective free hadron-nucleon interactions at very low energies are obviously the reference to which the in-medium interactions have to be compared. Therefore key experiments on those more elementary reference systems will also be mentioned in the present section.

Starting with pions, recent years have seen the continuation of experiments at PSI on pionic hydrogen and pionic deuterium, with ever increasing sophistication and efficiency, reaching accuracies which are limited by theoretical corrections [29]. Pionic atoms of deuterium are obviously the source of knowledge on the pion-neutron interaction, which is a pre-requisite for studies of heavier targets and for obtaining separately the isoscalar and the isovector interactions. The use of deuterium for this purpose inevitably introduces some dependence on models in the extraction of the two basic interactions.

Turning to heavier pionic atoms, the last decade has been dominated by the experimental observation of 'deeply-bound' pionic atom states in the recoil-free (d,^{3}He) reaction [30] which populates such states from 'inside' the nucleus. With this technique one avoids the cut-off imposed by nuclear absorption on the usual process of X-ray emission during the atomic cascades. The observation of these states in isotopes of Pb and Sn [31] made it possible to test predictions of interaction models which were based on data for conventional pionic atom states. Alternatively, it became possible to derive interaction parameters from deeply bound atomic states, for comparisons with models based on X-ray data. Moreover, studies of several isotopes of a single element have the promise of providing information on the role played by neutron density distributions in the pion-nucleus interaction.

Motivated by the renewed interest in the pion-nucleus interaction at very low energy, caused by the observation of deeply-bound states and by the possibility of linking the long-standing s-wave 'anomaly' with aspects of chiral-symmetry restoration (see below), differential cross sections for the elastic scattering of both π^+ and π^- by several target nuclei were measured at 21 MeV. A dedicated experiment [32, 33] where both charge states of the pion were measured with the same setup and where absolute normalizations were provided by muon scattering, yielded angular distributions which could be analyzed with the same interaction models as used for pionic atoms, thus providing tests across thresholds of various characteristics of the pion-nucleus interaction.

Turning to kaonic atoms, significant progress has been made with kaonic hydrogen, due to experiments with precision greatly exceeding that of the earlier generation experiments that removed the so-called kaonic hydrogen 'puzzle', where the strong interaction shift appeared initially to be attractive, contrary to expectations. The experiments at KEK [34] showed that the shift of the $1s$ level in kaonic hydrogen is repulsive, as expected from earlier phase-shift analyses. More recent results from DAΦNE [35], using the unique low energy K^- and K^+ from ϕ decay, are barely consistent with the KEK results within error bars. In addition, experiments at KEK on kaonic atoms of ^{4}He [36] seem to produce results quite different from the previous ones, which were at variance with predictions of most calculations. With the exception of the above two examples, the world's data on kaonic atoms have not been expanded in the last decade, because low energy K^- beams of sufficient quality are not available.

Outside the realm of kaonic atoms, there have been experimental indications [37, 38, 39, 40] of possible existence of strongly bound antikaon states in *nuclei*. These caused renewed interest in the question of the depth of the real part of the K^--nucleus potential at threshold, where 'deep' real potentials are known from χ^2 fits to kaonic atom data and 'shallow' potentials are obtained from chiral approaches. Although the experimental situation is not settled at the present time, some understanding of the antikaon-nucleus interaction is being promoted thanks to studies inspired by the speculations on strongly bound states.

The interaction of K^+ mesons with nuclei has not been discussed in our previous Review [1]. This topic is included in the present Review since further analyses of previous transmission experiments have clearly demonstrated [41, 42, 43] that the elementary KN interaction in the range of 500-700 MeV/c is modified in the nuclear medium. In common with the case of K^- mesons, the recent renewed interest in the topic of medium-modification of the elementary K^+ interaction was motivated by speculations based on experimental indications, in this case on the possible existence of the Θ^+ pentaquark.

The large cross sections for annihilation of antiprotons on nucleons set the scene for the interaction of $\bar{p}$ with nuclei at low energies. In terms of optical potentials that means dominance of the imaginary part which complicates the issue of the connection between the free $\bar{p}N$ interaction and the interaction in the nuclear medium. It also means that $\bar{p}$ do not penetrate deeply into nuclei. On the other hand, one of the experimental consequences is the ability to measure annihilation cross sections at extremely low energies. Indeed such measurements have been made in recent years at momenta as low as 40-50 MeV/c on light nuclei [44, 45] and on hydrogen [46]. Total cross sections for $\bar{n}p$ down to 50 MeV/c have also been reported [47].

The experimental situation with $\bar{p}$ atoms has changed significantly in the last decade with the publication by the PS209 collaboration [48] of high-quality data for several sequences of isotopes along the periodic table. For most target nuclei strong-interaction level shifts and

widths have been measured for two atomic levels of the same antiprotonic atom, with two examples where information is available for three levels. In addition close to 20 target nuclei have been studied by the radiochemical method [49, 50], observing the production of nuclei differing from the target nucleus by the removal of one neutron or one proton. Such data provide unique information on the absorption of $\bar{p}$ by a neutron or by a proton, repectively, at about 2.5-3 fm outside of the nuclear surface, and in particular the ratios between the probabilities for the two processes are determined quite reliably. The two kinds of data, namely, level shifts and widths on the one hand and ratios from radiochemical data on the other, were shown to lead to consistent results and could also be analyzed together.

Finally we mention the interaction of low energy Σ^- with nuclei. No additional data on Σ^- atoms have been produced in recent years and the only relevant new experimental information was obtained from the (π^-, K^+) reaction on nuclear targets [51] which showed some features in common with the Σ^- atom potential derived more than a decade earlier.

III. PIONS

A. The pion-nucleus potential

At zero energy the interaction of pions with nucleons is rather weak and consequently a $t\rho$ approach would be expected to yield a reasonably good optical potential or at least provide a theoretically motivated *form* for the potential. The interaction of low energy pions with nucleons is affected by the (3,3) resonance at about 180 MeV, and this is manifested by a significant p wave term in the πN interaction which in turn is reflected in the form of the optical potential [8]. The Kisslinger potential, where this p wave interaction leads to gradient terms in the pion nucleus potential, was introduced more than half a century ago [52] and model-independent analyses of elastic scattering of pions by nuclei showed [53] that indeed the local-equivalent potential has all the features expected for the Kisslinger potential (see also [54]). A $t\rho$ potential at zero energy is real because pions cannot be absorbed at rest by a single nucleon, although they can be absorbed by the nucleus. For that reason Ericson and Ericson [55] introduced ρ^2 terms into the potential which describe schematically the absorption of π^- on pairs of nucleons. The potential for π^- mesons then becomes, in its simplest form,

$$2\mu V_{\rm opt}(r) = q(r) + \vec{\nabla} \cdot \alpha(r) \vec{\nabla} \tag{14}$$

with

$$\begin{aligned} q(r) &= -4\pi(1+\frac{\mu}{M})\{b_0[\rho_n(r)+\rho_p(r)] + b_1[\rho_n(r)-\rho_p(r)]\} \\ &\quad -4\pi(1+\frac{\mu}{2M})4B_0\rho_n(r)\rho_p(r), \end{aligned} \tag{15}$$

$$\begin{aligned} \alpha(r) &= 4\pi(1+\frac{\mu}{M})^{-1}\{c_0[\rho_n(r)+\rho_p(r)] + c_1[\rho_n(r)-\rho_p(r)]\} \\ &\quad +4\pi(1+\frac{\mu}{2M})^{-1}4C_0\rho_n(r)\rho_p(r), \end{aligned} \tag{16}$$

where ρ_n and ρ_p are the neutron and proton density distributions normalized to the number of neutrons N and number of protons Z, respectively, μ is the pion-nucleus reduced mass

and M is the mass of the nucleon. In this potential $q(r)$ is referred to as the s wave potential term and $\alpha(r)$ is referred to as the p wave potential term. The real coefficients b_0 and b_1 are minus the pion-nucleon isoscalar and isovector s wave scattering lengths, respectively, whilst the real coefficients c_0 and c_1 are the pion-nucleon isoscalar and isovector p wave scattering volumes, respectively. The parameters B_0 and C_0 represent s wave and p wave absorptions, respectively, and as such have imaginary parts. Dispersive real parts are found to play a role in pionic atom potentials. The $\rho_n\rho_p$ in the absorption terms represent two-nucleon absorption which takes place predominantly on neutron-proton pairs. These were originally written [55] as $B_0\rho_m^2$ and $C_0\rho_m^2$, with $\rho_m = \rho_n + \rho_p$ without distinguishing between neutrons and protons. The factor 4 is introduced above to make the coefficients B_0 and C_0 comparable in the two formulations. In practice when parameters are obtained from fits to the data the two forms yield practically the same results.

In the above expressions the terms linear in the nuclear densities are associated, in the $t\rho$ approach, with the interaction between pions and free nucleons. Ericson and Ericson showed that the p wave dipole interaction is modified in the nuclear medium in a way analogous to the Lorentz-Lorenz effect in electrodynamics, replacing the above expression for $\alpha(r)$ as follows:

$$\alpha(r) \longrightarrow \frac{\alpha(r)}{1 + \frac{1}{3}\xi\alpha(r)} \tag{17}$$

where ξ is a constant of the order 1. This effect is generally referred to as the Lorentz-Lorenz-Ericson-Ericson (LLEE) effect and it results from short range repulsive correlations between nucleons. This modification should apply only to the linear part of α, and Eq. (16) is re-written as

$$\alpha(r) = \frac{\alpha_1(r)}{1 + \frac{1}{3}\xi\alpha_1(r)} + \alpha_2(r) \tag{18}$$

with

$$\alpha_1(r) = 4\pi(1 + \frac{\mu}{M})^{-1}\{c_0[\rho_n(r) + \rho_p(r)] + c_1[\rho_n(r) - \rho_p(r)]\} \tag{19}$$

$$\alpha_2(r) = 4\pi(1 + \frac{\mu}{2M})^{-1}4C_0\rho_n(r)\rho_p(r). \tag{20}$$

Another complication arises due to the parameter b_0 being exceptionally small. Hence second order effects in the construction of the isoscalar s wave potential term in $q(r)$ become important [55] and this causes b_0 to be replaced by

$$\overline{b}_0 = b_0 - \frac{3}{2\pi}(b_0^2 + 2b_1^2)k_F, \tag{21}$$

where k_F is the Fermi momentum calculated for the local nuclear density.

Finally there is another relatively small term of a kinematical origin whose presence is supported by fits to pionic atom data. This is the so-called angle transformation term [56, 57] which is given by

$$\begin{aligned} 2\mu\Delta V_{\rm opt} \;=\; & -4\pi\{\frac{\mu}{2M}(1 + \frac{\mu}{M})^{-1}\nabla^2[c_0(\rho_n + \rho_p) + c_1(\rho_n - \rho_p)] \\ & + \frac{\mu}{M}(1 + \frac{\mu}{2M})^{-1}\nabla^2[C_0\rho_n\rho_p]\}. \end{aligned} \tag{22}$$

TABLE I: Data for $1s$ states in pionic atoms

	shift (keV)	width (keV)	Ref.
^{20}Ne	-32.17 ± 0.77	15.43 ± 0.41	[60]
^{22}Ne	-40.42 ± 0.50	12.7 ± 3.5	[60]
Na	-50.6 ± 1.0	17.1 ± 1.6	[61]
^{24}Mg	-60.2 ± 1.2	24.3 ± 1.6	[62]
^{28}Si	-95.1 ± 2.0	41.0 ± 4.0	[62]
^{115}Sn	-2402 ± 24	441 ± 87	[31]
^{119}Sn	-2483 ± 18	326 ± 80	[31]
^{123}Sn	-2523 ± 18	341 ± 72	[31]
^{205}Pb	-5354 ± 61	764 ± 165	[63]

The above potential is inserted into the KG equation (2) to obtain a complex eigenvalue. The Coulomb potential due to the finite size charge distribution as well as the Uehling $\alpha(Z\alpha)$ vacuum polarization potential [58] are also included. The strong interaction effects are the differences between these eigenvalues with and without the above potential (Eq. (14)), respectively.

B. Pionic atom data

Experimental results on pionic atoms covering the whole of the periodic table have been published for a few decades, with improved accuracy over the years and with increased use of separated isotopes for targets. The most extensive analysis has been that of Konijn et al. [59] who analyzed 140 data points covering states from $1s$ in ^{10}B to $4f$ in ^{237}Np. We note that a different definition of the strong interaction shift is used in Ref. [59], namely, the difference between the complex binding energy for the full potential, including finite size Coulomb and vacuum polarization potential, and the binding energy for the point Coulomb potential. This is different from the conventional definition used here and, in any case, it breaks down for $1s$ states when the charge of the nucleus is $Z > 137/2$. Such data are available now for the $1s$ state in ^{205}Pb.

In the present work we are mostly concerned with global properties of the pion-nucleus interaction and its dependence on the nuclear density. This is effected by performing *global* fits to pionic atom data, handling together all relevant data. In order to avoid some distortion of the emerging picture we excluded from the analysis several deformed nuclei and also several very light nuclei, where the concept of an optical potential could be questionable. Moreover, we study extensively the dependence of strong-interaction effects on the neutron densities ρ_n, using two-parameter Fermi distributions. For that reason we excluded from the data base also nuclei with $Z \leq 8$ where other densities such as a modified harmonic oscillator are more appropriate.

The data used in the present work are summarized in the following four tables. The number of data points is 100, compared to 54 points used in our previous Review [1]. Ten of the points are due to the recently observed deeply bound states, as can be seen from the last four entries in Table I and the last line of Table II. These states are discussed below.

TABLE II: Data for $2p$ states in pionic atoms

	shift (keV)	width (keV)	Ref.
^{24}Mg	0.129 ± 0.004	0.0725 ±0.0018	[62]
^{26}Mg	0.126 ± 0.004	0.0811 ±0.0019	[64]
^{28}Si	0.286 ± 0.010	0.192 ±0.009	[62]
^{30}Si	0.281 ± 0.010	0.196 ±0.008	[64]
S	0.615 ± 0.022	0.430 ±0.021	[65]
^{40}Ca	1.941 ± 0.080	1.590 ±0.023	[66]
^{42}Ca	1.650 ± 0.080	1.65 ±0.15	[67]
^{44}Ca	1.583 ± 0.080	1.60 ±0.07	[67]
^{48}Ca	1.295 ± 0.115	1.64 ±0.11	[67]
^{46}Ti	2.490 ± 0.140	2.39 ±0.15	[67]
^{48}Ti	2.290 ± 0.130	2.62 ±0.15	[67]
^{50}Ti	1.937 ± 0.110	2.15 ±0.27	[67]
^{50}Cr	3.560 ± 0.210	4.3 ±0.4	[68]
^{52}Cr	3.120 ± 0.190	3.85 ±0.21	[68]
^{54}Cr	2.827 ± 0.190	3.84 ±0.29	[68]
Fe	4.468 ± 0.340	6.87 ±0.21	[65]
Ge	5.5 ± 0.9	18.5 ±2.5	[69]
As	4.6 ± 0.9	14.5 ±4.0	[69]
Nb	2.1 ± 3.0	64 ± 8	[62]
Ru	−27.6 ± 7.0	77 ±24	[62]
^{205}Pb	−835 ± 45	321 ±61	[63]

C. Deeply bound pionic atom states

.

As mentioned in Sec. II, the last decade has been dominated, for pionic atoms, by the observation of deeply bound states, which contributed to the revival of interest in pionic atoms in general and in the πN in-medium interaction in particular. We therefore include here a brief outline of this topic.

The term deeply bound pionic atoms refers to $1s$ and $2p$ states in heavy pionic atoms which cannot be populated via the X-ray cascade process because upper levels such as the $3d$ are already broadened by the strong interaction to the extent that the radiative yield becomes exceedingly small. The first to show that $1s$ and $2p$ states in heavy pionic atoms, perhaps surprisingly, are so narrow as to make them well defined, were Friedman and Soff [75]. They calculated numerically binding energies and widths for pionic atom states well beyond the experimentally reachable region using optical potential parameters [76] which reproduced very well experimental results over the entire periodic table. Figure 4 is the original figure from 1985 (Ref. [75]) showing the calculated binding energies (B) and widths (Γ) for $1s$ states of pionic atoms as function of the atomic number Z. It is seen that up to the top end of the periodic table the widths of the states are relatively small.

The explanation of that unexpected results was also given by Friedman and Soff [75] in terms of the overlap of the atomic wavefunction with the nucleus. The atomic wavefunctions of these deeply bound states are excluded from the nucleus due to the repulsive s wave part of the potential such that their overlap with the imaginary part of the potential becomes

TABLE III: Data for $3d$ states in pionic atoms

	shift (keV)	width (keV)	Ref.
Nb	0.761 ±0.020	0.402 ±0.016	[62]
Ru	1.428 ±0.080	0.75 ±0.08	[62]
Ag	1.99 ±0.05	1.43 ±0.04	[62]
Cd	2.23 ±0.09	1.65 ±0.07	[62]
Ba	5.44 ±0.27	4.3 ±0.9	[70]
^{140}Ce	7.05 ±0.30	5.6 ±1.0	[70]
^{142}Ce	7.23 ±0.30	6.5 ±0.9	[70]
^{148}Nd	7.85 ±0.40	8.8 ±1.2	[71]
^{150}Nd	7.77 ±0.40	9.2 ±1.1	[71]
^{166}Er	17.4 ±1.0	19.7 ±0.9	[72]
^{168}Er	16.3 ±0.5	19.4 ±1.0	[72]
Pt	28.8 ±1.9	37 ±5	[73]
^{208}Pb	32.25 ±2.40	47 ±4	[73]
Bi	30.5 ±3.0	52 ±4	[73]

TABLE IV: Data for $4f$ states in pionic atoms

	shift (keV)	width (keV)	Ref.
^{168}Er	0.351 ±0.020	0.22 ±0.03	[74]
Re	0.76 ±0.04	0.41 ±0.05	[73]
Pt	1.13 ±0.04	0.59 ±0.05	[73]
^{208}Pb	1.72 ±0.04	0.98 ±0.05	[73]
Bi	1.83 ±0.06	1.24 ±0.09	[73]
U	5.08 ±0.20	3.65 ±0.65	[65]

very small. In this context it is instructive to note that for a Schrödinger equation the width of a state is given *exactly* (i.e. not perturbatively) by the following expression

$$\Gamma = -2\frac{\int |\psi|^2 \,\mathrm{Im}V_{\mathrm{opt}} d\mathbf{r}}{\int |\psi|^2 \, d\mathbf{r}}. \tag{23}$$

A slightly different expression is obtained for the KG equation. It is, therefore, easy to see that the reduced overlap of the atomic wavefunction with the nucleus, due to the repulsive real part of the s-wave term of the potential Eq. (15), provides a natural explanation of the numerically observed saturation of widths. Only for larger charge numbers, beyond the range of stable nuclei, the Coulomb attraction overcomes the s-wave repulsion, resulting in very large increase in the calculated widths.

Three years later Toki and Yamazaki also concluded that deeply bound pionic atom levels would be sufficiently narrow and therefore could be observed, and in addition discussed experiments that could populate such states [77]. After several unsuccessful attempts in various laboratories, it was realized that the key to success was the creation of a pion at rest (it appears that the first to suggest this approach, although in a different context, were Ericson and Kilian [78]). That requires 'recoil-free' kinematics, which for the (d,^{3}He) reaction on Pb creating a bound pion means a beam energy around 600 MeV. The experiment at

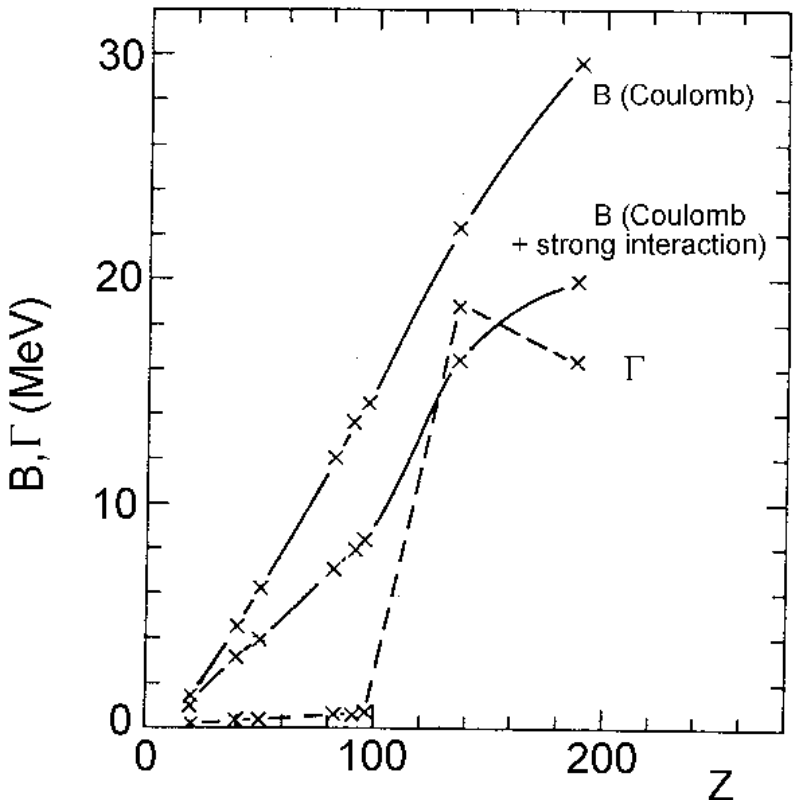

FIG. 4: Calculated binding energies and widths of $1s$ states in pionic atoms (from Ref. [75]).

GSI used the fragment separator in order to achieve the required resolution and reduction of background and the first observation of the $1s$ state in pionic atoms of ^{207}Pb by Yamazaki et al. [30] was a clear demonstration of the ability to study such states. Further experiments by the same group achieved improved accuracies for the $1s$ and $2p$ levels in pionic atoms of ^{205}Pb using a ^{206}Pb target [63] and studies of the $1s$ state in isotopes of Sn [31] followed soon after. Full details of this fascinating project can be found in a Review by Kienle and Yamazaki [3].

To conclude this section, Fig. 5 illustrates the phenomenon of saturation of widths in pionic atoms by showing calculated radiation and total widths of 'circular' states (i.e. states with radial number $n = l + 1$) in pionic atoms of Pb, using for the strong interaction the present-day best fit potential (see below). It is seen that for large l values the widths are essentially the radiative widths and X-ray transitions will be observed. As the l-value decreases the strong interaction width becomes significant and eventually, for low l values, the radiative transitions will be suppressed. However, the initial rise of the strong interaction width with decreasing l is saturated, resulting in the relatively narrow widths of deeply bound states. This is seen in Fig. 6 showing the energy spectrum for circular states of pionic atoms of Pb. Comparing with Fig. 5, it is clear that the energy levels are well-defined only thanks to the saturation of the widths.

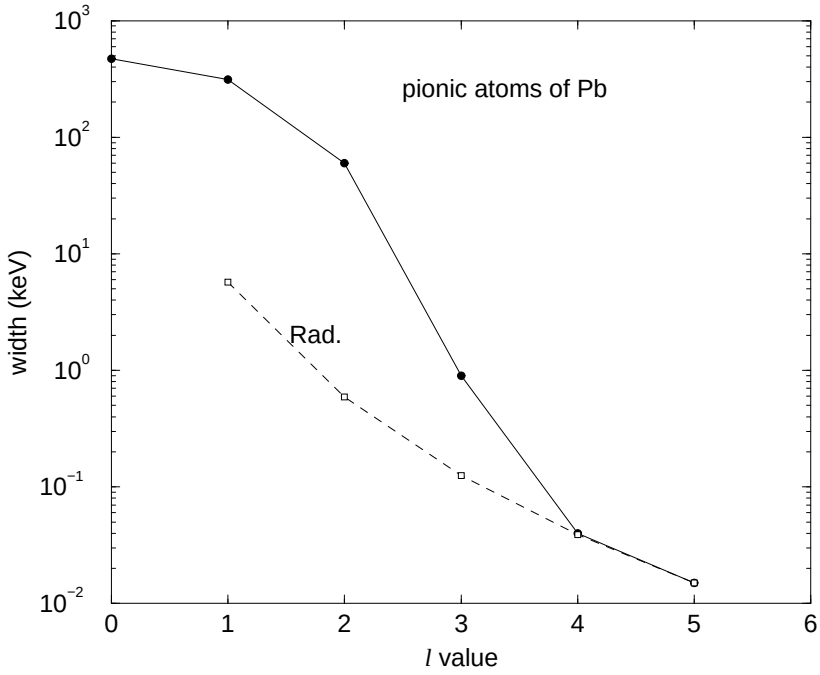

FIG. 5: Calculated widths of 'circular' states in pionic atoms of Pb, showing radiative (dashed) and total widths (solid line).

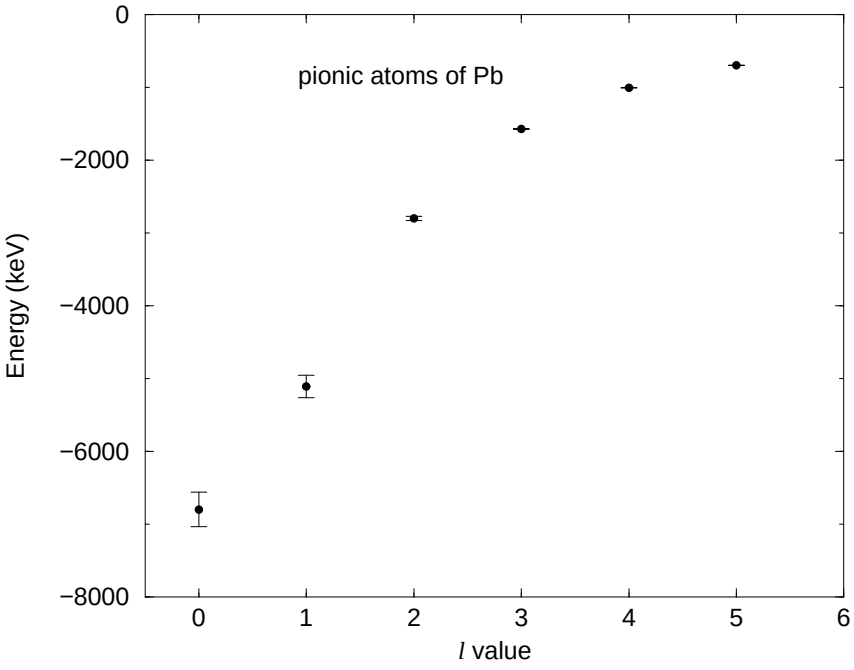

FIG. 6: Calculated energy levels of 'circular' states in pionic atoms of Pb. The bars show the widths of the states.

D. Fits to pionic atom data

1. General

With nine parameters in the pion-nucleus optical potential it is not a straightforward task to get meaningful information on the potential from χ^2 fits to the data. Moreover, there is the question of the proton ρ_p and neutron ρ_n density distributions which are an essential ingredient of the potential. The proton density distributions are known quite well from electron scattering and muonic X-ray experiments [10], and can be obtained from the nuclear charge distributions by numerical unfolding of the finite size of the proton. In contrast, the neutron densities are not known to sufficient accuracy and their uncertainties must be considered when extracting parameters from fits to the data.

Parameters of the pion-nucleus potential Eq. (14) had been obtained by performing χ^2 fits to the data already in the late 1970s and early 1980s and with the additional accumulation of data they were found to possess good predictive power of yet unmeasured quantities, with little dependence on the details of the potential form used to fit the data. Two approaches have been made to the problem of large number of free parameters: (i) assumptions can be made in order to reduce the number of free parameters, such as introducing 'effective' density in the quadratic terms [79] thus making them linear in the density and avoiding correlations with the corresponding genuinely linear terms; (ii) performing *global* fits to very large sets of data where the effects of correlations between parameters are reduced. In most cases the dependence on neutron densities have not been studied and 'reasonable' densities have been assumed in the analysis. Only García-Recio, Nieves and Oset [12] varied also neutron densities and obtained parameters for neutron distributions from global fits to pionic atoms data. Using three different versions for the pion-nucleus potential, they showed that the neutron rms radii were determined to good accuracy and were in reasonable agreement with values deduced from Hartree-Fock calculations. Below we present detailed studies of the dependence of derived potential parameters on neutron densities [80], with emphasis on the 's-wave anomaly' problem (see below).

Addressing first the p-wave part of the potential (Eq. (16)), we note that due to its gradient nature it is expected to be effective only in the surface region of nuclei and that large medium or density-dependent effects are not expected beyond the 'trivial' LLEE correction Eq. (17). As discussed in Ref. [1], the dependence of χ^2 on the parameters of the p-wave term is rather weak, with the free pion-nucleon scattering volumes of c_0=$0.21 m_\pi^{-3}$ and c_1=$0.165 m_\pi^{-3}$ being consistent with the best-fit values, when the 'classical' value of ξ=1.0 is being used. We therefore adopt these three values and focus most of the attention on the s wave part of the potential.

The role of the deeply bound states in the global picture of pion-nucleus interaction was an obvious question when the first such states were observed, and it was found [81] that shifts and widths of deeply bound states agreed with predictions made with potentials based on 'normal' states. That is fully understood by considering the overlaps between atomic and nuclear densities, which are very similar for normal and for deeply bound states, as can be seen e.g. from Fig. 17 of Ref. [3]. However, the experimental study of deeply bound states provides information on $1s$ states throughout the periodic table and has enriched our undertanding of the pion-nucleus interaction at low energies. Studies of isotopes have the potential of providing additional valuable information. In what follows we combine the data on deeply bound states with data on normal states, as is seen in Tables I and II.

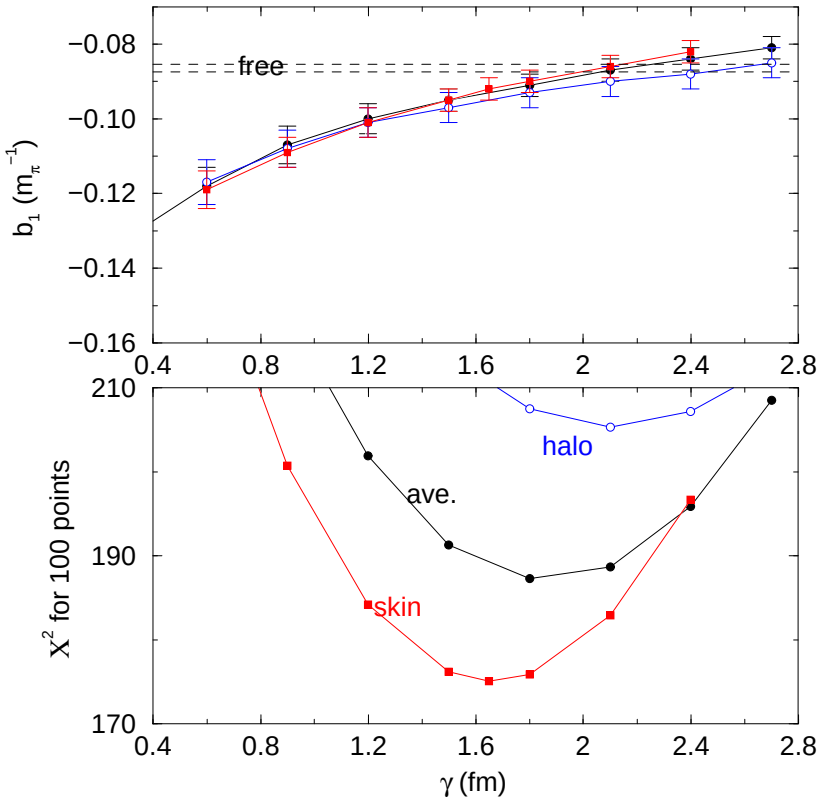

FIG. 7: Results of global fits to pionic atom data for different values of the neutron radius parameter γ of Eq. (8). Lower part - values of χ^2 for 100 data points for three shapes of the neutron density ρ_n. Upper part - the corresponding isovector parameter b_1 in comparison to its free πN value (marked 'free').

2. The role of neutron densities

As discussed in Sec. I C, r_p, the rms radius for the proton density distribution, is considered to be known and we therefore focus attention on values of the difference $r_n - r_p$, using the linear dependence of $r_n - r_p$ on $(N-Z)/A$ given by Eq. (8). In order to allow for possible differences in the *shape* of the neutron distribution, the 'skin' and the 'halo' forms of Ref. [18] were used, as well as their average, see Sec. I C.

Parameters of the potential Eq. (14) were determined by minimising the χ^2 in fits to the combined data given in tables I to IV. The linear p-wave parameters were held fixed at their respective free πN values of c_0=0.21m_π^{-3} and c_1=0.165m_π^{-3} and the LLEE parameter was held fixed at ξ=1. The quadratic p-wave parameters were found to be close to ReC_0=0.01m_π^{-6} and ImC_0=0.06m_π^{-6}. The neutron radius parameter δ was fixed at -0.035 fm and we scanned over the other radius parameter γ.

Figure 7 shows results of global fits to the 100 data points for pionic atoms, as discussed above. The lower part shows values of χ^2 as function of the parameter γ, as defined by Eq. (8). It is seen that the quality of fit depends on the shape of the neutron distribution, where the 'skin' shape is definitely preferred. The existence of quite well-defined minima is gratifying. The upper part shows the corresponding values of the isovector parameter b_1 in comparison with its free πN value (marked 'free'). It is clear that the resulting values

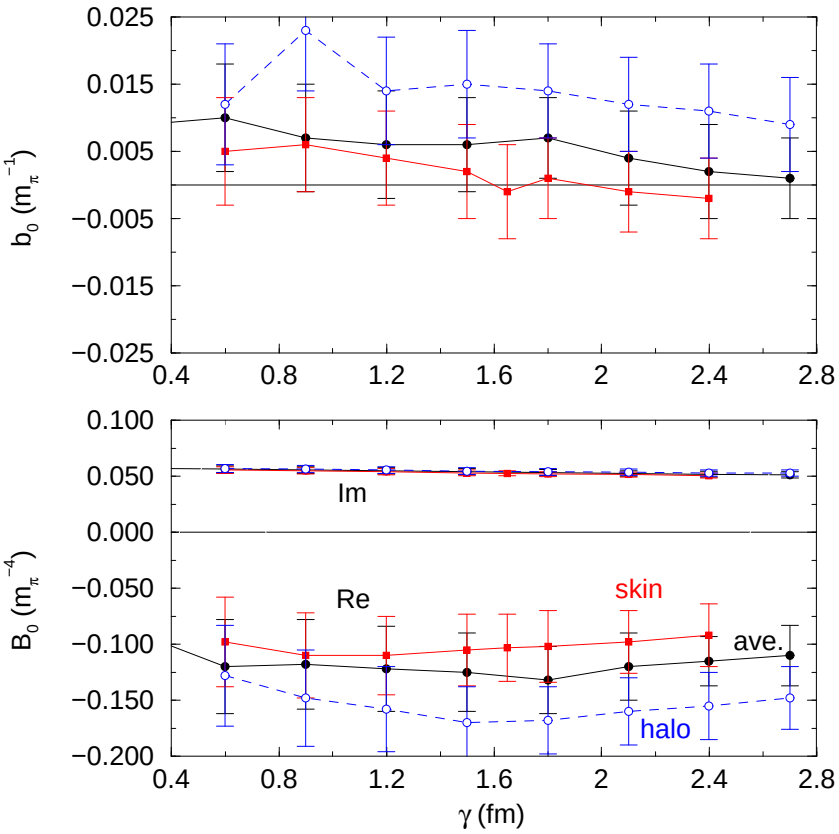

FIG. 8: Results of global fits for different values of the neutron radius parameter γ of Eq. (8). Lower part - the complex parameter B_0. Upper part - the isoscalar parameter b_0.

of b_1 are almost independent of the shape of the neutron density used in the fit, depending mostly on the values of the rms radius r_n, as represented by the parameter γ. From the figure one might conclude that for the best fit value of γ=1.6 fm the value of b_1 turns out to be in reasonable agreement with the free πN value.

Figure 8 shows in the upper part values of the isoscalar parameter b_0. As noted above, this parameter is exceptionally small and the errors on the best-fit results are relatively large. The lower part of the figure shows the resulting values of the quadratic parameter B_0. The values of ImB_0 are determined to a very good accuracy and are independent of the neutron radius parameter γ and of the shape of the distribution. The values of ReB_0 are not as accurate but they are clearly not zero, representing non-negligible repulsion in addition to the repulsion provided by the linear term.

The rms radii of neutron distributions implied by the global fits to pionic atom data need some attention, particularly in view of the fairly strong dependence of the derived *in medium* values of the isovector s-wave parameter b_1 on the rms radius assumed for ρ_n. As mentioned above, values of the difference $r_n - r_p$ between rms radii obtained for medium-weight and heavy nuclei with γ=1.5 fm are too large by 0.05 to 0.1 fm in comparison with recent RHB calculations [21, 22]. Moreover, a survey of different sources of information on $r_n - r_p$ suggests [16] that γ=0.9-1.0 fm is the proper value. Therefore the pionic atoms result of $\gamma \geq$1.6 fm is at odds with all we know about neutron density distributions in nuclei.

An obvious next step is to try some finite-range (FR) modification of the otherwise zero

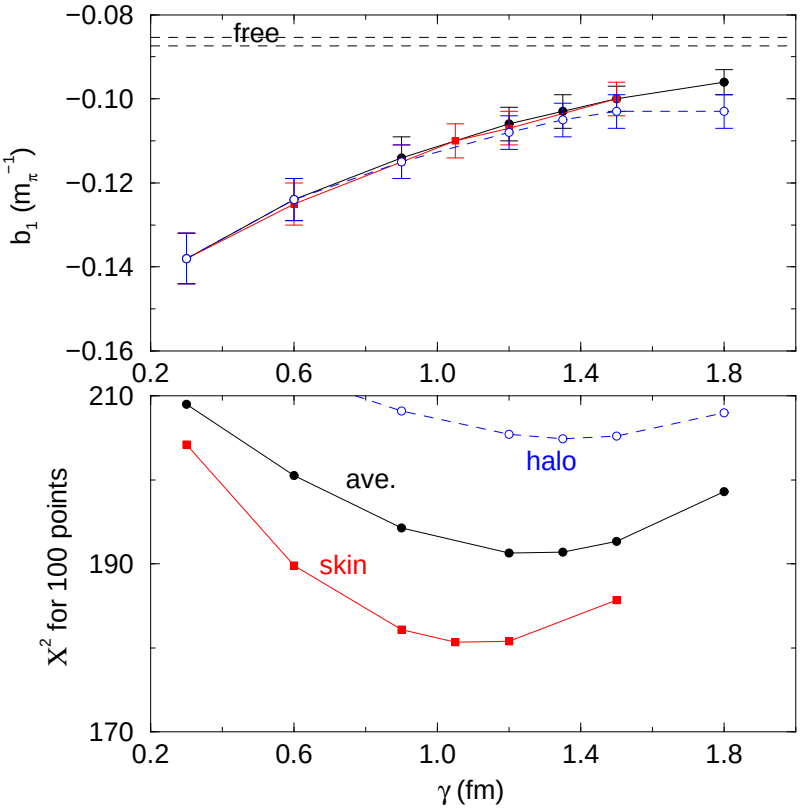

FIG. 9: Same as Fig. 7 but with finite range folding applied to the p-wave potential, see text.

range pion-nucleus potential. This can be achieved by folding the densities with e.g. a Gaussian such that each density ρ in the potential is replaced by a folded one ρ^F, see Eq. (10). It is found that when folded densities are used the χ^2 becomes a monotonic increasing function of the range parameter β. However, when folding is introduced separately into the s-wave and into the p-wave parts of the potential, then a minimum is obtained for χ^2 when the rms radius of the finite range function is 0.9±0.1 fm, provided FR is applied *only* to the p-wave term. The same results are obtained when a Yukawa FR function is used instead of the Gaussian. Figure 9 shows results of global fits to pionic atom data when a FR folding with rms radius of 0.9 fm is applied to the p-wave part of the potential. Comparing with Fig. 7 we note that again the 'skin' shape yields the best fit but now it is obtained for γ=1.1 fm, which is an acceptable value. However, the difference between b_1 and its free πN value is very large, representing a significant increased repulsion in the nuclear medium. Figure 10 is quite similar to Fig. 8 with non-zero values for ReB_0. Although there is no acceptable theory for the empirical parameter B_0, it is believed that the absolute value of its real part should be smaller than the imaginary part [82, 83], which is not the case here.

The present results mean that the in-medium s-wave repulsion, as obtained from global fits to pionic atom data, is significantly enhanced compared to expectations, partly via the extra repulsion provided by b_1 and partly by the dispersive ReB_0 being more repulsive than expected. The sum of these two effects is the well-known pionic atoms 'anomaly'. This is the most bias-free way of presenting the 'anomaly', or 'anomalous s-wave repulsion'.

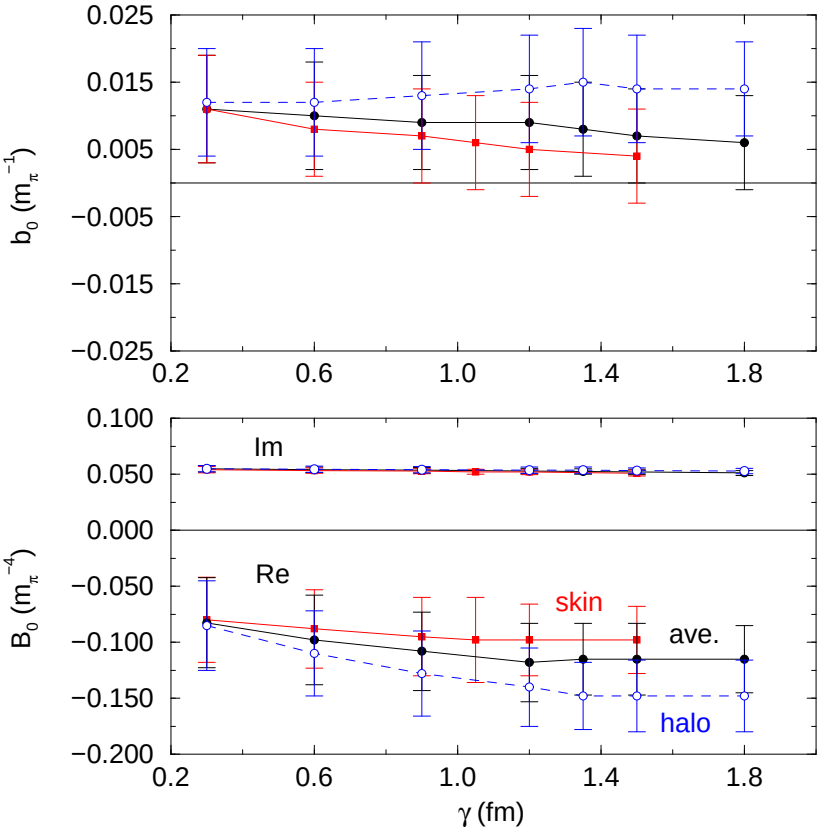

FIG. 10: Same as Fig. 8 but with finite range folding applied to the p-wave potential, see text.

3. The s-wave anomaly and the issue of chiral symmetry restoration

The so-called s-wave anomaly or the extra repulsion observed in fits to pionic atom data had been known for a very long time [1]. The previous section presented a state-of-the-art summary of this topic, based on global fits to 100 data points, respecting our knowledge on the $r_n - r_p$ rms radii difference and otherwise without additional assumptions. Global approaches always yielded the result that the extra repulsion observed in the phenomenological potential is due to two sources, namely, an enhanced b_1 coefficient and an unexpectedly large repulsion of the dispersive quadratic term, albeit with large uncertainty. An alternative approach, mainly due to Yamazaki and co-workers, has been to handle restricted data sets and to reduce the number of parameters in the potential by making some assumptions. Basically they used the approach of Seki and Masutani [79] where due to the correlations between b_0 and ReB_0 and the assumption of an average or an effective density, the two terms plus the isoscalar double-scattering contribution of Eq. (21) are lumped together, resulting in a single effective isoscalar real part linear in the density. Using the deeply bound $1s$ states in Sn isotopes (see Table I) together with $1s$ states in ^{16}O, ^{20}Ne and ^{28}Si, a total of 12 points, they obtain $b_1 = -0.1149 \pm 0.0074 m_\pi^{-1}$ (see Ref. [3] for full details.) This may be compared with the value of b_1 that corresponds to the minimum of χ^2 in Fig. 9 for the 'skin' shape of ρ_n, namely $b_1 = -0.109 \pm 0.005 m_\pi^{-1}$. The agreement between the two results is very good, and a significant discrepancy is thus established beyond any doubt with respect to the free πN value $b_1^f = -0.0864 \pm 0.0010 m_\pi^{-1}$ derived from the preliminary results of the

PSI measurement of the π^-H $1s$ level shift and width [84]. Note, however, the *conceptual* differences between the two methods:

- The Yamazaki et al. approach makes particular assumptions on the neutron densities of only few nuclides for $1s$ atomic states. In our global approach, where it is found that the major effect of the unknown neutron densities is through $r_n - r_p$, the $(N-Z)/A$ dependence of $r_n - r_p$ is an average over 36 nuclides spanning a full range of atomic states (from $1s$ to $4f$).

- Due to the use of 'effective density' as mentioned above, and $N = Z$ nuclei dominated by the isoscalar πN interaction, it is somewhat ambiguous in the Yamazaki et al. approach to determine b_0 and ReB_0 independently of each other. Thus, assuming $b_0 = 0$, they obtain Re$B_0 = -0.033 \pm 0.012 m_\pi^{-4}$ [Eq. (77) of Ref. [3]]. Our data base includes 100 rather than 12 points, where all are significant in determining parameters of the s-wave part of the potential since this part contributes large fractions of the strong interaction effects also for states with $l > 0$. Moreover, no assumptions are made regarding the terms nonlinear in density. In addition figure 10 shows that our deduced value of b_0 for the 'skin' shape for ρ_n is essentially in agreement with the free πN value $b_0^f = +0.0068 \pm 0.0031 m_\pi^{-1}$, deduced from the preliminary PSI results for the π^-H $1s$ level shift and width [84]. If this value were assumed in Ref. [3], then they would have derived a value of Re$B_0 = -0.064 \pm 0.012 m_\pi^{-4}$ agreeing within error bars with our values as depicted in Fig. 10.

A systematic study of the uncertainties in parameters of the potential and their dependence on the size of the data base and on assumptions made and constraints imposed in the analysis can be found in Ref. [17]. In what follows we focus attention on the in-medium values of b_1. It is shown below that eventually the problem with ReB_0 is also solved.

The renewed interest in recent years in the 'anomalous' s-wave repulsion in the pion-nucleus interaction at threshold, as found in phenomenological analyses of strong interaction effects in pionic atoms, is partly due to the suggestion by Weise [85, 86] that such enhancement could be expected, at least in the isovector channel, to result from a chirally motivated approach where the pion decay constant becomes effectively density dependent in the nuclear medium. Since b_1 in free-space is well approximated in lowest chiral-expansion order by the Tomozawa-Weinberg (TW) expression [87, 88]

$$b_1 = -\frac{\mu_{\pi N}}{8\pi f_\pi^2} = -0.08 m_\pi^{-1}\,, \tag{24}$$

with $\mu_{\pi N}$ the pion-nucleon reduced mass, then it may be argued that b_1 will be modified in pionic atoms if the free-space pion decay constant $f_\pi = 92.4$ MeV is modified in the medium. QCD coupled with PCAC relates f_π to the quark condensate $< \bar{q}q >$:

$$\frac{f_\pi^{*2}(\rho)}{f_\pi^2} = \frac{< \bar{q}q >_\rho}{< \bar{q}q >_0} \simeq 1 - \frac{\sigma\rho}{m_\pi^2 f_\pi^2}\,, \tag{25}$$

where σ is the πN sigma term and where the last step provides the leading term in a density expansion of the quark condensate [89] assuming that the charge-averaged pion mass does not change in the medium.[2] Thus f_π is expected to decrease in the nuclear medium by

[2] This holds for the temporal version of f_π, corresponding to the vacuum-to-pion matrix element of the time component of the axial current, c.f. Refs. [90, 91].

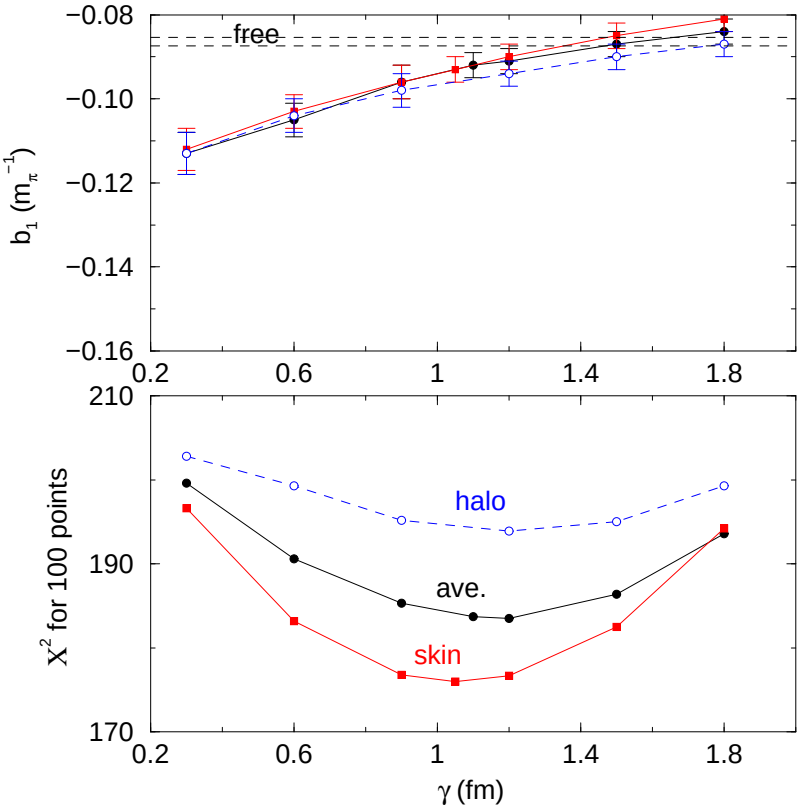

FIG. 11: Results of global fits for different values of the neutron radius parameter γ (Eq. (8)) with $b_1(\rho)$ given by Eq. (26). Lower part - values of χ^2 for 100 data points for three shapes of the neutron density ρ_n. Upper part - the corresponding isovector parameter b_1 in comparison to its free πN value (marked 'free').

about 20% at nuclear-matter density $\rho_0 \simeq 0.16$ fm^{-3}, using $\sigma \simeq 50$ MeV [92]. The form of Eq. (24) suggests then a density-dependent isovector amplitude such that b_1 becomes

$$b_1(\rho) = \frac{b_1(0)}{1 - \sigma\rho/m_\pi^2 f_\pi^2} = \frac{b_1(0)}{1 - 2.3\rho} \tag{26}$$

for σ=50 MeV and with ρ in units of fm^{-3}, resulting in an increase of b_1 in the nuclear medium by about 60% at nuclear-matter density $\rho_0 \simeq 0.16$ fm^{-3}. This ansatz [85, 86] was applied at almost the same time in two different analyses of pionic atom data. Kienle and Yamazaki [93] outlined a method for extracting b_1 from analyses of very limited data sets, which is essentially the method described above, but using a fixed average value of the density-dependent $b_1(\rho)$ of Eq. (26). Friedman [94] presented results of global analyses, as outlined above but with 60 data points compared to the present 100 points, using explicitly Eq. (26) for the density dependent $b_1(\rho)$. It was shown that indeed most of the difference between the derived b_1 and its free πN value disappeared when the above density dependence was included.

Figure 11 shows results of global fits to the 100 data points for pionic atoms, with $b_1(\rho)$ given by Eq. (26). The parameter b_1 stands here for $b_1(\rho = 0)$. It is seen that for the lowest minimum of χ^2, i.e. the minimum of the curve obtained for the 'skin' shape for the neutron density, b_1 is much closer to the free πN value than it was in Fig. 9 where a fixed b_1

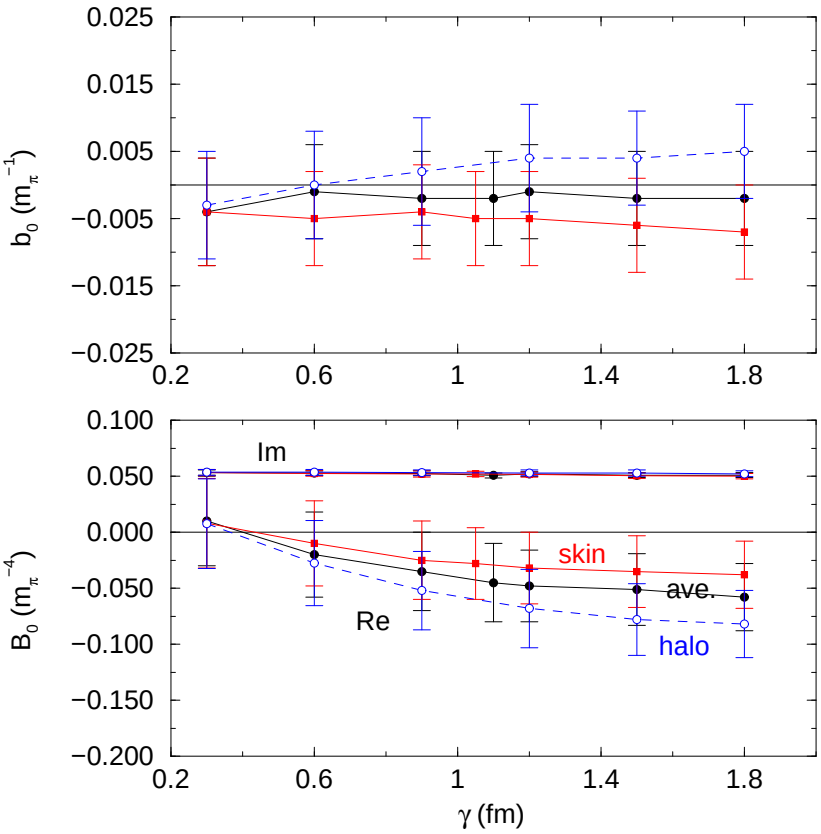

FIG. 12: Results of global fits for different values of the neutron radius parameter γ (Eq. (8)) with $b_1(\rho)$ given by Eq. (26). Lower part - values of the complex parameter B_0. Upper part - the resulting isoscalar parameter b_0.

was assumed, and they are almost in agreement. Figure 12 shows that b_0 now is consistent with zero and that ReB_0 is much less repulsive than before and is acceptable being almost consistent with zero.

The renormalization of f_π in dense matter, as given by Eq. (25) and leading to the related renormalization of the isovector amplitude b_1 in Eq. (26), may also be derived under simplifying assumptions by solving the KG equation in infinite nuclear matter of protons and neutrons for a pion chiral s-wave polarization operator $\Pi_s(E)$ near threshold [95, 96]. In chiral-perturbation theory, in the limit of vanishing m_π/M and for zero momentum pions, $\mathbf{q} = 0$, the leading terms to order $E/(4\pi f_\pi)$ of the πN s-wave amplitudes give rise to the following form of the s-wave pion polarization operator:

$$\Pi_s(E) = 2EV_{\rm opt}^{(s)}(E) \approx \tau_z \frac{E}{2f_\pi^2}(\rho_n - \rho_p) - \frac{(\sigma - \beta E^2)}{f_\pi^2}(\rho_p + \rho_n) \ , \tag{27}$$

where E is the pion energy including its rest mass m_π and $\tau_z = +1, 0, -1$ for π^-, π^0, π^+, respectively, in the notation of Eq. (3). The first, TW isovector term is the dominant one near threshold, providing repulsion for π^- for all nuclei with neutron excess. The second, isoscalar term is nearly zero at threshold, so it is reasonable to fit β by requiring $\beta = \sigma/m_\pi^2$. The polarization operator $\Pi_s(E)$ satisfies a KG equation (for $\mathbf{q} = 0$):

$$E^2 - m_\pi^2 - \Pi_s(E) = 0 \tag{28}$$

which by inserting Eq. (27) becomes

$$(1-\frac{\sigma\rho}{m_\pi^2 f_\pi^2})(E^2-m_\pi^2)-\tau_z\frac{E}{2f_\pi^2}(\rho_n-\rho_p)=0\,, \tag{29}$$

with $\rho=\rho_p+\rho_n$. When recast into the form

$$\Pi_s(E)=E^2-m_\pi^2=\tau_z\frac{E}{2f_\pi^{*2}}(\rho_n-\rho_p)\,, \tag{30}$$

with the effective density-dependent pion decay constant f_π^* defined by

$$f_\pi^{*2}=f_\pi^2\left(1-\frac{\sigma\rho}{m_\pi^2 f_\pi^2}\right)\,, \tag{31}$$

it is seen to be equivalent, at threshold, to Eqs. (24-26) with the renormalized effective pion decay constant f_π^*. Equation (30) strictly speaking is satisfied for one specific value of energy ('self energy') near threshold, $E\gtrsim m_\pi$. Approximating then $\Pi_s(E)$ by the right-hand side at $E=m_\pi$, the appearance of f_π^* instead of f_π may be attributed to a wave-function renormalization effect [95, 96].

Switching from infinite nuclear matter considerations to actual pionic-atom calculations, the finite-size Coulomb potential V_c needs to be introduced properly into a KG equation in which $\Pi_s(E)$ serves as a *given* input, not as an entity to solve Eq. (28) for. Schematically, Eq. (28) is replaced by

$$\left[(E-V_c)^2-m_\pi^2-\Pi_s(E-V_c)\right]\psi=0\,, \tag{32}$$

where the Coulomb potential V_c enters via the minimal substitution requirement [97], $\Pi_s(E)\to\Pi_s(E-V_c)$. When the chiral version of the s-wave pion polarization operator Eq. (27) was used in a KG equation of the type of Eq. (32), it was found in the global fits to pionic atom data reported in Ref. [98] that a large over-correction of b_1 occurred, to a value $b_1=-0.068\pm0.004 m_\pi^{-1}$, significantly less repulsive than b_1^f. In this case, it is the combined effect of the isoscalar and the isovector amplitudes that is responsible for over-shooting b_1^f. Therefore, although the effect of including the energy dependence of the $\mathbf{q}=0$ chiral amplitudes goes in the desired direction, it does not provide a quantitative resolution of the s-wave anomaly problem. Different results, and conclusions, are obtained when fits are made to partial data sets which may not carry sufficient statistical significance to decide one way or another on this issue [95, 96].

Friedman and Gal [98] discussed also an alternative procedure in which the empirical *on-shell* energy dependent πN amplitudes are used for implementing the minimal substitution requirement $E\to E-V_c$. As pointed out by Ericson [99] the on-shell approximation follows naturally for strongly repulsive short-range NN correlations from the Agassi-Gal theorem [100] for scattering off non-overlapping nucleons. The energy dependence of the 'empirical' amplitudes is weaker than that of the 'chiral' ones. For $b_1(E)$ there is hardly any energy dependence, in contrast to the energy dependence of the 'chiral' $b_1(E)$ which by itself would suffice to recover b_1^f, the free-space value of b_1, in the pionic-atom global fits. For $b_0(E)$ the empirical energy dependence is only about 60% of the 'chiral' effect. When this weaker empirical energy dependence of b_0 was used, the resulting b_1 was still too repulsive

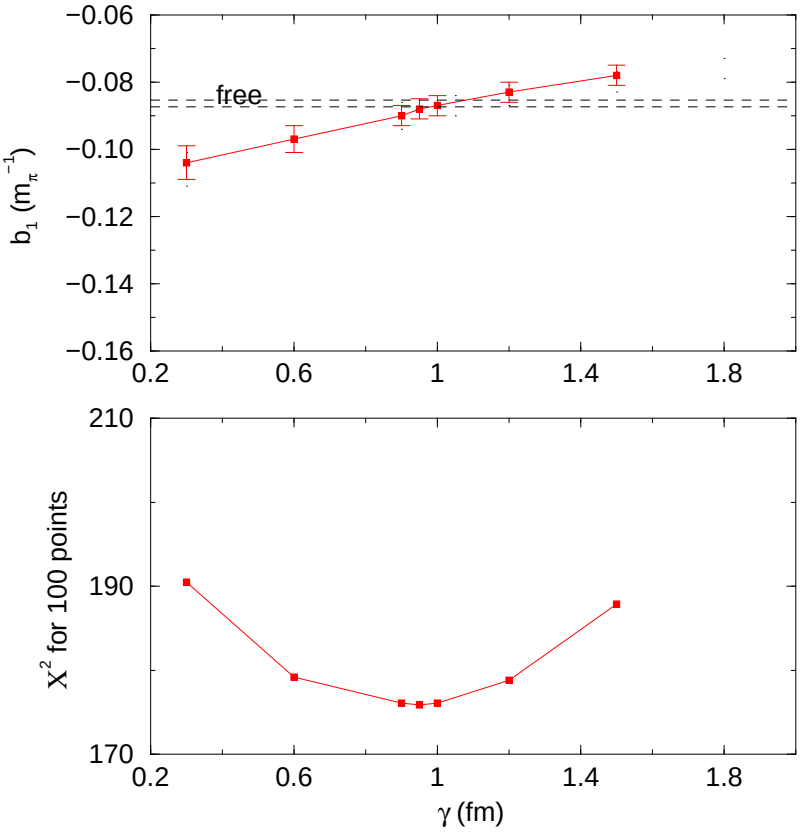

FIG. 13: Results of global fits for different values of the neutron radius parameter γ (Eq. (8)) with $b_1(\rho)$ given by Eq. (26) and the empirical energy dependence of the free $b_0(E)$ included. Lower part - values of χ^2 for 100 data points for the 'skin' shape of the neutron density ρ_n. Upper part - the corresponding isovector parameter b_1 in comparison to its free πN value (marked 'free').

in comparison with b_1^f, but closer to b_1^f than the b_1 resulting in the conventional fixed b_1 model.

Figure 13 is similar to Fig. 11 but with the energy dependence of the free πN b_0 included *in addition* to applying the density-dependent renormalization of Eq. (26) for b_1. Comparing with Fig. 11 the values of b_1 have shifted now and at the minimum of χ^2 the agreement with the free πN value is perfect. The resulting b_0 (not shown) of $b_0 = -0.009 \pm 0.007 m_\pi^{-1}$ is close to the free value and ReB_0 (not shown) is essentially zero at $-0.005 \pm 0.035 m_\pi^{-4}$. The chiral-motivated isovector $b_1(\rho)$ Eq. (26) together with the empirical energy dependence therefore provides all the required extra repulsion, with the isoscalar b_0 being essentially zero and with no significant dispersive ReB_0 term needed.

4. Radial sensitivity of pionic atoms

The chiral-motivated dependence of the isovector term b_1, as given by Eq. (26), almost completely removed the 'anomaly' observed when a fixed value was used for b_1. Not only with Eq. (26) does now one get for $b_1(0)$ the free πN value, but also the fit value of b_0 is very close to its free value and ReB_0 is zero. This is obtained without the need to introduce

'effective' density or to make any assumptions regarding ReB_0. It is concluded, therefore, that Eq. (26) is a fair representation of the medium-modification of the isovector term of $q(r)$, Eq. (15). It is instructive to examine further the radial sensitivity of this term.

The radial sensitivity of exotic atom data was addressed before [1] with the help of a 'notch test', introducing a local perturbation into the potential and studying the changes in the fit to the data as function of position of the perturbation. The results gave at least a semi-quantitative information on what are the radial regions which are being probed by the various types of exotic atoms. However, the radial extent of the perturbation was somewhat arbitrary and only very recently that approach was extended [101] into a mathematically well-defined limit.

In order to study the radial sensitivity of *global* fits to exotic atom data, it is necessary to define the radial position parameter globally using as reference e.g. the known charge distribution for each nuclear species in the data base. The radial position r is then defined as $r = R_c + \eta a_c$, where R_c and a_c are the radius and diffuseness parameters, respectively, of a 2pF charge distribution [10]. In that way η becomes the relevant radial parameter when handling together data for several nuclear species along the periodic table. The value of χ^2 is regarded now as a functional of a global optical potential $V(\eta)$, i.e. $\chi^2 = \chi^2[V(\eta)]$, where the parameter η is a *continuous* variable. It leads to [101, 102]

$$d\chi^2 = \int d\eta \frac{\delta\chi^2}{\delta V(\eta)} \delta V(\eta) \; , \tag{33}$$

where

$$\frac{\delta\chi^2[V(\eta)]}{\delta V(\eta')} = \lim_{\sigma\to 0} \lim_{\epsilon_V \to 0} \frac{\chi^2[V(\eta) + \epsilon_V \delta_\sigma(\eta - \eta')] - \chi^2[V(\eta)]}{\epsilon_V} \tag{34}$$

is the functional derivative (FD) of $\chi^2[V]$. The notation $\delta_\sigma(\eta - \eta')$ stands for an approximated δ-function and ϵ_V is a change in the potential. From Eq. (33) it is seen that the FD determines the effect of a local change in the optical potential on χ^2. Conversely it can be said that the optical potential sensitivity to the experimental data is determined by the magnitude of the FD. Calculation of the FD may be carried out by multiplying the best fit potential by a factor

$$f = 1 + \epsilon \delta_\sigma(\eta - \eta') \tag{35}$$

using a normalized Gaussian with a range parameter σ for the smeared δ-function,

$$\delta_\sigma(\eta - \eta') = \frac{1}{\sqrt{2\pi}\sigma} e^{-(\eta-\eta')^2/2\sigma^2} . \tag{36}$$

For finite values of ϵ and σ the FD can then be approximated by

$$\frac{\delta\chi^2[V(\eta)]}{\delta V(\eta')} \approx \frac{1}{V(\eta')} \frac{\chi^2[V(\eta)(1 + \epsilon\delta_\sigma(\eta - \eta'))] - \chi^2[V(\eta)]}{\epsilon} \; . \tag{37}$$

The parameter ϵ is used for a *fractional* change in the potential and the limit $\epsilon \to 0$ is obtained numerically for several values of σ and then extrapolated to $\sigma = 0$.

Figure 14 shows the FDs with respect to relative changes in the real part and with respect to relative changes in the full complex s-wave part of the best-fit pion-nucleus potential where the chiral $b_1(\rho)$ is assumed. Calculations of the FD with respect to the imaginary part of the potential show additivity of the FDs, hence the difference between the FD for

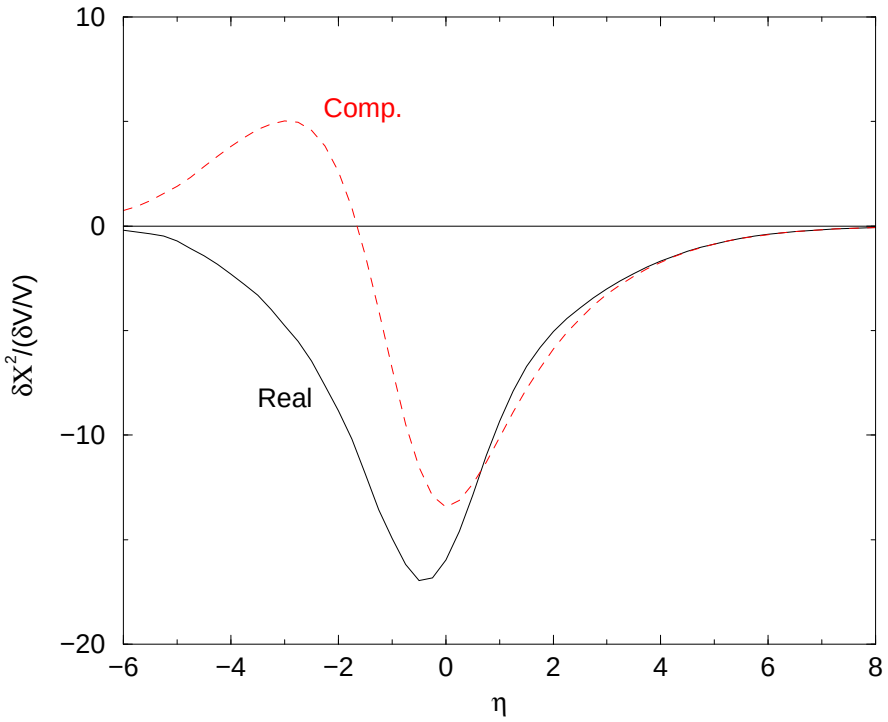

FIG. 14: Functional derivatives of the best fit χ^2 with respect to relative changes in the real part (solid curve) and with respect to relative changes in the full complex (dashed) s-wave pion nucleus potential Eq. (15), with $b_1(\rho)$ of Eq. (26)

the full complex potential and for the real part is the FD with respect to relative changes in the imaginary part of the s-wave part of the potential. It is immediately clear from the figure that both parts of the potential have quite similar importance in determining strong interaction effects in pionic atoms. Turning to radial sensitivity, recall that $\eta = -2.2$ corresponds to 90% of the central density of the nuclear charge and $\eta = 2.2$ corresponds to 10% of that density. It is therefore clear that pionic atom data are sensitive to the s-wave part of the potential over a region where the densities change between free space to the full central density. It is no wonder that using a fixed value for b_1 in fits to data led to 'abnormal' values for this parameter. With the success of the chiral $b_1(\rho)$ there is no reason for employing approximations such as linearization, by using an effective density.

E. Pion elastic scattering

The applicability of the Kisslinger potential [52] and its Ericson-Ericson extension [55] (Eqs. (15-22)) to elastic scattering of pions by nuclei had been demonstrated early in the days of the 'pion factories' [79, 103], mostly at energies higher than 40-50 MeV. Following the success with the 'chiral' density dependence of b_1 in the subthreshold regime of pionic atoms, it is interesting to study the behavior of the pion-nucleus potential across threshold into the scattering regime and to examine whether the pionic atom 'anomaly' is observed also above threshold when using a fixed value for the parameter b_1. Of particular interest is the question of whether the density dependence of the isovector amplitude as given by Eq. (26) is required by the scattering data. In the scattering scenario, unlike in the atomic case, one

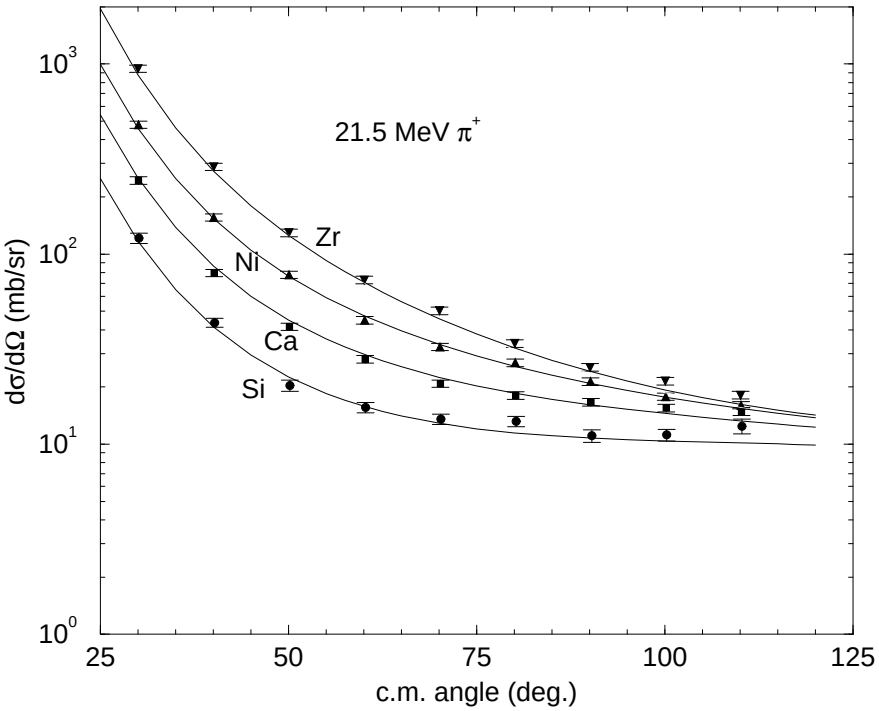

FIG. 15: Experimental results for elastic scattering of π^+ compared with calculations.

can study both charge states of the pion, thus increasing sensitivities to isovector effects and to the energy dependent effects due to the Coulomb interaction. Looking for earlier suitable data for elastic scattering, it was somewhat surprising to realize that at kinetic energies well below 50 MeV there seemed to be only one set of high quality data available for both charge states of the pion obtained in the same experiment, namely, the data of Wright et al. [104] for 19.5 MeV pions on calcium, with predominantly the $N = Z$ isotope ^{40}Ca. For that reason precision measurements of elastic scattering of 21.5 MeV π^+ and π^- by several nuclei were performed very recently at PSI [32, 33] with the aim of analyzing the results in terms of the same effects as found in pionic atoms. The experiment was dedicated to studying the elastic scattering of *both* pion charge states and special emphasis was placed on the absolute normalization of the cross sections, which was based on the parallel measurements of Coulomb scattering of muons.

Figures 15 and 16 show comparisons between experimental differential cross sections for the elastic scattering of 21.5 MeV π^+ and π^- by Si, Ca, Ni and Zr and calculations made with the best-fit EW potential, defined below. The fit to the data was made to all eight angular distributions put together, see Ref. [33] for details. Table V summarizes values of b_1 obtained for the various models, with C indicating a conventional (fixed b_1) potential, W indicating the use of the chiral-motivated $b_1(\rho)$ of Eq. (26) and EW stands for using $b_1(\rho)$ and including also the empirical energy dependence of b_0. It is evident that with the C potential using a fixed value for b_1 the fit to elastic scattering results yields too repulsive a value for b_1 in comparison with the corresponding value for the free πN interaction, much the same as is the case with pionic atoms. When the chiral motivated $b_1(\rho)$ of Eq. (26) is used χ^2 is reduced significantly and the resulting b_1 is essentially in agreement with the free value. Adding the empirical energy dependence of b_0 brings the two values into full agreement, much the same as is the case with pionic atoms. As with pionic atoms, the

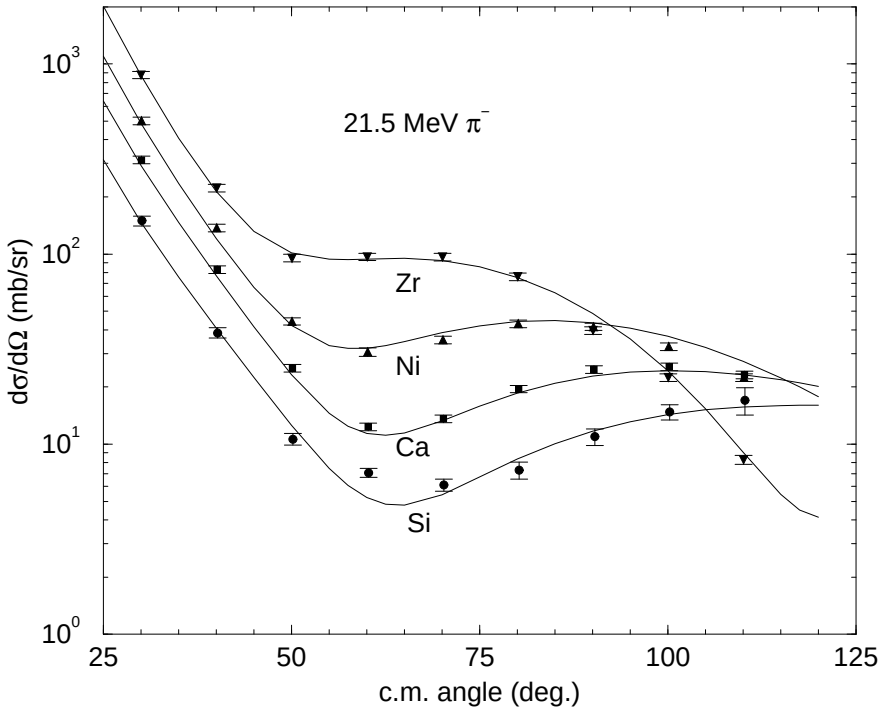

FIG. 16: Experimental results for elastic scattering of π^- compared with calculations.

TABLE V: Values of b_1 from fits to elastic scattering of 21.5 MeV $\pi^\pm$ by Si, Ca, Ni and Zr. The free πN value is $b_1^f = -0.0864 \pm 0.0010 m_\pi^{-1}$.

model	C	W	EW
$b_1(m_\pi^{-1})$	-0.114 ± 0.006	-0.081 ± 0.005	-0.083 ± 0.005
χ^2 for 72 points	134	88	88

chiral energy dependence in Eq. (27) caused large over-correction of the resulting b_1 which turns out to be significantly less repulsive than its free πN value.

It is therefore concluded that the extra-repulsion or s-wave anomaly is observed also in the scattering regime and that the medium-modification of the isovector term of the local part of the pion-nucleus potential is of the same nature both below and just above threshold.

F. Conclusions

Pionic atoms form the oldest type of exotic atom of a strongly-interacting particle and both experiment and theory had achieved maturity already in the 1990s, with the nagging problem of anomalously enhanced repulsion in the s-wave part of the potential essentially unresolved. The discrepancy between the in-medium b_1 and its free πN value became clearer with the ever improving accuracy of the experimental results on pionic hydrogen. In contrast, it seemed that experimental X-ray spectroscopy of medium-weight and heavy pionic atoms reached a dead end without new experiments in the last 20 years. The predicted existence of well-defined $1s$ and $2p$ states in heavy pionic atoms, due to saturation of widths caused by the s-wave repulsion, prompted the pioneering (d,^{3}He) experiments which supplied strong

interaction data unreached otherwise. Although the overall picture of pionic atom potentials has not changed due to these new data, they gave added impetus to the study of medium effects in the pion-nucleus interaction at threshold. The issue of the enhanced repulsion in the s-wave part of the potential appears to have been resolved with the chiral-motivated $b_1(\rho)$ of Eq. (26) which was shown to apply also at 21 MeV thanks to a recent dedicated experiment on elastic scattering of $\pi^{\pm}$ by nuclei. It may be concluded that the dominant effect of the nuclear environment on the real part of the pion-nucleus potentials close to threshold is given by Eq. (26). Note, however, that the absorption terms quadratic in density remain largely phenomenological.

IV. $\bar{K}$ NUCLEAR PHYSICS

A. Preview

The $\bar{K}$-nucleus interaction near threshold is strongly attractive and absorptive as suggested by fits to the strong-interaction shifts and widths of K^--atom levels [1]. Global fits yield 'deep' density dependent optical potentials with nuclear-matter depth $\mathrm{Re}V_{\bar{K}}(\rho_0) \sim -$(150-200) MeV [101, 105, 106, 107, 108], whereas in the other extreme case several studies that fit the low-energy K^-p reaction data, including the $I = 0$ quasibound state $\Lambda(1405)$ as input for constructing self consistently density dependent optical potentials, obtain relatively 'shallow' potentials with $\mathrm{Re}V_{\bar{K}}(\rho_0) \sim -$(40-60) MeV [24, 109, 110, 111]. For a recent update of these early calculations, see Ref. [112]. An example of a chirally motivated coupled-channel fit to the low-energy K^-p cross sections is shown in Fig. 17 from Ref. [24]. This calculation is based on the free-space chiral coupled-channel amplitudes used in the in-medium calculations of Waas et al. [26] following the earlier work of Kaiser et al. [113]. By imposing self consistency in its nuclear part (solid lines) the calculation [24] leads to a weakly density dependent shallow $\bar{K}$-nucleus potential in terms of the effective scattering length $a_{\rm eff}(\rho)$ of Fig. 3 in Sec. I. As is shown below, 'shallow' potentials are substantially inferior to 'deep' ones in comprehensive fits to K^--atom data. The issue of depth of $\mathrm{Re}V_{\bar{K}}$ is reviewed below and the implications of a 'deep' potential for the existence and properties of $\bar{K}$-nucleus quasibound states are discussed. Since the two-body $\bar{K}N$ interaction provides a starting point in many theoretical works for constructing the $\bar{K}$ nuclear optical potential $V_{\bar{K}}$, we start with a brief review of the $\bar{K}N$ data available near the K^-p threshold.

B. The K^-p interaction near threshold

The K^-p data at low energies provide a good experimental base upon which models for the strong interactions of the $\bar{K}N$ system have been developed. Near threshold the coupling to the open $\pi\Sigma$ and $\pi\Lambda$ channels is extremely important, as may be judged from the size of the K^-p reaction cross sections, particularly $K^-p \to \pi^+\Sigma^-$, with respect to the K^-p elastic cross sections shown in Fig. 17. Theoretical models often include also the closed $\eta\Lambda$, $\eta\Sigma$, $K\Xi$ channels [114]. Other threshold constraints are provided by the accurately determined threshold branching ratios [115, 116]

$$\gamma = \frac{\Gamma(K^-p \to \pi^+\Sigma^-)}{\Gamma(K^-p \to \pi^-\Sigma^+)} = 2.36 \pm 0.04\,, \tag{38}$$

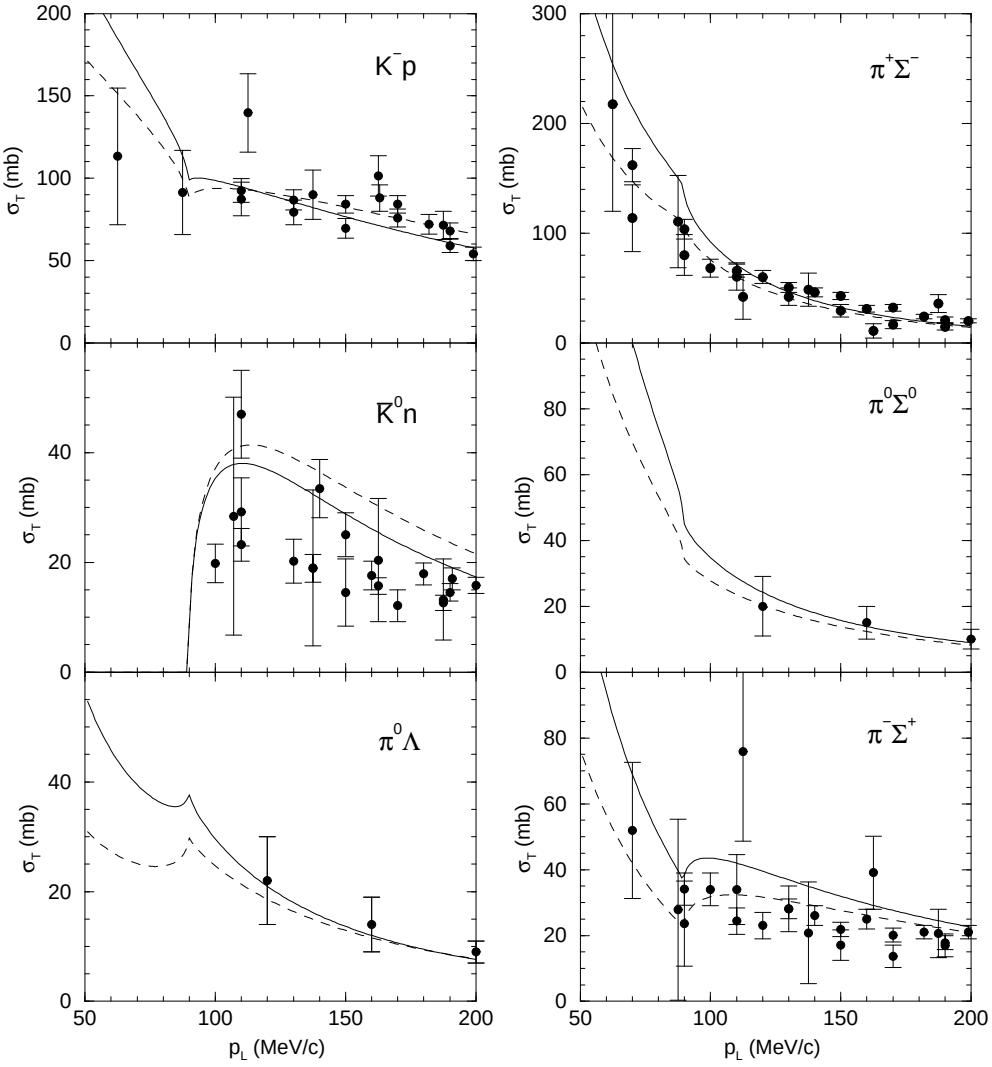

FIG. 17: Calculations from Ref. [24] of cross sections for K^-p scattering and reactions. The dashed lines show free-space chiral-model coupled-channel calculations using amplitudes from Ref. [26]. The solid lines show chiral-model coupled-channel calculations using slightly varied parameters in order to fit also the K^--atom data for a (shallow) optical potential calculated self consistently.

$$R_c = \frac{\Gamma(K^-p \to \pi^+\Sigma^-,\ \pi^-\Sigma^+)}{\Gamma(K^-p \to \text{all inelastic channels})} = 0.664 \pm 0.011\,, \tag{39}$$

$$R_n = \frac{\Gamma(K^-p \to \pi^0\Lambda)}{\Gamma(K^-p \to \pi^0\Lambda,\ \pi^0\Sigma^0)} = 0.189 \pm 0.015\,. \tag{40}$$

Additional sources of experimental information are the $\pi\Sigma$ invariant mass spectrum in the $I = 0$ channel from various reactions, and the K^-p scattering length deduced from the recent measurements at KEK [34] and at Frascati [35] (the DEAR collaboration) using a Deser-based formula [117]:

$$\epsilon_{1s} - \mathrm{i}\frac{\Gamma_{1s}}{2} \approx -2\alpha^3\mu^2_{K^-p}a_{K^-p}(1 - 2\alpha\mu_{K^-p}(\ln\,\alpha - 1)a_{K^-p})\,, \tag{41}$$

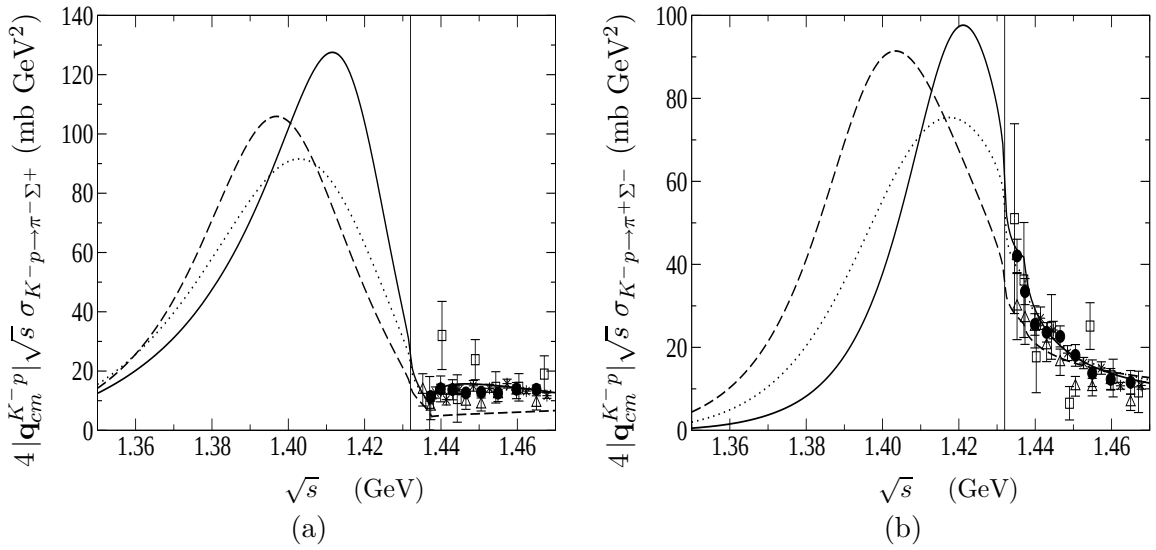

FIG. 18: Calculated cross sections for $K^-p \to \pi^\mp\Sigma^\pm$ multiplied by $4|\mathbf{q}_{cm}^{K^-p}|\sqrt{s}$ and continued below the K^-p threshold (vertical line), for three chiral coupled-channel fits to the K^-p low-energy data. The fit shown by the solid (dashed) lines excludes (includes) the DEAR value for a_{K^-p}. Figure taken from Ref. [119].

where α is the fine-structure constant. The value of a_{K^-p} derived from the DEAR measurement using this expression, $a_{K^-p} = (-0.45 \pm 0.09) + \mathrm{i}(0.27 \pm 0.12)$ fm, appears inconsistent with most comprehensive fits to the low-energy K^-p scattering and reaction data, as discussed by Borasoy et al. [118, 119, 120, 121]. A dissenting view, however, is reviewed recently by Oller et al. [122].

The K^-p elastic, charge-exchange and reaction cross sections shown in Fig. 17 refer to energies above the K^-p threshold at $\sqrt{s} = 1432$ MeV. However, by developing potential models, or limiting the discussion to phenomenological K-matrix analyses, $\bar{K}N$ amplitudes are obtained that allow for analytic continuation into the nonphysical region below threshold. Using a K-matrix analysis, this was the way Dalitz and Tuan predicted the existence of the $\Lambda(1405)$ $\pi\Sigma$, $I = 0$ resonance in 1959 [123]. Recent examples from a coupled-channel potential model calculation [119] based on low-energy chiral expansion are shown in the next three figures. Figure 18 depicts the quantity $4|\mathbf{q}_{cm}^{K^-p}|\sqrt{s}\sigma_{K^-p\to\pi^\mp\Sigma^\pm}(s)$ obtained by continuing the $K^-p \to \pi\Sigma$ amplitudes below the K^-p threshold. One sees clearly the resonant behavior of the extrapolated cross sections due to the $\Lambda(1405)$. This resonance is also seen in Fig. 19 where the real and imaginary parts of the K^-p elastic scattering amplitude, continued analytically below the K^-p threshold, are plotted. The discrepancy with $\mathrm{Im}a_{K^-p}$ deduced from the DEAR measurement [35], as given above, is clearly seen. In contrast to amplitudes which allow for the $I = 0$ $\bar{K}N$ channel and thus exhibit a resonance effect due to the $\Lambda(1405)$, the purely $I = 1$ K^-n amplitude does not show such effects below threshold, as seen in Fig. 20 where the real and imaginary parts of the K^-n elastic scattering amplitude, within the same coupled-channel model, are shown. The model dependence of the K^-n elastic scattering amplitude, as given by the three different curves, is considerably weaker than the model dependence of amplitudes in which the $\Lambda(1405)$ resonance enters, e.g. the $K^-p \to \pi^\mp\Sigma^\pm$ amplitudes related to the cross sections shown in Fig. 18.

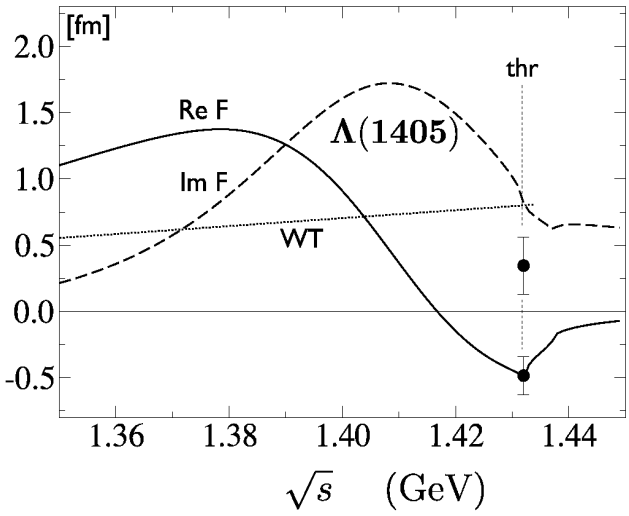

FIG. 19: Real and imaginary parts of the K^-p forward elastic scattering amplitude, fitted within a NLO chiral SU(3) coupled-channel approach to K^-p scattering and reaction data. The line denoted WT is the (real) LO Tomozawa-Weinberg K^-p driving-term amplitude. The DEAR measurement [35] value for a_{K^-p} is shown with error bars. Figure taken from Ref. [124], based on the work of Ref. [119].

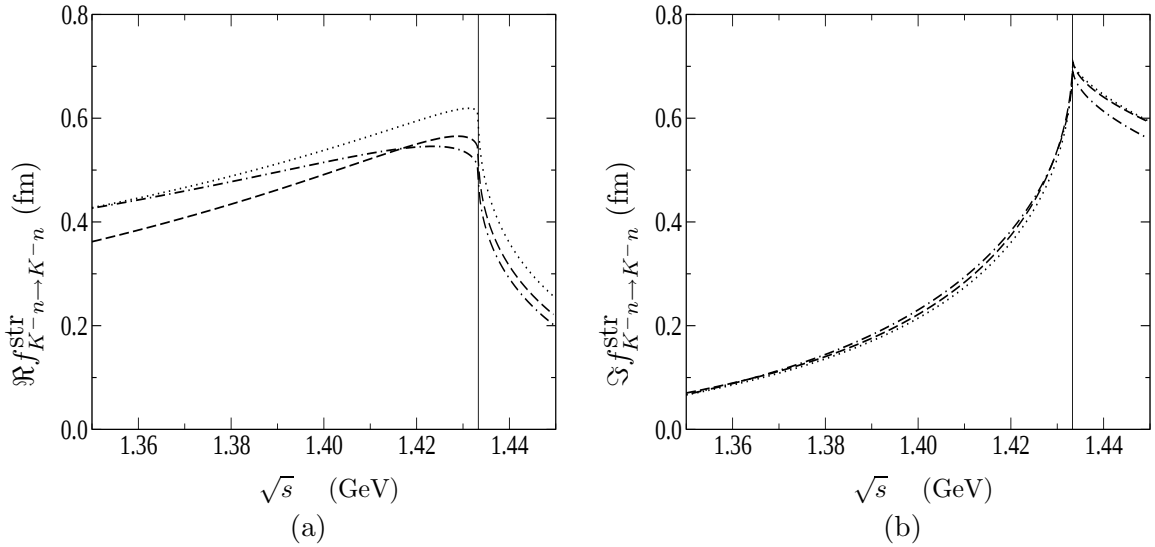

FIG. 20: Real (left) and imaginary part (right) of the K^-n forward elastic scattering amplitude, continued below the K^-n threshold (vertical line). The various lines correspond to different interaction models, the dashed line standing for the Tomozawa-Weinberg interaction. Figure taken from Ref. [119].

C. $\bar{K}$-nucleus potentials

The gross features of low-energy $\bar{K}N$ physics, as demonstrated in the previous section by chiral coupled-channel fits to the low-energy K^-p scattering and reaction data, are encapsulated in the leading-order Tomozawa-Weinberg (TW) vector term of the chiral effective

Lagrangian [125]. The Born approximation for the $\bar{K}$-*nuclear* optical potential $V_{\bar{K}}$ due to the TW interaction term yields then a sizable attraction:

$$V_{\bar{K}} = -\frac{3}{8f_\pi^2}\,\rho \sim -55\,\frac{\rho}{\rho_0}\ \ \mathrm{MeV} \tag{42}$$

for $\rho_0 = 0.16$ fm^{-3}, where $f_\pi \sim 93$ MeV is the pseudoscalar meson decay constant. Iterating the TW term plus next-to-leading-order terms, within an *in-medium* coupled-channel approach constrained by the $\bar{K}N - \pi\Sigma - \pi\Lambda$ data near the $\bar{K}N$ threshold, roughly doubles this $\bar{K}$-nucleus attraction. It is found (e.g. Ref. [26]) that the $\Lambda(1405)$ quickly dissolves in the nuclear medium at low density, so that the repulsive free-space scattering length a_{K^-p}, as function of ρ, becomes *attractive* well below ρ_0. Since the purely $I = 1$ attractive scattering length a_{K^-n} is only weakly density dependent, the resulting in-medium $\bar{K}N$ isoscalar scattering length $b_0(\rho) = \frac{1}{2}(a_{K^-p}(\rho) + a_{K^-n}(\rho))$ translates into a strongly attractive $V_{\bar{K}}$:

$$V_{\bar{K}}(r) = -\frac{2\pi}{\mu_{KN}}\,b_0(\rho)\,\rho(r)\ , \qquad \mathrm{Re}V_{\bar{K}}(\rho_0) \sim -110\ \mathrm{MeV}\,. \tag{43}$$

This in-medium $\bar{K}N$ isoscalar scattering length $b_0(\rho)$ is the same one as the effective scattering length $a_{\rm eff}$ plotted as function of the density ρ in Fig. 3 in Sec. I D. It is useful to record that $b_0(\rho_0) \approx 1$ fm corresponds to $V_{\bar{K}}(\rho_0) \approx -100$ MeV. However, when $V_{\bar{K}}$ is calculated *self consistently*, namely by including $V_{\bar{K}}$ in the propagator G_0 used in the Lippmann-Schwinger equation determining $b_0(\rho)$, as demonstrated by Eq. (13) in Sec. I D, one obtains $\mathrm{Re}V_{\bar{K}}(\rho_0) \sim -(40\text{-}60)$ MeV [24, 109, 110, 111]. The main reason for this weakening of $V_{\bar{K}}$, approximately going back to that calculated using Eq. (42), is the strong absorptive effect which $V_{\bar{K}}$ exerts within G_0 to suppress the higher Born terms of the $\bar{K}N$ TW potential.

Additional considerations for estimating $V_{\bar{K}}$ are listed below.

- QCD sum-rule estimates [126] for vector (v) and scalar (s) self-energies:

$$\Sigma_v(\bar{K})\ \sim\ -\frac{1}{2}\,\Sigma_v(N)\ \sim\ -\frac{1}{2}\,(200)\ \mathrm{MeV}\ =\ -100\ \mathrm{MeV}\,, \tag{44}$$

$$\Sigma_s(\bar{K})\ \sim\ \frac{m_s}{M_N}\,\Sigma_s(N)\ \sim\ \frac{1}{10}\,(-300)\ \mathrm{MeV}\ =\ -30\ \mathrm{MeV}\,, \tag{45}$$

  where m_s is the strange-quark (current) mass. The factor 1/2 in Eq. (44) is due to the one nonstrange antiquark $\bar{q}$ in the $\bar{K}$ meson out of two possible, and the minus sign is due to G-parity going from q to $\bar{q}$. This rough estimate gives then $V_{\bar{K}}(\rho_0) \sim -130$ MeV.

- The QCD sum-rule approach essentially refines the mean-field argument [127, 128]

$$V_{\bar{K}}(\rho_0)\ \sim\ \frac{1}{3}\,(\Sigma_s(N) - \Sigma_v(N))\ \sim\ -170\ \mathrm{MeV}\,, \tag{46}$$

  where the factor 1/3 is again due to the one nonstrange antiquark in the $\bar{K}$ meson, but here with respect to the three nonstrange quarks of the nucleon.

- The ratio of K^-/K^+ production cross sections in nucleus-nucleus and proton-nucleus collisions near threshold, measured by the Kaon Spectrometer (KaoS) collaboration [129] at SIS, GSI, yields an estimate $V_{\bar{K}}(\rho_0) \sim -80$ MeV by relying on

TABLE VI: Calculated $(K^-_{\rm stop},\pi)$ rates on ^{12}C per stopped K^- (in units of 10^{-3}) for $1p_N \to 1s_\Lambda$ capture into the 1^- ground-state configurations in $^{12}_{\Lambda}$C and $^{12}_{\Lambda}$B, for various fitted optical potentials ordered according to their depth. Table taken from Ref. [24].

final $^{A}_{\Lambda}$Z	chiral	effective	fixed	DD	$R_{\rm exp}\times 10^3$
$^{12}_{\Lambda}$C	0.231	0.169	0.089	0.063	0.98 ± 0.12 [130]
$^{12}_{\Lambda}$B	0.119	0.087	0.046	0.032	0.28 ± 0.08 [131]

Boltzmann-Uehling-Uhlenbeck (BUU) transport calculations normalized to the value $V_K(\rho_0)\sim +25$ MeV. Since $\bar{K}NN\to YN$ absorption processes apparently were disregarded in these calculations, a deeper $V_{\bar{K}}$ may follow once nonmesonic absorption processes are included.

- Capture rates of $(K^-_{\rm stop},\pi)$ reactions to specific Λ hypernuclear states provide a sensitive measure for the strength of the K^- optical potential at threshold. A very strong potential, as discussed in Sec. IV E, generates $\bar{K}$-*nuclear* quasibound states which due to orthogonality with the K^- atomic states force the wavefunctions of the latter to oscillate and become suppressed within the nuclear volume, and thus to reduce their effectiveness in the calculation of the $(K^-_{\rm stop},\pi)$ transition matrix element. The results of DWIA calculations [24] for capture on ^{12}C into the 1^- ground state configurations of $^{12}_{\Lambda}$C and $^{12}_{\Lambda}$B are shown in Table VI, using several fitted K^- optical potentials which are ordered according to their depth. It is clearly seen that the deeper the K^- optical potential is, the lower the calculated rate becomes. Unfortunately, all the calculated rates shown in Table VI are much lower than the measured values $R_{\rm exp}$ [130, 131], making it difficult to draw definitive conclusions. Furthermore, the experimental capture rates depart strongly from the ratio 2 : 1 expected from charge independence for the ratio $R(^{12}_{\Lambda}{\rm C})/R(^{12}_{\Lambda}{\rm B})$ for the rates $R_{\rm exp}$.

D. Fits to K^- -atom data

The K^--atom data used in global fits [1] span a range of nuclei from ^{7}Li to ^{238}U, with 65 level-shifts, widths and transition yields data points. It was shown already in the mid 1990s [1] that although a reasonably good fit to the data is obtained with the generic $t\rho$ potential of Eq. (3) with an effective complex parameter b_0 corresponding to attraction, greatly improved fits are obtained with a density-dependent potential, where the fixed b_0 is replaced by $b_0 + B_0[\rho(r)/\rho_0]^\alpha$, with b_0, B_0 and $\alpha \geq 0$ determined by fits to the data. Fitted potentials of this kind are marked DD. This parameterization offers the advantage of fixing b_0 at its (repulsive) free-space value in order to respect the low-density limit, while relegating the expected in-medium attraction to the B_0 term which goes with a higher power of the density. As mentioned in Sec. IV A, the $t\rho$ best-fit potentials have real parts which are less than 100 MeV deep for medium-weight and heavy nuclei. The corresponding density-dependent potentials are more attractive, 150-200 MeV deep, hence the 'shallow' *vs* 'deep' terminology. Chirally inspired approaches that fit the low-energy K^-p reaction data predict attractive potentials of depths ∼(110-120) MeV [26] and, additionally, by requiring self consistency in the construction of the optical potential, lead to yet shallower potentials with ${\rm Re}V_{\bar{K}}(\rho_0)\sim -$(40-60) MeV [24, 110]. Recent experimental reports on candidates for

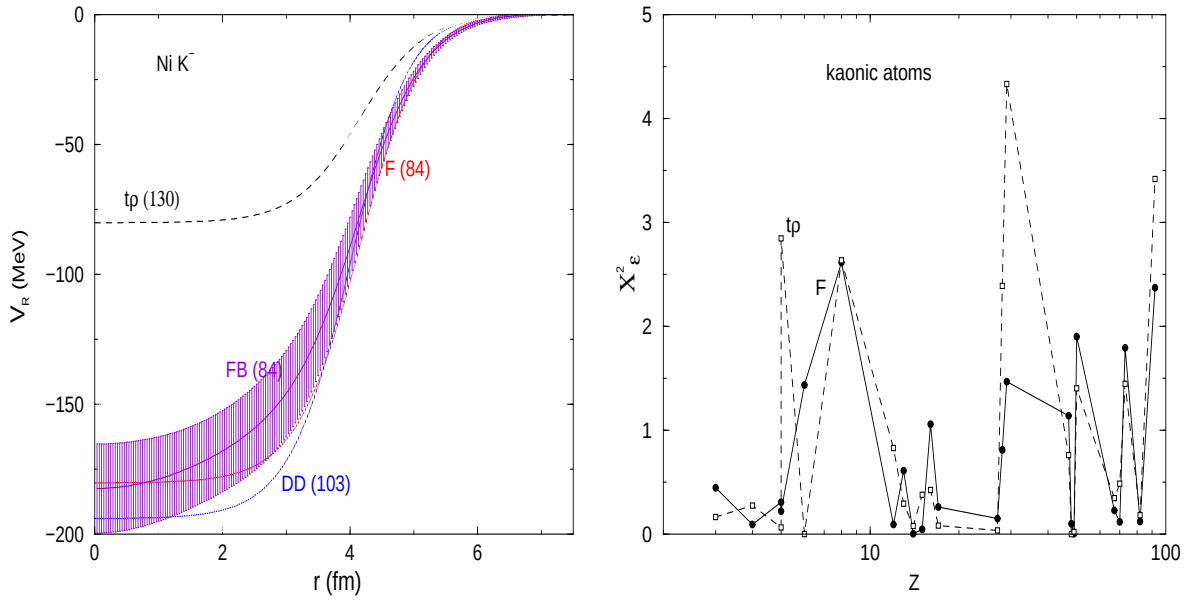

FIG. 21: Left: real part of the $\bar{K}$-^{58}Ni potential obtained in a global fit to K^--atom data using the model-independent FB technique [101], in comparison with other best-fit potentials and χ^2 values in parentheses. Right: contributions to the χ^2 of K^- atomic shifts for the *deep* density-dependent potential F from Ref. [108] and for the *shallow* $t\rho$ potential.

$\bar{K}$-nuclear deeply bound states in the range of binding $B_{\bar{K}} \sim$ 100-200 MeV [37, 38, 39, 40] again highlighted the question of how much attractive the $\bar{K}$-nucleus interaction is below the $\bar{K}N$ threshold. Therefore the motivation for re-analysis of a comprehensive set of kaonic atom data is two fold. First is the question of 'deep' *vs.* 'shallow' real $\bar{K}$-nucleus potential, in light of recent possible experimental evidence for the existence of deeply bound kaonic states whose binding energies exceed the depth of the shallow type of potential obtained from fits to kaonic atom data. However, if the deep variety of potential is confirmed, then the dependence of the $\bar{K}N$ interaction on the nuclear density becomes of prime concern. This density dependence is the second point which motivated the re-analysis of kaonic atoms data [108] although there have not been any new experimental results on strong interaction effects in kaonic atoms since the early 1990s.

The departure of the optical potential from the fixed-t $t\rho$ approach was introduced [108] with the help of a geometrical model, where one *loosely* defines in coordinate space an 'internal' region and an 'external' region by using the multiplicative functions $F(r)$ in the former and $[1 - F(r)]$ in the latter, where $F(r)$ is defined as

$$F(r) \;=\; \frac{1}{e^x + 1} \tag{47}$$

with $x \;=\; (r - R_x)/a_x$. Then clearly $F(r) \;\rightarrow\; 1$ for $(R_x - r) >> a_x$, which defines the internal region. Likewise $[1 \;-\; F(r)] \;\rightarrow\; 1$ for $(r - R_x) >> a_x$, which defines the external region. Thus R_x forms an approximate border between the internal and the external regions, and *if* R_x is close to the nuclear surface then the two regions will correspond to the high density and low density regions of nuclear matter, respectively. The fixed b_0 in the $t\rho$ potential was replaced by

$$b_0 \;\rightarrow\; B_0\; F(r) \;+\; b_0\; [1 \;-\; F(r)] \tag{48}$$

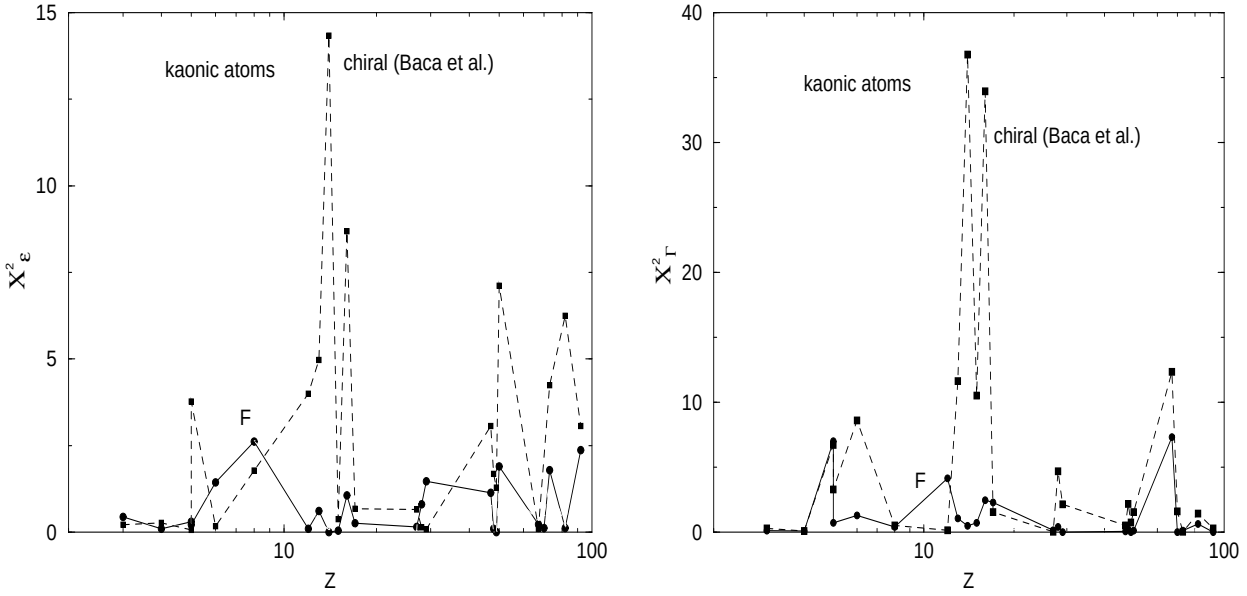

FIG. 22: Contributions to the χ^2 of K^- atomic shifts (left) and widths (right) for the *deep* density-dependent potential F from Ref. [108] and for the *shallow* chirally-based potential from Ref. [132].

where the parameter b_0 represents the low-density interaction and the parameter B_0 represents the interaction inside the nucleus. This division into regions of high and low densities is meaningful *provided* R_x is close to the radius of the nucleus and a_x is of the order of 0.5 fm. This is indeed the case, as found in global fits to kaonic atom data [108]. We note that unlike with pionic and antiprotonic atoms, the dependence of kaonic atom fits on the rms radius of the neutron distribution is marginal.

Figure 21 (left) shows, as an example, the real part of the best-fit potential for ^{58}Ni obtained with the various models discussed above, i.e. the simple $t\rho$ model and its DD extension, and the geometrical model F, with the corresponding values of χ^2 for 65 data points in parentheses. Also shown, with an error band, is a Fourier-Bessel (FB) fit [101] that is discussed below. We note that, although the two density-dependent potentials marked DD and F have very different parameterizations, the resulting potentials are quite similar. In particular, the shape of potential F departs appreciably from $\rho(r)$ for $\rho(r)/\rho_0 \leq 0.2$, where the physics of the $\Lambda(1405)$ is expected to play a role. The density dependence of the potential F provides by far the best fit ever reported for any global K^--atom data fit, and the lowest χ^2 value as reached by the model-independent FB method. On the right-hand side of the figure are shown the individual contributions to χ^2 of the shifts for the deep F potential and the shallow $t\rho$ potential. Figure 22 shows comparisons between χ^2 values of the shifts and of the widths for the F potential and the yet shallower chirally-based potential of Baca et al. [132]. It is self evident that the agreement between calculation and experiment is substantially better for the deep F potential than for the shallow chiral potentials.

The question of how well the real part of the K^--nucleus potential is determined was discussed in Ref. [101]. Estimating the uncertainties of hadron-nucleus potentials as function of position is not a simple task. For example, in the '$t\rho$' approach the shape of the potential is determined by the nuclear density distribution and the uncertainty in the strength parameter, as obtained from χ^2 fits to the data, implies a fixed *relative* uncertainty at all radii, which is, of course, unfounded. Details vary when more elaborate forms such as 'DD' or 'F' are

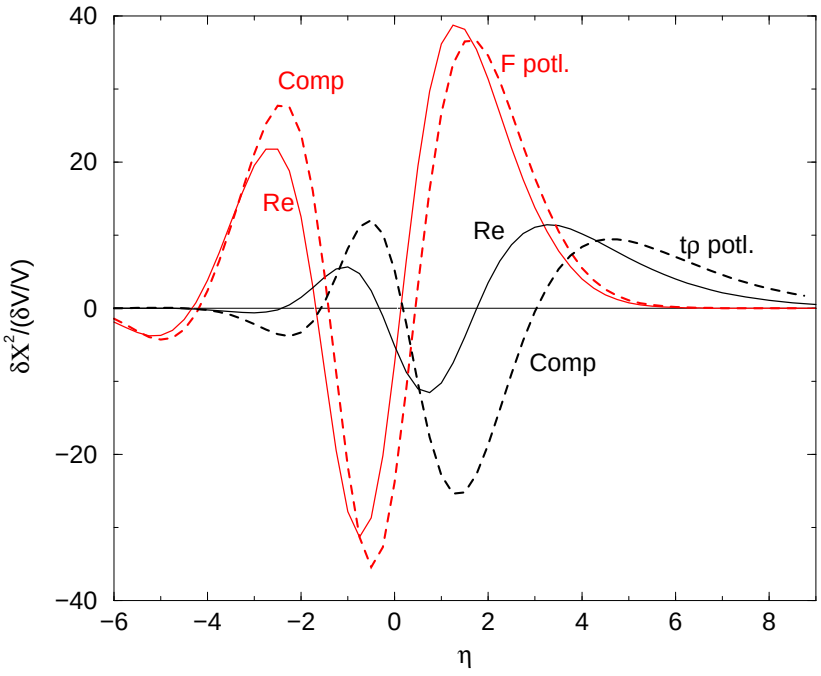

FIG. 23: Functional derivatives of kaonic atoms χ^2 with respect to the fully complex (Comp, dashed lines) and real (Re, solid lines) potential as function of η, where $r = R_c + \eta a_c$, with R_c and a_c the radius and diffuseness parameters, respectively, of the charge distribution. Results are shown for the $t\rho$ potential and for the $t(\rho)$ 'F' potential of Ref. [108] obtained from global fits to kaonic atom data.

used, but one is left essentially with *analytical continuation* into the nuclear interior of potentials that might be well-determined only close to the nuclear surface. 'Model-independent' methods have been used in analyses of elastic scattering data for various projectiles [11] to alleviate this problem. However, applying e.g. the Fourier-Bessel (FB) method in global analyses of kaonic atom data, one ends up with too few terms in the series, thus making the uncertainties unrealistic in their dependence on position. This is illustrated in Fig. 21 by the 'FB' curve, obtained by adding a Fourier-Bessel series to a '$t\rho$' potential. Only three terms in the series are needed to achieve a χ^2 of 84 and the potential becomes deep, in agreement with the other two 'deep' solutions. The error band obtained from the FB method [11] is, nevertheless, unrealistic because only three FB terms are used. However, an increase in the number of terms is found to be unjustified numerically.

The functional derivative (FD) method for identifying the radial regions to which exotic atom data are sensitive is described in detail in Sec. III D 4. This method was applied in Ref. [101] to the F and $t\rho$ kaonic atom potentials and results are shown in Fig. 23 where η is a global parameter defined by $r = R_c + \eta a_c$, with R_c and a_c the radius and diffuseness parameters, respectively, of the charge distribution. From the figure it can be inferred that the sensitive region for the real $t\rho$ potential is between $\eta = -1.5$ and $\eta = 6$ whereas for the F potential it is between $\eta = -3.5$ and $\eta = 4$. Recall that $\eta = -2.2$ corresponds to 90% of the central charge density and $\eta = 2.2$ corresponds to 10% of that density. It therefore becomes clear that within the $t\rho$ potential there is no sensitivity to the interior of the nucleus whereas with the $t(\rho)$ 'F' potential, which yields greatly improved fit to the data, there is sensitivity to regions within the full nuclear density. The different sensitivities result

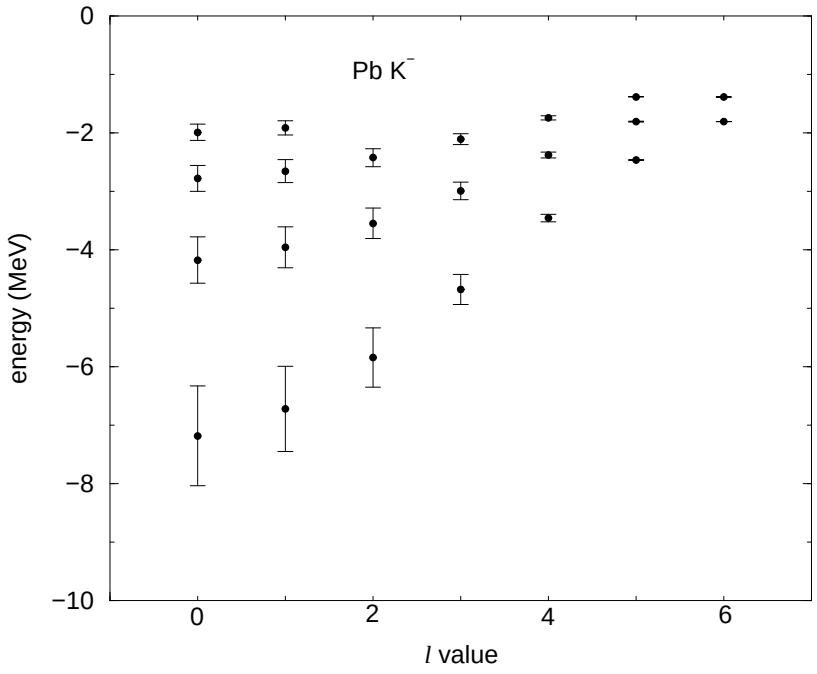

FIG. 24: Calculated energies of K^- atomic states in ^{208}Pb. The lowest energy for each l value corresponds to $n = l + 1$. The bars represent the widths of the states.

from the potentials themselves: for the $t\rho$ potential the interior of the nucleus is masked essentially by the strength of the imaginary potential. In contrast, for the F potential not only is its imaginary part significantly smaller than the imaginary part of the $t\rho$ potential [108] but also the additional attraction provided by the deeper potential enhances the *atomic* wavefunctions within the nucleus [1] thus creating the sensitivity at smaller radii. As seen in the figure, the functional derivative for the complex F potential is well approximated by that for its real part.

It is concluded that optical potentials derived from the observed strong-interaction effects in kaonic atoms are sufficiently deep to support strongly-bound antikaon states, but it does not necessarily imply that such states are sufficiently narrow to be resolved unambiguously from experimental spectra. Moreover, the discrepancy between the very shallow chirally motivated potentials [24, 110], the intermediate potentials of depth around 100 MeV [26] and the deep phenomenological potentials of type 'F' remains an open problem. It should also be kept in mind that these depths relate to $\bar{K}$ potentials at *threshold*, whereas the information required for $\bar{K}$-nuclear quasibound states is at energies of order 100 MeV below threshold.

E. Deeply bound K^- atomic states

Somewhat paradoxically, due to the strong absorptive imaginary part of the K^--nucleus potential, relatively narrow deeply-bound atomic states are expected to exist which are quite independent of the real potential. Such states are indeed found in numerical calculations as can be seen in Fig. 24 where calculated binding energies and widths of atomic states of K^- in ^{208}Pb are shown for several l-values, down to states which are inaccessible via the X-ray

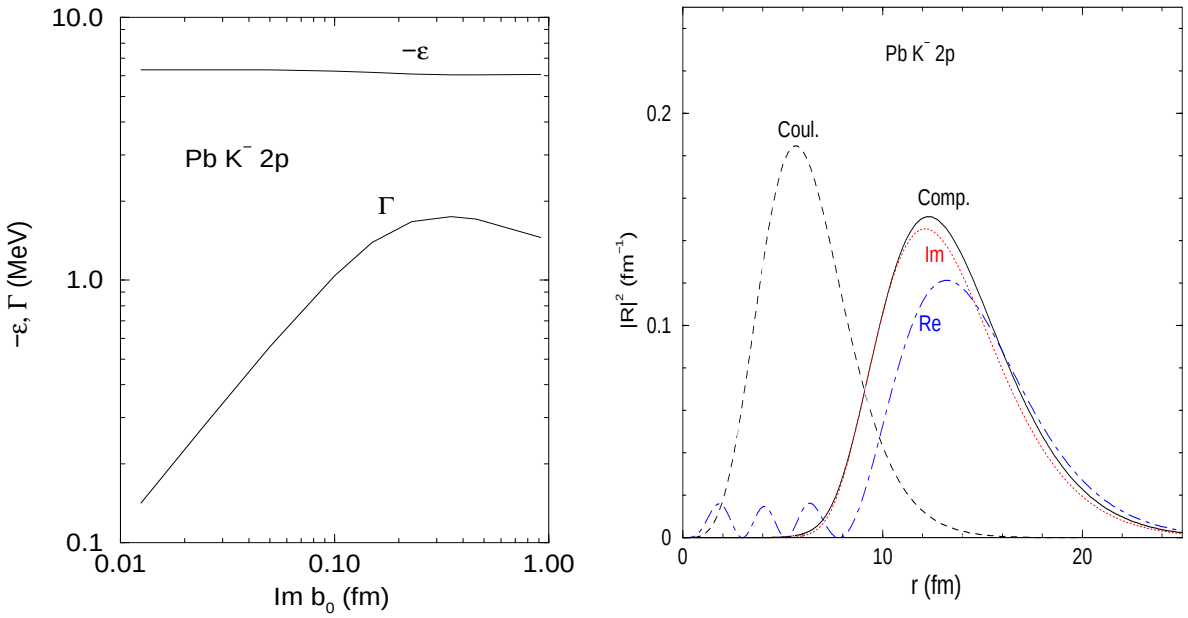

FIG. 25: Saturation of width Γ for the $2p$ 'deeply bound' K^- atomic state in ^{208}Pb as function of absorptivity, Imb_0, for Re$b_0 = 0.62$ fm (left) and wavefunctions for this state (right).

cascade. For ^{208}Pb, the last observed K^- atomic circular state is the $7i$, corresponding to $l = 6$. The general physics behind this phenomenon is similar to that responsible for the deeply-bound pionic atom states, although there are differences in the mechanism. For a Schrödinger equation the width of a state is given *exactly* by Eq. (23) and if a normalized atomic wavefunction is expelled from the nucleus, then small widths are expected due to the reduced overlap between the atomic wavefunction and the imaginary potential. (For the KG equation there are small changes in the expression Eq. (23), see Refs. [133, 134].) The mechanism behind the pionic atom deeply bound states is simply the repulsive real part of the s-wave potential. In contrast, phenomenological kaonic atom potentials are attractive, but the strengths of the imaginary part of the potential are such that the decay of the wavefunction as it enters the nucleus is equivalent to repulsion, resulting in narrow atomic states due to the reduced overlap as discussed above. It is seen from Fig. 24 that there is a saturation phenomenon where widths hardly increase for $l \leq 2$, contrary to intuitive expectation. The repulsive effect of sufficiently strong absorption is responsible for the general property of saturation of widths of atomic states and saturation of reaction cross sections above threshold, observed experimentally for antiprotons (see Sec. VI F.)

The left-hand side of Fig. 25 shows the saturation of widths as function of Imb_0 for the $2p$ state of kaonic atoms of ^{208}Pb. For small values of Imb_0 the calculated width increases linearly but already at 20% of the best-fit value of 0.9 fm saturation sets in and eventually the width goes down with further increase of the absorption. Note that the real part of the binding energy, represented here by the strong interaction level shift ϵ, is hardly changing with Imb_0. The right-hand side of Fig. 25 shows radial wavefunctions for the $2p$ atomic K^- state in ^{208}Pb for several combinations of potentials. The dashed curve marked 'Coul' is for the Coulomb potential only, and with a half-density radius for ^{208}Pb of 6.7 fm it clearly overlaps strongly with the nucleus. Adding the full complex optical potential the solid curve marked 'Comp' shows that the wavefunction is expelled from the nucleus, and the dotted curve marked 'Im' shows that this repulsion is effected by the imaginary part

of the potential. Clearly the overlap of the wavefunction with the nucleus is dramatically reduced compared to the Coulomb-only situation. An interesting phenomenon is displayed by the dot-dashed curve marked 'Re'. It shows the wavefunction when the real potential is added to the Coulomb potential, demonstrating significant *repulsion* of the wavefunction by the added *attractive* potential. The explanation for this bizarre result is provided by the three small peaks inside the nucleus which are due to the orthogonality of the *atomic* wavefunction and strongly-bound K^- *nuclear* wavefunctions having the same l-values. This extra structure of the wavefunction in the interior effectively disappears when the imaginary potential is included.

F. Deeply bound K^- nuclear states in light nuclei

No saturation mechanism holds for the width of $\bar{K}$-nuclear states which retain very good overlap with the potential. Hence, the questions to ask are (i) whether it is possible at all to bind *strongly* $\bar{K}$ mesons in nuclei, and (ii) are such quasibound states sufficiently narrow to allow observation and identification? The first question was answered affirmatively by Nogami [135] as early as 1963 arguing that the K^-pp system could acquire about 10 MeV binding in its $I = 1/2,\ L = S = 0$ state. Yamazaki and Akaishi, using a complex energy-independent $\bar{K}N$ potential within a single-channel K^-pp calculation [136], reported a binding energy $B \sim 50$ MeV and width $\Gamma \sim 60$ MeV. Preliminary results of revised Antisymmetrized Molecular Dynamics (AMD) calculations by Doté and Weise [124, 137] which implicitly account for $\bar{K}N - \pi\Sigma$ coupling agree on B but estimate $\Gamma \sim 100$ MeV. Coupled-channel $\bar{K}NN - \pi\Sigma N$ Faddeev calculations [138, 139, 140, 141] of K^-pp have confirmed this order of magnitude of binding, $B\ \sim$ 55-75 MeV, differing on the width; the calculations by Shevchenko et al. [138, 139] give large values, $\Gamma \sim 100$ MeV, for the mesonic width. These Faddeev calculations overlook the $\bar{K}NN \to YN$ coupling to nonmesonic channels which are estimated to add, conservatively, 20 MeV to the overall width. Altogether, the widths calculated for the K^-pp quasibound state are likely to be so large as to make it difficult to identify it experimentally [142].

The current experimental and theoretical interest in $\bar{K}$-nuclear bound states was triggered back in 1999 by the suggestion of Kishimoto [143] to look for such states in the nuclear reaction (K^-, p) in flight, and by Akaishi and Yamazaki [144, 145] who suggested to look for a $\bar{K}NNN$ $I = 0$ state bound by over 100 MeV for which the main $\bar{K}N \to \pi\Sigma$ decay channel would be kinematically closed. In fact, Wycech had conjectured that the width of such states could be as small as 20 MeV [146]. Some controversial evidence for relatively narrow states was presented initially in $(K^-_{\rm stop}, p)$ and $(K^-_{\rm stop}, n)$ reactions on ^{4}He (KEK-PS E471) [37, 38] but has recently been withdrawn (KEK-PS E549/570) [147]. $\bar{K}$-nuclear states were also invoked to explain few statistically-weak irregularities in the neutron spectrum of the (K^-, n) in-flight reaction on ^{16}O (BNL-AGS, parasite E930) [39], but subsequent (K^-, n) and (K^-, p) reactions on ^{12}C at $p_{\rm lab} = 1$ GeV/c (KEK-PS E548) [148] have not disclosed any peaks beyond the appreciable strength observed below the $\bar{K}$-nucleus threshold. Ongoing experiments by the FINUDA spectrometer collaboration at DAΦNE, Frascati, already claimed evidence for a relatively broad K^-pp deeply bound state ($B \sim 115$ MeV) in $K^-_{\rm stop}$ reactions on Li and ^{12}C, by observing back-to-back Λp pairs from the decay $K^-pp \to \Lambda p$ [40], but these pairs could naturally arise from conventional absorption processes at rest when final-state interaction is taken into account [149]. Indeed, the $K^-_{\rm stop}pn \to \Sigma^- p$ reaction on ^{6}Li has also been recently observed [150]. Another recent claim of a very narrow and deep

K^-pp state ($B \sim 160$ MeV, $\Gamma \sim 30$ MeV) is also based on observing decay Λp pairs, using $\bar{p}$ annihilation data on ^{4}He from the OBELIX spectrometer at LEAR, CERN [151]. The large value of B_{K^-pp} over 100 MeV conjectured by these experiments is at odds with *all* the few-body calculations of the K^-pp system listed above. One cannot rule out that the Λp pairs assigned in the above analyses to K^-pp decay in fact result from nonmesonic decays of different clusters, say the $\bar{K}NNN$ $I = 0$ quasibound state. A definitive study of the K^-pp quasibound state (or more generally $\{\bar{K}[NN]_{I=1}\}_{I=1/2}$) could be reached through fully exclusive formation reactions, such as:

$$K^- + {}^3\mathrm{He} \;\rightarrow\; n + \{\bar{K}[NN]_{I=1}\}_{I=1/2,I_z=+1/2}, \quad p + \{\bar{K}[NN]_{I=1}\}_{I=1/2,I_z=-1/2}\,, \tag{49}$$

the first of which is scheduled for day-one experiment in J-PARC [152]. Finally, preliminary evidence for a $\bar{K}NNN$ $I = 0$ state with $B = 58\pm6$ MeV, $\Gamma = 37\pm14$ MeV has been recently presented by the FINUDA collaboration on ^{6}Li by observing back-to-back Λd pairs [153]. It is clear that the issue of $\bar{K}$ nuclear states is far yet from being experimentally resolved and more dedicated, systematic searches are necessary.

G. RMF dynamical calculations of $\bar{K}$ quasibound nuclear states

In this model, spelled out in Refs. [108, 154, 155], the (anti)kaon interaction with the nuclear medium is incorporated by adding to $\mathcal{L}_N$ the Lagrangian density $\mathcal{L}_K$:

$$\mathcal{L}_K = \mathcal{D}^*_\mu \bar{K} \mathcal{D}^\mu K - m_K^2 \bar{K} K - g_{\sigma K} m_K \sigma \bar{K} K\,. \tag{50}$$

The covariant derivative $\mathcal{D}_\mu = \partial_\mu + i g_{\omega K} \omega_\mu$ describes the coupling of the (anti)kaon to the vector meson ω. The(anti)kaon coupling to the isovector ρ meson was found to have negligible effects. The $\bar{K}$ meson induces additional source terms in the equations of motion for the meson fields σ and ω_0. It thus affects the scalar $S = g_{\sigma N}\sigma$ and the vector $V = g_{\omega N}\omega_0$ potentials which enter the Dirac equation for nucleons, and this leads to rearrangement or polarization of the nuclear core, as shown on the left-hand side of Fig. 26 for the calculated average nuclear density $\bar{\rho} = \frac{1}{A}\int \rho^2 d\mathbf{r}$ as a function of B_{K^-} for K^- nuclear $1s$ states across the periodic table. It is seen that in the light K^- nuclei, $\bar{\rho}$ increases substantially with B_{K^-} to values about 50% higher than without the $\bar{K}$. The increase of the central nuclear densities is bigger, up to 100%, and is nonnegligible even in the heavier K^- nuclei where it is confined to a small region of order 1 fm. Furthermore, in the Klein-Gordon equation satisfied by the $\bar{K}$, the scalar $S = g_{\sigma K}\sigma$ and the vector $V = -g_{\omega K}\omega_0$ potentials become *state dependent* through the *dynamical* density dependence of the mean-field potentials S and V, as expected in a RMF calculation. An imaginary $\mathrm{Im}V_{\bar{K}} \sim t\rho$ was added, fitted to the K^- atomic data [107]. It was then suppressed by an energy-dependent factor $f(B_{\bar{K}})$, considering the reduced phase-space for the initial decaying state and assuming two-body final-state kinematics for the decay products in the $\bar{K}N \rightarrow \pi Y$ mesonic modes (80%) and in the $\bar{K}NN \rightarrow YN$ nonmesonic modes (20%).

The RMF coupled equations were solved self-consistently. For a rough idea, whereas the static calculation gave $B^{1s}_{K^-} = 132$ MeV for the K^- $1s$ state in ^{12}C, using the values $g^{\rm atom}_{\omega K}$, $g^{\rm atom}_{\sigma K}$ corresponding to the K^--atom fit, the dynamical calculation gave $B^{1s}_{K^-} = 172$ MeV. In order to scan a range of values for $B^{1s}_{K^-}$, the coupling constants $g_{\sigma K}$ and $g_{\omega K}$ were varied in given intervals of physical interest.

Beginning approximately with ^{12}C, the following conclusions may be drawn:

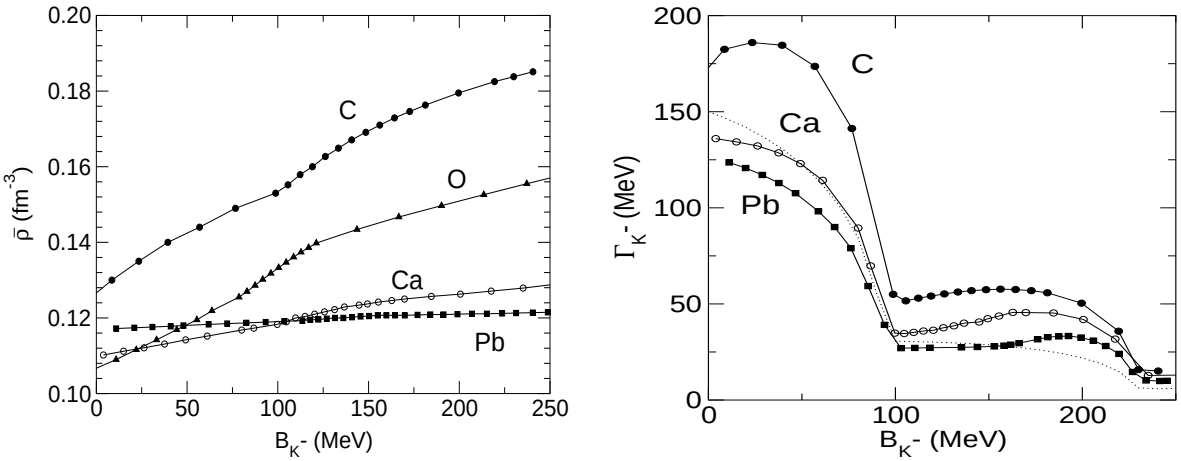

FIG. 26: Dynamically calculated average nuclear density $\bar{\rho}$ (left) and widths Γ_{K^-} (right) of $1s$ K^--nuclear states in the nuclei denoted, as function of the $1s$ K^- binding energy [108].

- For given values of $g_{\sigma K}, g_{\omega K}$, the $\bar{K}$ binding energy $B_{\bar{K}}$ saturates as function of A, except for a small increase due to the Coulomb energy (for K^-).

- The difference between the binding energies calculated dynamically and statically, $B_{\bar{K}}^{\rm dyn} - B_{\bar{K}}^{\rm stat}$, is substantial in light nuclei, increasing with $B_{\bar{K}}$ for a given value of A, and decreasing monotonically with A for a given value of $B_{\bar{K}}$. It may be neglected only for very heavy nuclei. The same holds for the nuclear rearrangement energy $B_{\bar{K}}^{\rm s.p.} - B_{\bar{K}}$ which is a fraction of $B_{\bar{K}}^{\rm dyn} - B_{\bar{K}}^{\rm stat}$.

- The width $\Gamma_{\bar{K}}(B_{\bar{K}})$ decreases monotonically with A, according to the right-hand side of Fig. 26 which shows calculated widths Γ_{K^-} as function of the binding energy B_{K^-} for $1s$ states in ${}_{K^-}{}^{12}$C, ${}_{K^-}{}^{40}$Ca and ${}_{K^-}{}^{208}$Pb. The dotted line shows the static 'nuclear-matter' limit corresponding to the K^--atom fitted value ${\rm Im}b_0 = 0.62$ fm and for $\rho(r) = \rho_0 = 0.16$ fm^{-3}, using the same phase-space suppression factor as in the 'dynamical' calculations. It is clearly seen that the functional dependence $\Gamma_{K^-}(B_{K^-})$ follows the shape of the dotted line. This dependence is due primarily to the binding-energy dependence of the suppression factor $f(B_{K^-})$ which falls off rapidly until $B_{K^-} \sim$ 100 MeV, where the dominant $\bar{K}N \to \pi\Sigma$ gets switched off, and then stays rather flat in the range $B_{K^-} \sim$ 100-200 MeV where the width is dominated by the $\bar{K}NN \to YN$ absorption modes. The widths calculated in this range are considerably larger than given by the dotted line (except for Pb in the range $B_{K^-} \sim$ 100-150 MeV) due to the dynamical nature of the RMF calculation, whereby the nuclear density is increased by the polarization effect of the K^-. Adding perturbatively the residual width neglected in this calculation, partly due to the $\bar{K}N \to \pi\Lambda$ secondary mesonic decay channel, a representative value for a lower limit $\Gamma_{\bar{K}} \geq 50 \pm 10$ MeV holds in the binding energy range $B_{K^-} \sim$ 100-200 MeV. Fig. 27 shows the effect of splitting the 80% mesonic decay width, previously assigned all to $\pi\Sigma$ absorption channels, between $\pi\Sigma$ (70%) and $\pi\Lambda$ (10%), and also of simulating the 20% nonmesonic absorption channels by a ρ^2 dependence compared to ${\rm Im}V_{\bar{K}} \sim t\rho$ used by Mareš et al. [108]. These added contributions [155] make the lower limit $\Gamma_{\bar{K}} \geq 50 \pm 10$ MeV a rather conservative one.

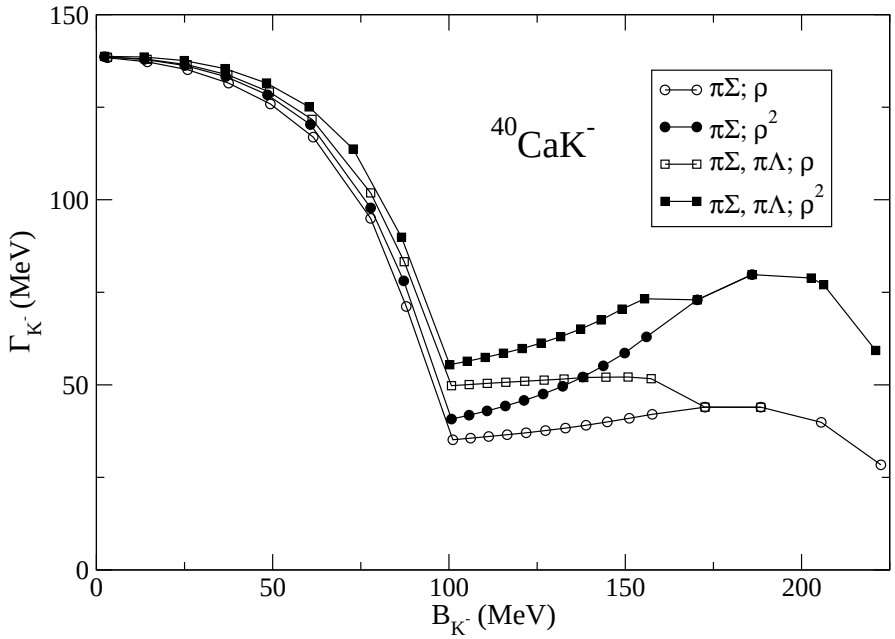

FIG. 27: Dynamically calculated widths of the $1s$ K^--nuclear state in ${}^{40}_{K^-}$Ca for $\pi\Sigma + \pi\Lambda$ compared to $\pi\Sigma$ final mesonic absorption channels, and for ρ^2 compared to ρ dependence of the final nonmesonic absorption channels, as function of the K^- binding energy, from Gazda et al. [155].

V. K^+ MESONS

A. Overview of the K^+-nucleus interaction

There are obviously no K^+ exotic atoms to provide information on the K^+-nucleus interaction below threshold. Nevertheless, it has been found that for pions and antiprotons the optical potentials cross smoothly from the atomic into the scattering regime, and therefore studies of the K^+-nucleus interaction at low energies above threshold are relevant to the general topic of medium modifications of the interaction. In fact, K^+ mesons provide a clear example of such modifications.

The K^+N interaction below the pion-production threshold is fairly weak and featureless and this merit has motivated past suggestions to probe nuclear in-medium effects by studying scattering and reaction processes with K^+ beams below 800 MeV/c; see Ref. [156] for an early review. The insufficiency of the impulse-approximation $t_{\rm free}\rho$ form of the K^+ - nucleus optical potential, where $t_{\rm free}$ is the free-space K^+N t matrix, was somewhat of a surprise already in the 1980s. Limited total cross-section data [157] on carbon, and elastic and inelastic differential cross section data [158] on carbon and calcium showed problems with the $t\rho$ potential, particularly with respect to its reaction content ('reactivity' below). In order to account for the increased reactivity in K^+ - nucleus interactions, Siegel et al. [159] and later Peterson [160] suggested that nucleons 'swell' in the nuclear medium, primarily by increasing the dominant hard-core S_{11} phase shift. Brown et al. [161] suggested that the extra reactivity was due to the reduced in-medium masses of exchanged vector mesons, and this was subsequently worked out in detail in Ref. [162]. Another source for increased reactivity in K^+ - nucleus interactions was discussed in the 1990s and is due to meson exchange-current effects [163, 164].

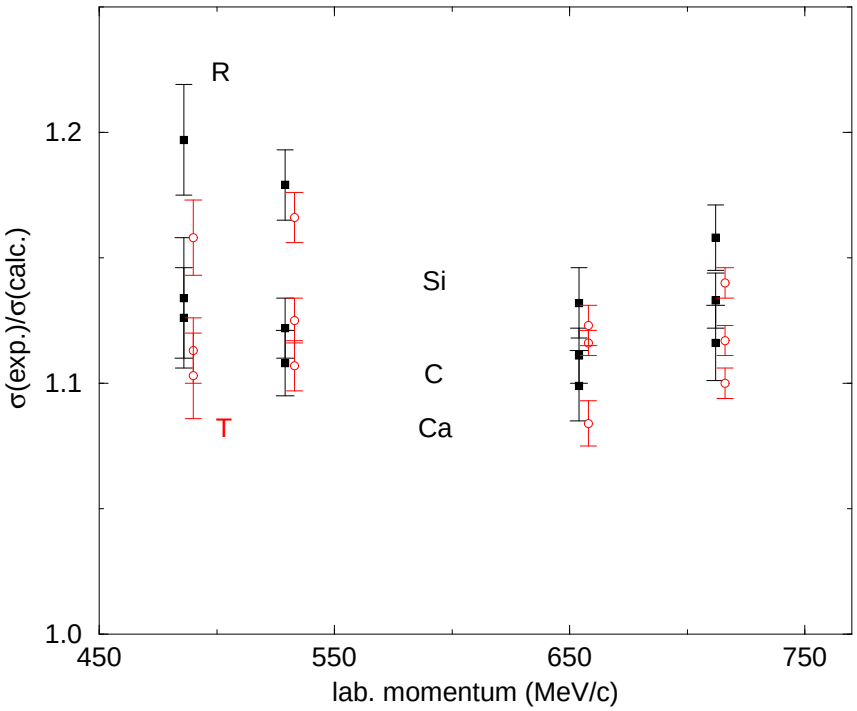

FIG. 28: Ratios between experimental and calculated cross sections for calculations based on $V_{\rm opt}^{(K^+)} = t\rho$ fits to ^{6}Li. Solid squares represent σ_R, circles represent σ_T.

Some further experimental progress was made during the early 1990s, consisting mostly of measuring attenuation cross sections in K^+ transmission experiments at the BNL-AGS on deuterium and several other nuclear targets in the momentum range $p_{\rm lab}$ = 450-740 MeV/c [165, 166, 167] and extracting K^+-nucleus total cross sections. The same transmission data were then reanalyzed to extract in addition total reaction cross sections [41], which are less dependent on the potential used in converting measured attenuation into cross sections and eventually self-consistent final values of K^+ integral cross sections (reaction and total) on ^{6}Li, ^{12}C, ^{28}Si and ^{40}Ca were published in Refs. [42, 43]. These integral cross-section data gave clear evidence for the density dependence of the increased reactivity suggested by the earlier data, as demonstrated in Fig. 28 from Ref. [42]. Plotted in the figure are ratios of experimental to calculated integral cross sections for ^{12}C, ^{28}Si and ^{40}Ca, where the calculated cross sections use a $t\rho$ potential fitted to the ^{6}Li data. These ratios, for the denser nuclei, deviate considerably from the value of one in a way which is largely independent of the beam momentum.

Other measurements during the 1990s include K^+ quasielastic scattering on several targets at 705 MeV/c [168] and new measurements of K^+ elastic and inelastic differential cross sections on ^{6}Li and ^{12}C at 715 MeV/c [169], further analyzed in Ref. [170]. These data and analyses lent support to the substantial medium modifications demonstrated above on the basis of studying integral cross sections. By the late 1990s, experimentation in K^+ - nuclear physics had subsided, and with it died out also theoretical interest although the problems with medium modifications of the interaction remained, as is shown below. Theoretical interest in K^+ - nuclear physics to some extent has been revived recently [171, 172, 173, 174], particularly in connection with possible contributions due to Θ^+ pentaquark degrees of free-

dom, as is also discussed below.

B. Kaon-nucleus optical potential

The starting form adopted for the kaon-nucleus optical potential $V_{\rm opt}$, following Eq. (4) of Sec. I B, is the simplest possible $t\rho$ form:

$$2\varepsilon_{\rm red}^{(A)} V_{\rm opt}(r) = -4\pi F_A b_0 \rho(r) \quad , \tag{51}$$

where $\varepsilon_{\rm red}^{(A)}$ is the center-of-mass (c.m.) reduced energy,

$$(\varepsilon_{\rm red}^{(A)})^{-1} = E_p^{-1} + E_A^{-1} \tag{52}$$

in terms of the c.m. total energies for the projectile and target respectively, and

$$F_A = \frac{M_A\sqrt{s}}{M(E_A + E_p)} \tag{53}$$

is a kinematical factor resulting from the transformation of amplitudes between the KN and the K^+ - nucleus c.m. systems, with M the free nucleon mass, M_A the mass of the target nucleus and $\sqrt{s}$ the total projectile-nucleon energy in their c.m. system. The parameter b_0 in Eq. (51) reduces in the impulse approximation to the (complex) isospin-averaged KN scattering amplitude in the forward direction. For ^{6}Li and for ^{12}C the modified harmonic oscillator (MHO) form was used for the nuclear densities whereas for ^{28}Si and for ^{40}Ca the two-parameter Fermi (2pF) form was used and minor changes were made to parameters of the neutron density to check sensitivities to ρ_n. The data base for the analysis were the 32 integral cross sections for K^+ on ^{6}Li, ^{12}C, ^{28}Si and ^{40}Ca from Ref. [43].

Fits to the integral cross sections were made [171, 172] separately at each of the four momenta, varying the complex parameter b_0, and the results are summarized in Table VII, marked as $t\rho$ for each momentum. From the values of χ^2 per point it is seen that the fits are unacceptably poor and the resulting Reb_0 and Imb_0 disagree with the corresponding free K^+N values (marked as $t_{\rm free}\rho$ and derived from the KN phase shifts as given by SAID [175]). The discrepancies are particularly noticeable for Imb_0, which are determined to good accuracy. Evidently the experimental results indicate significant increase in reactivity, as mentioned in Sec. V A.

The obvious next step is to effectively make b_0 density dependent by introducing higher powers of the density, such as

$$b_0\ \rho(r) \rightarrow b_0\ \rho(r)\ +\ B\ \rho^2(r)\ , \tag{54}$$

where both parameters b_0 and B are to be determined from fits to the data. The results [171, 172] are also shown in Table VII, marked as Eq. (54), where Reb_0 was kept fixed at its respective free KN value. The improvement in the fits to the data is evident from the reduction of the values of χ^2, but except for the lowest incoming momentum the quality of the fits suggests that something is still missing. Guided by earlier analyses [42, 43] that achieved much improved fits by introducing the *average* nuclear density $\bar{\rho}$ for each target nuclide,

$$\bar{\rho} = \frac{1}{A}\int \rho^2 d\mathbf{r}\,, \tag{55}$$

TABLE VII: Fits to the eight K^+ - nuclear integral cross sections [43] at each of the four laboratory momenta $p_{\rm lab}$ (in MeV/c), using different potentials.

$p_{\rm lab}$	$V_{\rm opt}$	Reb_0(fm)	Imb_0(fm)	ReB(fm^4)	ImB(fm^4)	χ^2/N
488	$t\rho$	$-0.203(26)$	0.172(7)			16.3
	$t_{\rm free}\rho$	-0.178	0.153			
	Eq.(54)	-0.178	0.122(5)	0.52(20)	0.88(8)	1.18
	Eq.(56)	-0.178	0.129(4)	0.17(11)	0.62(6)	0.27
531	$t\rho$	$-0.196(39)$	0.202(9)			56.3
	$t_{\rm free}\rho$	-0.172	0.170			
	Eq.(54)	-0.172	0.155(14)	1.79(46)	0.72(27)	7.01
	Eq.(56)	-0.172	0.146(5)	0.46(21)	0.78(7)	3.94
656	$t\rho$	$-0.220(50)$	0.262(12)			54.9
	$t_{\rm free}\rho$	-0.165	0.213			
	Eq.(54)	-0.165	0.203(18)	1.66(80)	0.89(36)	7.24
	Eq.(56)	-0.165	0.204(5)	2.07(19)	0.77(7)	0.32
714	$t\rho$	$-0.242(53)$	0.285(15)			67.7
	$t_{\rm free}\rho$	-0.161	0.228			
	Eq.(54)	-0.161	0.218(24)	1.40(95)	1.10(48)	9.3
	Eq.(56)	-0.161	0.218(6)	1.51(43)	0.97(9)	1.24

Eq. (54) was replaced by the following ansatz [171, 172]:

$$b_0\ \rho(r) \rightarrow b_0\ \rho(r)\ +\ B\ \bar{\rho}\ \rho(r)\ . \tag{56}$$

The results of this prescription are also shown in Table VII, marked as Eq. (56) and it is clear that the fits to the data are very good. This use of the average nuclear density singles out the ^{6}Li target from the other three targets, due to its average density $\bar{\rho}$ being close to 50% of the corresponding values for the other targets. This is a purely phenomenological observation without (as yet) any theory behind it.

In order to further test the picture that emerges from the analysis of the integral cross sections for the K^+ - nucleus interaction, the analysis was repeated [172] including also differential cross sections for the elastic scattering of K^+ by some of the target nuclei. Fits were made to the combined integral and differential cross sections at 714 MeV/c consisting of the eight integral cross sections and the 17 differential cross sections from Ref. [170], using the potentials of either Eq. (54) or Eq. (56). Figure 29 shows that again the $\bar{\rho}\rho$ version of the potential Eq. (56) is preferred and the fits to the differential cross sections are good. The potential parameters obtained from the fits to the combined integral and differential cross sections agree, within uncertainties, with the corresponding values in Table VII.

Prior to discussing in the next section the reactive content of the above forms of density-dependent K^+ - nucleus optical potentials, it is worth noting that the splitting of Im$V_{\rm opt}$ in Table VII into its two reactive components Imb_0 and ImB appears well determined by the data at all energies, and perhaps is even model independent, particularly for the $\bar{\rho}\rho$ version Eq. (56) of the optical potential for which very accurate values of Imb_0 are derived. These values of Imb_0 are close to, but somewhat below the corresponding free-space values,

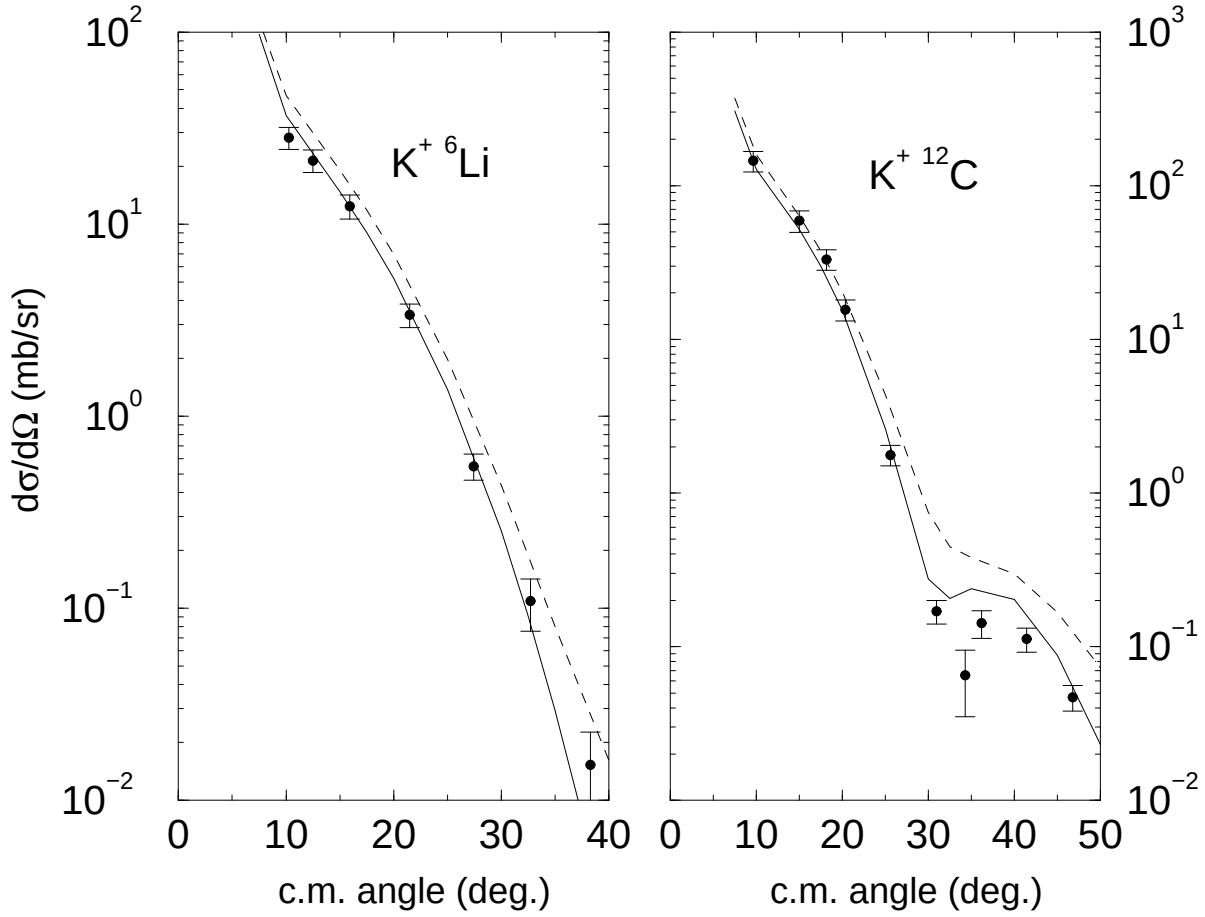

FIG. 29: Comparison between measured differential cross sections for K^+ elastic scattering at $p_{\rm lab} = 715$ MeV/c on ^{6}Li and ^{12}C [170] and best-fit calculations using Eq. (54) (dashed lines) and Eq. (56) (solid lines).

a feature which is observed in calculations which replace the $t\rho$ form by $g\rho$ where nuclear phase space effects are considered explicitly [173]. The values derived for ImB are roughly independent of the form of the piece added to $t\rho$, $\Delta V_{\rm opt}$, whether Eq. (54) or Eq. (56) are used to derive these values from the data. In contrast, the two components of Re$V_{\rm opt}$ are correlated strongly when Reb_0 is also varied, largely cancelling each other into a resulting poorly determined Re$V_{\rm opt}$. For this reason, it will appear difficult to offer any conclusive model for the physics underlying the real part of $\Delta V_{\rm opt}$.

C. K^+ absorption cross sections

The effect of $\Delta V_{\rm opt}$, within the improved fits to the K^+-nuclear integral cross sections, is demonstrated in the upper part of Fig. 30 for the reaction cross sections per nucleon σ_R/A at 488 MeV/c, where the calculated cross sections using a best-fit $t\rho$ optical potential (dashed line) are compared with the experimental values listed in Ref. [43]. The $t\rho$ fit fails to reconcile the ^{6}Li data with the data on the other, denser nuclei. If ^{6}Li is removed from the data base, then it becomes possible to fit reasonably well the data for the rest of the

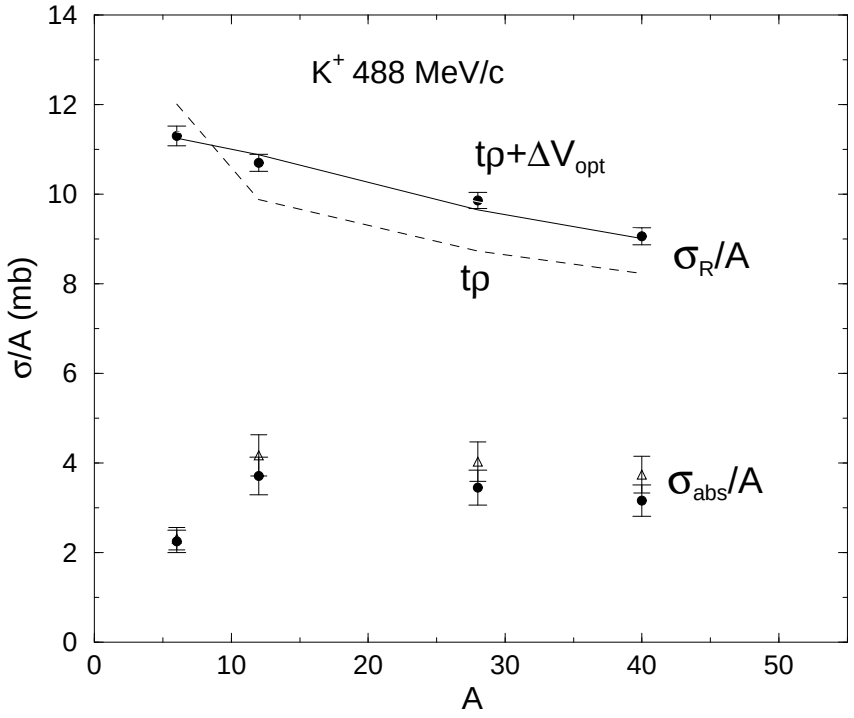

FIG. 30: Data and calculations [171] for K^+ reaction cross sections per nucleon (σ_R/A) at $p_{\rm lab}$ = 488 MeV/c are shown in the upper part. Calculated K^+ absorption cross sections per nucleon ($\sigma_{\rm abs}/A$) are shown in the lower part, see text.

nuclei, but the rise in Imb_0 with respect to its free-space value is then substantially higher than that for the $t\rho$ potential when ^{6}Li is included. At the higher energies, $t\rho$ fits which exclude ^{6}Li are less successful than at 488 MeV/c, while also requiring a substantial rise in Imb_0, which means increased values of the in-medium KN total cross sections with respect to the corresponding free-space values. This has been observed also in a K^+ - nucleus quasifree-scattering analysis [176], for K^+ mesons incident on C, Ca, Pb at $p_{\rm lab}$ = 705 MeV/c [168]. Also shown in the upper part of Fig. 30, by the solid line marked $t\rho + \Delta V_{\rm opt}$, are calculated reaction cross sections at 488 MeV/c using Eq. (56). This is a very good fit. Recently, Tolos et al. [173] have demonstrated that a similarly substantial improvement in the reproduction of reaction cross sections could be achieved microscopically by coupling in pentaquark degrees of freedom. It is tempting to assume that the effects of absorbing K^+ mesons into a pentaquark configuration are given by the difference between the solid curve and the dashed curve in Fig. 30 for nuclear targets heavier than ^{6}Li. However, for a quantitative estimate of the K^+ *absorption* cross sections one needs to do a more explicit calculation.

In close analogy to analyses of pionic atoms and of low-energy pion-nuclear scattering reactions in which the parameter B_0 (cf. Eq. (15)) is related to π^- nuclear absorption processes on two and on more nucleons, the additional piece $\Delta V_{\rm opt}$ due to the nonzero value of the parameter B in Eqs. (54,56) represents K^+ nuclear absorption into Θ^+ - nuclear final states. Here Θ^+, with mass $M_{\Theta^+} \approx 1540$ MeV, is an hypothetical $S = +1$ 'exotic' pentaquark baryon, searches for which have not provided conclusive evidence (for a recent review see Ref. [177]). The abnormally small upper limit $\Gamma_{\Theta^+} < 1$ MeV for the width of the

Θ^+ pentaquark deduced from some of these searches implies a negligible $\Theta^+ \to KN$ coupling, but this does not limit the coupling $\Theta^+ N \to KNN$ which is related to virtual decays such as $\Theta^+ \to \pi KN$ [178]. Gal and Friedman [171, 172] estimated the nuclear absorption cross sections of K^+ mesons by using two slightly different versions of the distorted-wave Born approximation:

$$\sigma_{\rm abs}^{(K^+)} \sim -\frac{2}{\hbar v}\int {\rm Im}(\Delta V_{\rm opt}(r))\ |\Psi^{(+)}_{(\Delta V_{\rm opt}=0)}(\mathbf{r})|^2\ d\mathbf{r}\quad , \tag{57}$$

and

$$\sigma_{\rm abs}^{(K^+)} \sim -\frac{2}{\hbar v}\int {\rm Im}(\Delta V_{\rm opt}(r))\ |\Psi^{(+)}(\mathbf{r})|^2\ d\mathbf{r}\quad , \tag{58}$$

where the distorted waves $\Psi^{(+)}_{(\Delta V_{\rm opt}=0)}$ are calculated discarding $\Delta V_{\rm opt}$.

Calculated absorption cross sections *per target nucleon* at $p_{\rm lab} = 488$ MeV/c are shown in the lower part of Fig. 30 for the fit using Eq. (56) for $V_{\rm opt}$ in Table VII. The triangles are for expression (57) and the solid circles are for expression (58). The error bars plotted are due to the uncertainty in the parameter ImB. It is seen that these calculated absorption cross sections, for the relatively dense targets of ^{12}C, ^{28}Si and ^{40}Ca, are proportional to the mass number A, and the cross section per target nucleon due to Im$B \neq 0$ is estimated as close to 3.5 mb. Although the less successful Eq. (54) gives cross sections larger by 40% at this particular incident momentum, this value should be regarded an upper limit, since the best-fit density-dependent potentials of Refs. [42, 43] yield values smaller than 3.5 mb by a similar amount. The experience gained from studying π-nuclear absorption [179] leads to the conclusion that $\sigma_{\rm abs}(K^+NN)$ is smaller than the extrapolation of $\sigma_{\rm abs}^{(K^+)}/A$ in Fig. 30 to $A = 1$, and since the KN interaction is weaker than the πN interaction one expects a reduction of roughly 50%, so that $\sigma_{\rm abs}(K^+NN)\ \sim$ 1-2 mb.

In Fig. 30, the considerably smaller absorption cross section per nucleon calculated for the relatively low-density ^{6}Li nucleus suggests a cross section of order fraction of millibarn, in a possible missing-mass search based on observing the final proton in the two-body reaction $K^+d \to \Theta^+p$. This cross section is not expected to exhibit marked resonance behavior near $p_{\rm lab} \sim 440$ MeV/c, which corresponds to the $\Theta^+(1540)$ resonance assumed rest mass, even if Θ^+ is very narrow. For the heavier nuclear targets too, the assignment of the excess reactivity observed in K^+-nuclear cross sections as due to $S = +1$ pentaquark degrees of freedom does not require the existence of a *narrow* KN resonance. It only assumes that pentaquark degrees of freedom are spread over this energy range with sufficient spectral strength. For nuclear targets other than deuterium, given the magnitude of the K^+ nuclear absorption cross sections as reviewed here, (K^+, p) experiments could prove useful. This reaction which has a 'magic momentum' about $p_{\rm lab} \sim 600$ MeV/c, where the $\Theta^+(1540)$ is produced at rest, is particularly suited to study bound or continuum states in *hyponuclei* ($S = +1$ nuclei according to the terminology suggested by Alfred Goldhaber [180]).

In conclusion, the available K^+ nuclear cross section data at $p_{\rm lab} \sim$ 450-800 MeV/c reveal substantial reactivity beyond that produced by the impulse approximation, or for that purpose by any effective $t\rho$ form of the K^+ optical potential. It was shown that this extra reactivity may be explained by adding a two-nucleon absorption channel $K^+nN \to \Theta^+N$, where the Θ^+ degrees of freedom need not materialize within a narrow energy bin. This provides a density-dependent mechanism that couples in $S = +1$ pentaquark degrees of freedom in a way which is insensitive to the width of their spectral distribution [171]. While there is no firm support at present for this conjecture from other phenomenological sources, a robust experimental program of measuring low-energy K^+d and K^+ - nuclear scattering

and reaction cross sections in the range $p_{\rm lab} \sim$ 300-800 MeV/c, and particularly about 400 Mev/c, would be extremely useful to decide whether or not $S = +1$ pentaquark degrees of freedom are involved in K^+ - nuclear dynamics.

VI. ANTIPROTONS

A. Overview of the $\bar{p}$-nucleus potential

In line with the other types of exotic atoms, the interaction of antiprotons with nuclei at threshold is described in terms of an optical potential, which in the simplest $t\rho$ form is given by

$$2\mu V_{\rm opt}(r) = -4\pi(1 + \frac{\mu}{M}\frac{A-1}{A})[b_0(\rho_n + \rho_p) + b_1(\rho_n - \rho_p)] \quad , \tag{59}$$

where μ is the reduced mass of the $\bar{p}$, ρ_n and ρ_p are the neutron and proton density distributions normalized to the number of neutrons N and number of protons Z, respectively, $A = N + Z$, and M is the mass of the nucleon. The factor $(A-1)/A$ above, which was omitted from the potential for pions, is included here due to the larger mass of the $\bar{p}$. Because of the large cross section for annihilation of $\bar{p}$ on a single nucleon, the interaction is expected to be dominated by the imaginary part of the potential and the absorption of $\bar{p}$ is expected to take place at the extreme surface regions of the nucleus. As a result it is unlikely that $\bar{p}$ atoms will provide information on the potential deep into the nucleus and the above simplest $t\rho$ form is a useful starting point for analyzing antiprotonic atom data. Previous attempts to add to the potential a p-wave term or non linear terms [1, 181] are not found to be justified in a phenomenological approach when the overall picture is considered, respecting also constraints satisfied by neutron density distributions, as described below. More specifically, we find that an imaginary part of a p-wave potential compatible with the Paris potential [182, 183, 184] could be accommodated, but then Imb_0 is found to be incompatible with the Paris potential. These remarks apply particularly to analyses based on the high-quality data of the PS209 collaboration, which is the basis for the present analysis. However, an isovector term $b_1(\rho_n - \rho_p)$ is included in Eq. (59) because the present data base is rich with groups of isotopes of the same element.

Proton densities for the above potential are taken, as before, from the known charge distributions [10] by unfolding the finite size of the proton. For the neutrons it is, again, a matter of choosing an adequate model, that will be in line with the bulk of information on neutron densities [16]. The importance of the *shapes* of neutron density distributions ρ_n was realized long ago, when single-particle densities (SP) were found [1, 181] to produce better fits to the data of $\bar{p}$ atoms compared to fits based on the two-parameter Fermi (2pF) shape, because of the sensitivity of $\bar{p}$ atom data to the extreme outer reaches of the nucleus. An alternative to SP densities is to use simple parameterizations such as the 2pF form for ρ_n and to accommodate different shapes, relative to the protons, by taking the 'skin' or the 'halo' version for ρ_n [16], or their average. In what follows we adopt the latter approach for global fits to $\bar{p}$ data because in any case the SP densities are not particularly suitable for nuclei far removed from closed shells and because we are interested in average properties. We therefore use the approach of Sec. III D 2 with the parameterization of $r_n - r_p$ given by Eq. (8).

B. Antiprotonic atom data

As mentioned in Sec. II, the experimental situation with $\bar{p}$ atoms has changed significantly in the last decade with the publication by the PS209 collaboration [48] of high-quality data for several sequences of isotopes along the periodic table. This set of X-ray data has greater accuracies compared to older data used in earlier analyses, and thanks to the full coverage of the periodic table by these new data we do not mix in the present analysis old data with the new results but use only the PS209 results [48], including the revised experimental results for Cd, Sn and Te isotopes [185, 186] obtained after correcting for E2 resonance effects. In what follows we address only *spin-averaged* quantities for antiprotonic atoms within a global approach to the hadron-nucleus interaction.

Strong interaction effects in antiprotonic atoms are reported [48] as level shifts and widths for the lowest levels reached in the X-ray cascade and as 'upper' level widths deduced from the yields of the transitions, based on intensity ratios and calculations of the atomic cascade process. These yield values had been converted in Ref. [48] into upper level widths with the help of the calculated radiation widths. However, it is easy to see that χ^2 values for the deduced upper level widths may be different from the corresponding values calculated for the yields. As the yields are the experimentally determined quantities, we have converted the quoted upper level widths back to transition yields, and used these in the global χ^2 fits.

The X-ray data used in the present analysis are for the following nuclear targets: ^{16,18}O, ^{40,42,43,44,48}Ca, ^{54,56,57,58}Fe, ^{58,60,62,64}Ni, ^{90,96}Zr, ^{106,116}Cd, ^{112,116,120,124}Sn, ^{122,124,126,128,130}Te and ^{208}Pb, a total of 90 data points [48].

In addition to the conventional method of studying strong interaction effects by observation of X-ray emission from exotic atoms, there is for antiprotons a radiochemical method which is capable of providing information on the absorption of $\bar{p}$ by nuclei [187]. In brief, this method is based on the high probability for annihilation of $\bar{p}$ on a single peripheral nucleon which leads to a residual nucleus containing one neutron or one proton less than the target nucleus (Z, N). When the two residual nuclei $(Z, N-1)$ and $(Z-1, N)$ are radioactive, then measuring their activities can provide the *ratio* between the probability for $\bar{p}$ annihilation on a neutron to that on a proton. This is based on the reasonable assumption that following such extremely peripheral annihilation the resulting pions will not interact with the residual nucleus. Considering that the absorption takes place within a narrow range of radii in the outer surface region of nuclei, these ratios may provide information on the ratios between neutron and proton densities at that region, supplementing the information provided by the atomic X-rays.

Experimental ratios of $\bar{p}$ absorption on neutrons to absorption on protons were taken from Refs. [49, 50]. Initial calculations showed that very large contributions to the resulting χ^2 came from ^{106}Cd and ^{112}Sn and subsequently these two nuclei were excluded from the data set. Possible explanations for the problem with these two nuclei in terms of a $\bar{p}p$ quasi bound state are given in Ref. [188]. We have therefore used 17 values of absorption ratios for the following nuclei: ^{48}Ca, ^{58}Ni, ^{96}Zr, ^{100}Mo, ^{96,104}Ru, ^{116}Cd, ^{124}Sn, ^{128,130}Te, ^{144,154}Sm, ^{148}Nd, ^{160}Gd, ^{176}Yb, ^{232}Th and ^{238}U.

C. Analyses of antiprotonic atom X-ray data

Detailed analyses of the results of the PS209 collaboration have been published in a series of papers, dedicated each to a particular subset of the data such as neighboring nuclei or

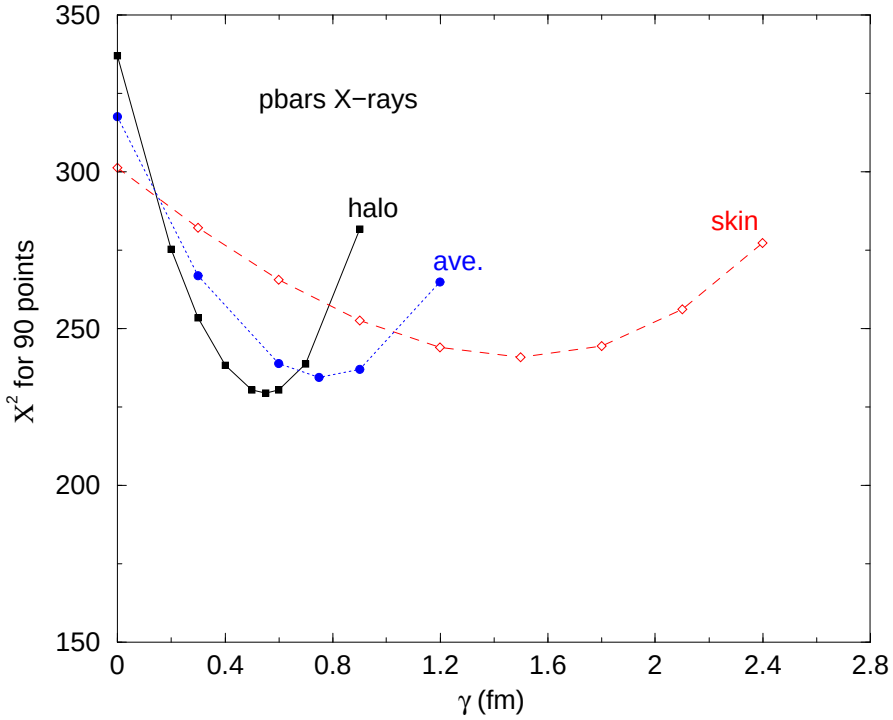

FIG. 31: Global best-fit χ^2 values for zero-range $\bar{p}$-nucleus potentials as function of the $r_n - r_p$ parameter γ of Eq.(8) for three shapes of the neutron density ρ_n.

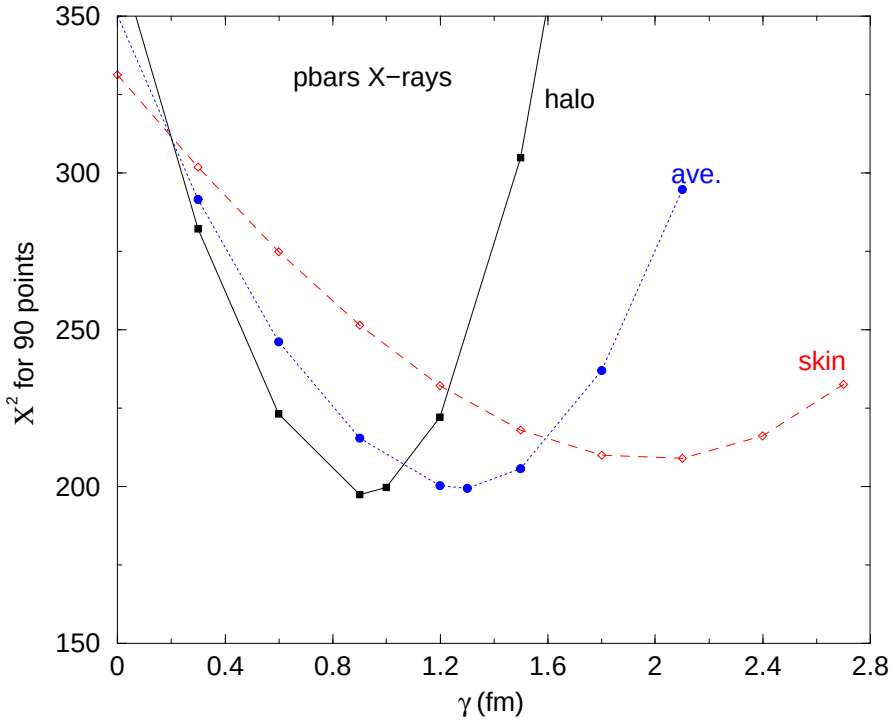

FIG. 32: Same as Fig. 31 but for finite-range potentials with a Gaussian parameter β=0.9 fm.

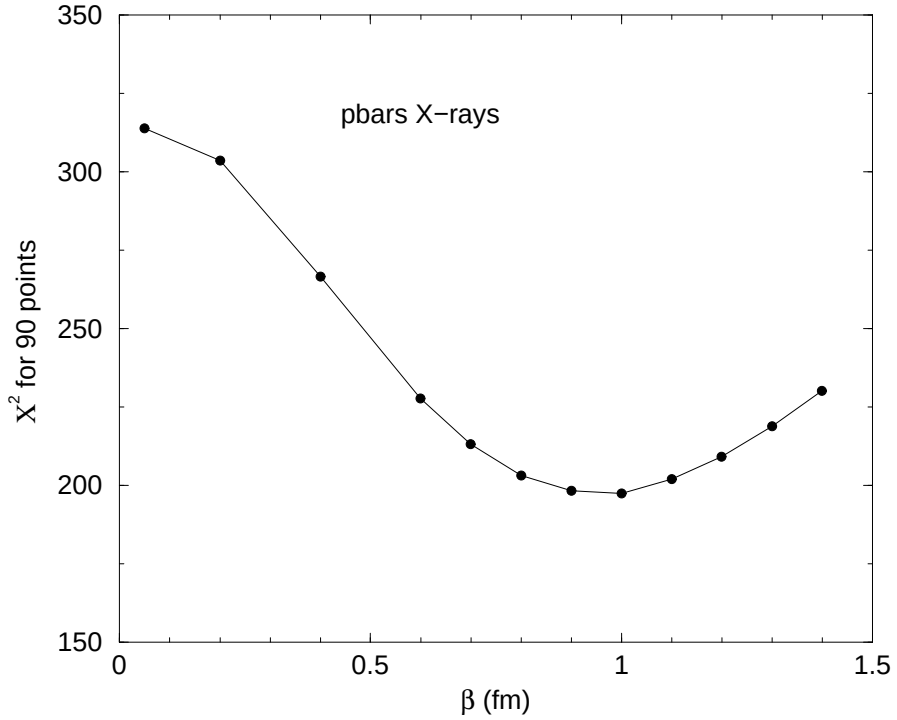

FIG. 33: Global best-fit χ^2 values as function of a Gaussian range β for the halo shape for ρ_n with γ=1.0 fm.

isotopes of the same element. In several cases it is necessary to take into consideration the effects of possible E2 resonances, when energy of a nuclear E2 transition is very close to the energy of the atomic transition being studied. In what follows we discuss only *global* fits to the entire data set of 90 points as part of a study of medium-modification of the $\bar{p}N$ interaction [19, 98].

Figure 31 shows the χ^2 values for the best-fit potential of the type Eq. (59) obtained with only two adjustable parameters, the real and imaginary parts of b_0. The halo shape for ρ_n yields the lowest value of χ^2 but the minimum at $\gamma \approx$0.5 fm is unacceptable as representing the average dependence of $r_n - r_p$ on the neutron excess, as discussed in Sec. III D 2. In Fig. 32 are shown similar results for a finite-range version of the potential, obtained with Gaussian folding, as given by Eq. (10), using a range parameter of β=0.9 fm. The lowest χ^2 is significanty lower than the corresponding value in Fig. 31 and is obtained for $\gamma \approx$0.9 fm, which is a most acceptable value, see Sec. III D 2 and Ref. [16]. The FR parameter β=0.9 fm is chosen because over a range of values of γ a minimum of χ^2 is obtained for this value of β=0.9 fm, as seen in Fig. 33. This minimum means a χ^2 per point of 2.2 which is quite good. The parameters of the potential are Reb_0=1.1$\pm$0.1 fm, Imb_0=1.8$\pm$0.1 fm for γ=1.0 fm and $\delta = -0.035$ fm, see Eq. (8). These parameters are not qualitatively distinct from the parameters obtained recently by Wycech et al. [189] using somewhat different values for β and γ, and also including a p-wave absorptive term in the $\bar{p}$ optical potential.

Figure 34 shows results when the isovector parameter b_1 is varied in the fit in addition to the isoscalar parameter b_0. It is found that Reb_1 is always consistent with zero (not shown) whereas the other three parameters vary monotonically with the neutron radius parameter γ. It is seen that the minimum of χ^2 is obtained for the same value of $\gamma \approx$1.0 fm as before

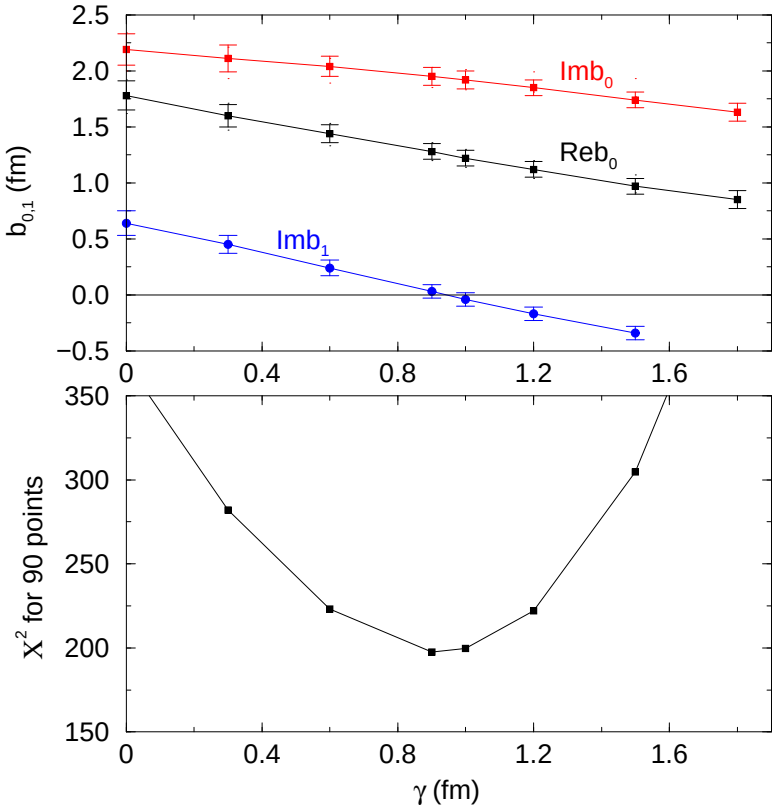

FIG. 34: Global best-fits for FR $\bar{p}$-nucleus potentials with β=0.9 fm as function of the $r_n - r_p$ parameter γ of Eq. (8) for the halo shape of the neutron density ρ_n including an isovector term Imb_1.

and the quality of fit is not improved. Moreover, at the best-fit point Imb_1 is consistent with zero. Note that a non-zero value for this parameter will be obtained if a very different value of γ is used to represent neutron densities.

It is interesting to make a few comparisons between the values of the differences between rms radii of neutron and of proton distributions implied by the global best-fit value of γ=1.0 fm, and differences obtained in detailed analyses of a small group of $\bar{p}$ atoms. For example, for ^{120}Sn it is found in Ref. [185] that $r_n - r_p = 0.08^{+0.03}_{-0.04}$ fm whereas our global expression yields 0.13±0.02 fm for this difference if we assign from Fig. 32 an estimated uncertainty of ±0.1 fm to the slope parameter γ. Likewise for ^{124}Sn the values are 0.14±0.03 fm from Ref. [185] and 0.16±0.02 fm from the present global analysis. Taking ^{208}Pb as another example, in Ref. [190] the rms difference is 0.16±0.04 fm whereas the present global expression leads to 0.18±0.02 fm. Similar agreements are found in other cases.

D. Radial sensitivity of X-ray data

Before proceeding to the radiochemical results which provide information on the annihilation of atomic $\bar{p}$ at the extreme periphery of the nucleus, it is instructive to examine the radial sensitivity of X-ray data in order to get some idea on what are the nuclear regions that determine the potentials derived above. Following the preliminary results of the 'notch

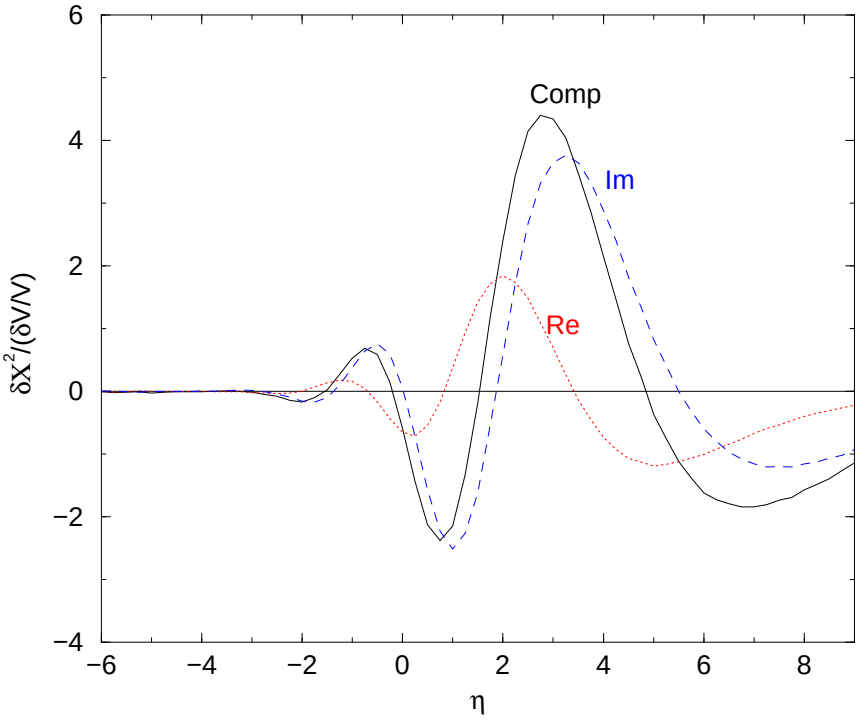

FIG. 35: Functional derivatives of the global best-fit χ^2 with respect to relative changes in the full complex potential (solid curve), in the real part (dotted) and in the imaginary part (dashed) of the potential as function of the radial position η, see Sec. III D 4.

test' of Ref. [1] where it was shown that $\bar{p}$ X-ray data are sensitive to the potential at radii well outside of the nuclear surface, we apply here the functional derivative method, as discussed in Sec. III D 4. Figure 35 shows the χ^2 FDs for the best-fit potential with γ=1.0 fm, $\delta = -0.035$ fm, a Gaussian range of 0.9 fm and with b_0=1.1+i1.8 fm. The first conclusion from this figure is the dominance of the imaginary part of the potential as the FD with respect to it follows closely the FD with respect to the full complex potential. The other clear feature are the radial regions where the bulk of |FD| is found, indicating the regions to which the data are sensitive. Strictly speaking, the FD refers to the optical potential and owing to the finite-range folding the relevant density regions are shifted to approximately 0.5 fm smaller radii, well outside of the half-density radius (at η=0), peaking between η=2 and η=6 where the densities are well below 10% of the central nuclear density.

E. Analysis of X-ray and radiochemical data

In the analysis of radiochemical data we adopt the approach of Refs. [18, 49, 50], namely that the method is sensitive to the neutron to proton density ratio close to 2.5 fm outside of the half-density radius of the charge density [191]. In terms of the global parameter η defined above, that corresponds to $\eta \approx 5$, which is within the region of sensitivity of the X-ray data but slightly shifted towards larger radii, as seen from Fig. 35. It is therefore interesting to see if analyses of the radiochemical data lead to results consistent with what is obtained from the X-ray data. The experimental ratios of absorption on neutrons to absorption on

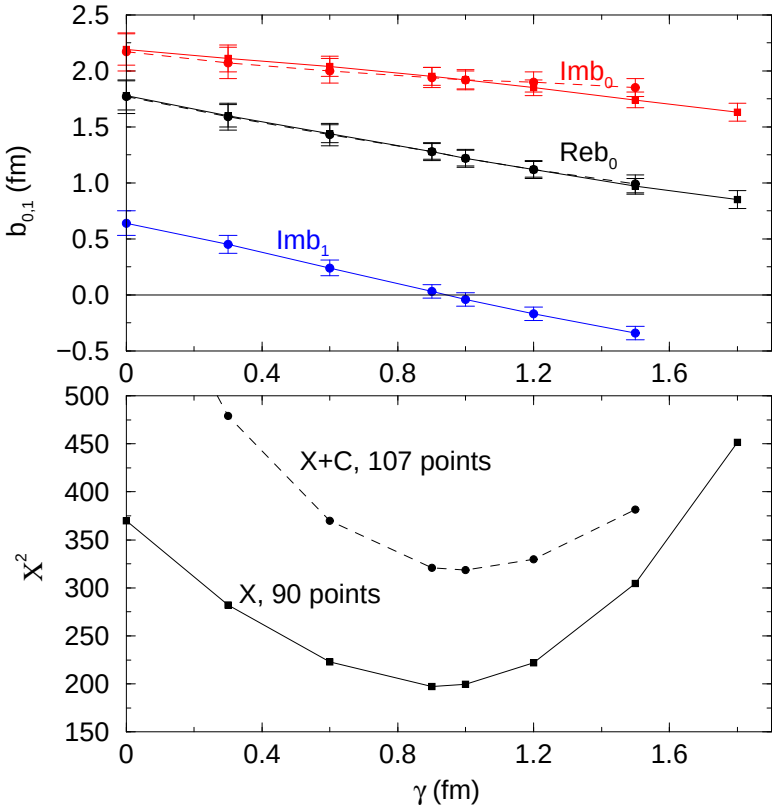

FIG. 36: Fits to the combined X-ray and radiochemical data (X+C, dashed curves) compared to fits to the X-ray data (X, solid curves) only.

protons were therefore compared to

$$\frac{\mathrm{Im}(b_0 + b_1)I_n}{\mathrm{Im}(b_0 - b_1)I_p} \tag{60}$$

where $I_{n,p}$ are the volume integrals of the neutron and proton densities, respectively, over an appropriate range. To check sensitivity to the chosen range of integration we have carried out the integration either between 2.0 and 3.0 fm or between 2.5 and 3.5 fm outside of the half-density radius of the charge density. For the finite-range potential used here the folded densities were used. Atomic wavefunctions were not included in the integrals because their effect largely cancels out in the ratios. Moreover, we note that choosing the range of integration was guided by the conclusions of Ref. [191] which were based on properties of the atomic wavefunctions. With the potential parameter b_1 consistent with zero the ratios Eq. (60) become independent of the parameters of the potential, but they are found to be sensitive to values of $r_n - r_p$ or to the parameter γ. Examining the χ^2 for the radiochemical data as function of γ, it was found [19] that the minimum occurred for $\gamma \approx 1.0$ fm, as was the case for the X-ray data, if the integration range was 2.5 to 3.5 fm (but not 2 to 3 fm) outside of the half-density radius of the charge density. This result confirms in a phenomenological way the theoretical conclusion of Wycech et al. [191] that most of the absorption takes place close to 2.5 fm beyond the charge radius. Note that due to the exponential decrease of the densities at such large radii the integrals are dominated by the densities close to the lower limit of the range of integration.

Combining the results of the radiochemical technique with the X-ray data, fits were made to the two kinds of data put together, a total of 107 points. From Fig. 36 showing results of fits to this combined data set, in comparison with results from fits to the X-ray only data, it is seen that the overall picture is the same in both cases, with larger values of χ^2 per point for the combined data. In particular, with the minimum of χ^2 for the same value of γ, the same conclusions are reached regarding neutron densities.

Before closing this section we look into the broader perspective of neutron densities in nuclei obtained from antiprotonic atoms. The following conclusions may be made from the global analyses presented above:

- The potential parameters depend mostly on $r_n - r_p$ and not on the shape of the neutron densities, although the χ^2 values do depend on the shape of ρ_n.
- The favored shape of ρ_n is of the 'halo' type,
- The rms radii of ρ_n are given on the average by Eq. (8) with the parameter $\gamma \approx 1.0$ fm.

A possible difficulty regarding nuclear densities is that the sensitivity of $\bar{p}$ atom data is to extremely small densities, of the order of 5% of the central nuclear density, where the proton densities too are not determined well by the traditional methods of electron scattering and muonic X-rays. In particular, the 2pF parameterization need not be appropriate to describe the outer reaches of the proton densities ρ_p. On the other hand, the present analyses of $\bar{p}$ atomic data lead only to conclusions on *differences* between neutrons and protons in $N \neq Z$ nuclei, both on the differences of rms radii and on differences in shapes. The preferred 'halo' shape in this context means that the diffuseness parameter a_n is larger than the corresponding parameters for protons, which is quite reasonable considering the binding energies of least bound nucleons and effects of the Coulomb potential. The disagreement with pionic atoms regarding the shapes of ρ_n is presumably due to the extreme simplification introduced in assuming 2pF parameterizations for the densities. Recall that pionic atom data are sensitive to densities up to the full nuclear density. It is, therefore, no wonder that there are some differences in conclusions obtained from experiments that are sensitive to different density regions of the nucleus. The fact that the rms radii obtained with the two methods are in full agreement with each other is not a coincidence. It was shown in Sec. III D 2 that potential parameters for pions depend mostly on $r_n - r_p$ and not on the shape of the neutron densities. The same results are found for $\bar{p}$ atoms, as emphasized above.

F. Deeply bound antiprotonic atom states

Much the same as with kaonic atoms, see Sec. IV E, the optical potential for antiprotonic atoms is dominated by its imaginary part which is of the order of 100 MeV deep when extrapolated into the full nuclear density. Such an absorption inevitably produces strong suppression of the *atomic* wavefunction inside the nucleus, which for a normalized atomic wavefunction located mostly outside of the nucleus is equivalent to repulsion. The role of the phenomenological attractive real part of the potential is more difficult to visualize. For sufficiently attractive potentials there is the possibility of accommodating strongly bound nuclear states, albeit very broad, as their wavefunctions are confined to the nuclear volume. Due to the orthogonality requirement of nuclear and atomic wavefunctions having the same l-values, the latter might be shifted considerably by the real potential, as demonstrated

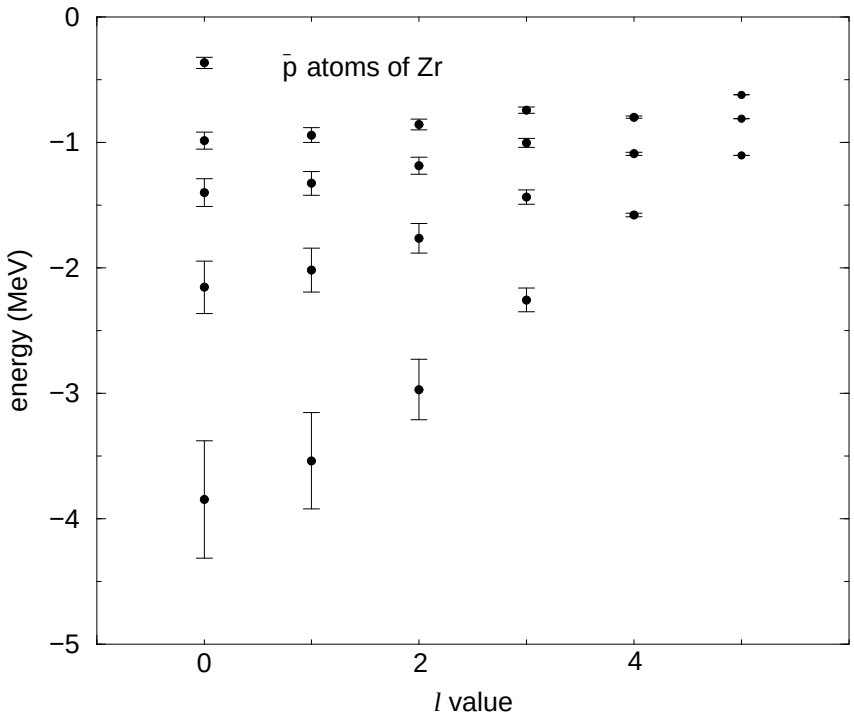

FIG. 37: Calculated energies of $\bar{p}$ atomic states in ^{90}Zr. The lowest energy for each l value corresponds to $n = l + 1$. The bars represent the widths of the states.

for kaonic atoms in Fig. 25, where large repulsion of the atomic wavefunction is observed as a result of an attractive strong interaction. It is, therefore, not surprising, that the phenomenon of saturation of widths of atomic states is observed [133, 134] in numerical calculations of antiprotonic atom spectra.

Figure 37 shows a calculated energy spectrum for $\bar{p}$ atoms of Zr as a typical medium-weight nucleus [134]. The strong-interaction potential is taken from global fits to $\bar{p}$ atomic data. The saturation of the widths is easily seen, with the widths increasing very little when l goes down towards l=0.

G. Antiproton-nucleus interaction across threshold

With rather well-established phenomenology of the interaction of antiprotons with nuclei in the subthreshold atomic regime, it is of interest to see if the same picture prevails also above threshold. Indeed early analyses of elastic scattering of 47 MeV antiprotons on carbon showed [192] that very good fits to the scattering data and to the then available $\bar{p}$ atom data could be obtained with a common optical potential, dominated by its imaginary part and based on Gaussian folding with a range parameter of β=1.2 fm, quite similar to the present results.

Antiprotons offer a unique tool, compared to other exotic atoms, for studying the interaction with nuclei very close to, but above threshold, in the form of $\bar{p}$ annihilation. At very low energies, below the $\bar{p}p \to \bar{n}n$ charge-exchange threshold, the total $\bar{p}$ reaction cross section consists only of $\bar{p}$ annihilation. Therefore measurements of annihilation cross sections at such low energies may be compared with total reaction cross sections calculated

with the optical potentials obtained from fits to antiprotonic atom data. A measurement of antiproton annihilation cross section at 57 MeV/c (1.7 MeV kinetic energy) on Ne was reported by Bianconi et al. [45] and was shown [193] to agree with predictions made with potentials obtained from global fits to $\bar{p}$ atom data. Comparisons for similar measurements of $\bar{p}$ annihilation on ^{4}He showed that predictions of annihilation cross sections made with $\bar{p}$ potentials obtained from fits to atomic data for medium-weight and heavy nuclei, do not agree with experiment. In contrast, when parameters of the potential were obtained from fits only to $\bar{p}$ atoms of ^{3,4}He, then the predicted annihilation cross section on ^{4}He agreed with the measured one. From this example it may be concluded that the $\bar{p}$-nucleus potentials cross smoothly the threshold from atomic states to the scattering regime. On the other hand the global $\bar{p}$ potentials which reproduce very well $\bar{p}$ atomic data for targets heavier than $A \approx$10, fail to describe similar data for the He isotopes.

A special case in this context is the annihilation of $\bar{p}$ on the proton very close to threshold. The $\bar{p}p$ total annihilation cross section was measured at four momenta between 38 and 70 MeV/c [46] and with the availability of strong interaction shift, width and yield for the $1s$ and $2p$ levels in antiprotonic hydrogen it is possible to study the $\bar{p}p$ interaction across threshold [194]. It is found that a Gaussian potential with a range parameter between 1 and 2 fm produces very good fits separately to the annihilation cross sections and to the atomic $\bar{p}$H data, but if both types of data are to be fitted together then the range parameter turns out to be β=1.5±0.15 fm with Re$b_0 = -0.15\pm0.15$ fm, Imb_0=1.80±0.06 fm. It is, therefore, possible to cross smoothly the borderline of E=0 also for the $\bar{p}$H system. However, the interaction parameters are different from those valid for ^{3,4}He and from those valid for target nuclei heavier than $A \approx$10. This demonstrates the limitations of using optical potentials down to the very light nuclear targets, where the energy dependence of those $\bar{N}N$ partial-wave amplitudes which may have quasibound states or resonances near threshold needs to be considered explicitly [195, 196].

Finally, it is interesting to note that the saturation of widths predicted for antiprotonic atom states is also predicted and *observed* above threshold in the form of saturation of reaction cross sections [194]. There is an interesting analogy between widths of bound states and total reaction cross sections where for the Schrödinger equation the latter is given by

$$\sigma_R = -\frac{2}{\hbar v}\int \mathrm{Im}V_{\mathrm{opt}}(r)|\psi(\mathbf{r})|^2 d\mathbf{r} \quad , \tag{61}$$

where $\psi(\mathbf{r})$ is the $\bar{p}$-nucleus elastic scattering wavefunction and v is the c.m. velocity. Recall that the width of a bound state, as discussed in Secs. III C and IV E is given by

$$\Gamma = -2\frac{\int \mathrm{Im}V_{\mathrm{opt}}(r)|\psi(\mathbf{r})|^2 d\mathbf{r}}{\int |\psi(\mathbf{r})|^2 d\mathbf{r}} \quad , \tag{62}$$

where $\psi(\mathbf{r})$ is the $\bar{p}$ full atomic wavefunction. The modification of this expression for the KG equation is mentioned in Sec. IV E. It is therefore to be expected that large local variations of the wavefunction, in both cases, is a common mechanism behind departures from linear dependence on the imaginary potential.

At very low antiproton energies where Coulomb focusing is effective, the annihilation cross sections on nuclei are expected to scale as $ZA^{1/3}$ in the perturbative regime [194], but the experimental annihilation cross sections on Ne and ^{4}He [45] differ strongly from this scaling law. This difference is a manifestation of saturation [193, 194], confirming the general property of saturation of widths as discussed above.

VII. THE REPULSIVE Σ NUCLEAR POTENTIAL

A. Preview

One Boson Exchange (OBE) models fitted to the scarce low-energy YN scattering data produce within a G-matrix approach, with one exception (Nijmegen Model F), as much attraction for the Σ nuclear potential as they do for the Λ nuclear potential, see Ref. [197] for a review of 'old' models and Ref. [198] for the latest state of the art for Nijmegen models. Indeed, the best-fit $t_{\rm eff}\rho$ potential for Σ^- atoms was found by Batty et al. [199, 200] to be attractive and absorptive, with central depths for the real and imaginary parts of 25-30 MeV and 10-15 MeV, respectively. It took almost a full decade, searching for Σ hypernuclear bound states at CERN, KEK and BNL, before it was realized that except for a special case for ${}^{4}_{\Sigma}$He, the observed continuum Σ hypernuclear spectra indicate a very shallow, or even repulsive Σ nuclear potential, as reviewed by Dover et al. [201]. These indications have received firm support with the measurement of several $(K^-,\pi^\pm)$ spectra at BNL [202] followed by calculations for ^{9}Be [203]. Recently, with measurements of the Σ^- spectrum in the (π^-,K^+) reaction taken at KEK across the periodic table [51, 204], it has become established that the Σ nuclear interaction is strongly repulsive. In parallel, analyses of Σ^--atom in the early 1990s, allowing for density dependence or departure from the $t\rho$ prescription, motivated mostly by the precise data for W and Pb [205], led to the conclusion that the *nuclear* interaction of Σs is dominated by repulsion [206, 207, 208], as reviewed in Ref. [1]. This might have interesting repercussions for the balance of strangeness in the inner crust of neutron stars [209], primarily by delaying the appearance of Σ^- hyperons to higher densities, if at all. The inability of the Nijmegen OBE models, augmented by G-matrix calculations [198], to produce Σ nuclear repulsion is a serious drawback for these models at present. This problem apparently persists also in the Juelich model approach [210]. The only theoretical works that provide exception are SU(6) quark-model RGM calculations by the Kyoto-Nijata group [211], in which a strong Pauli repulsion appears in the $I = 3/2$, ${}^3S_1 - {}^3D_1$ ΣN channel, and Kaiser's SU(3) chiral perturbation calculation [212] which yields repulsion of order 60 MeV.

Below we briefly review and update the Σ^- atom fits and the recent (π^-,K^+) KEK results and their analysis.

B. Density dependent Σ nuclear potentials from fits to Σ^- atoms

Batty et al. [206, 207] analyzed the full data set of Σ^- atoms, consisting of strong-interaction level shifts, widths and yields, in order to constrain the density dependence of $V_\Sigma(r)$. By introducing a phenomenological density dependent (DD) potential of the isoscalar form

$$V_\Sigma(r) \sim [b_0 + B_0\,(\rho(r)/\rho(0))^\alpha]\,\rho(r) \quad , \qquad \alpha > 0 \quad , \tag{63}$$

and fitting the parameters b_0, B_0 and α to the data, greatly improved fits to the data are obtained. Isovector components are readily included in Eq. (63) but are found to have a marginal effect. Note, however, that the absorption was assumed to take place only on protons. The complex parameter b_0 may be identified with the spin-averaged $\Sigma^- N$ scattering length. For the best-fit isoscalar potentials, ReV_Σ is attractive at low densities outside the

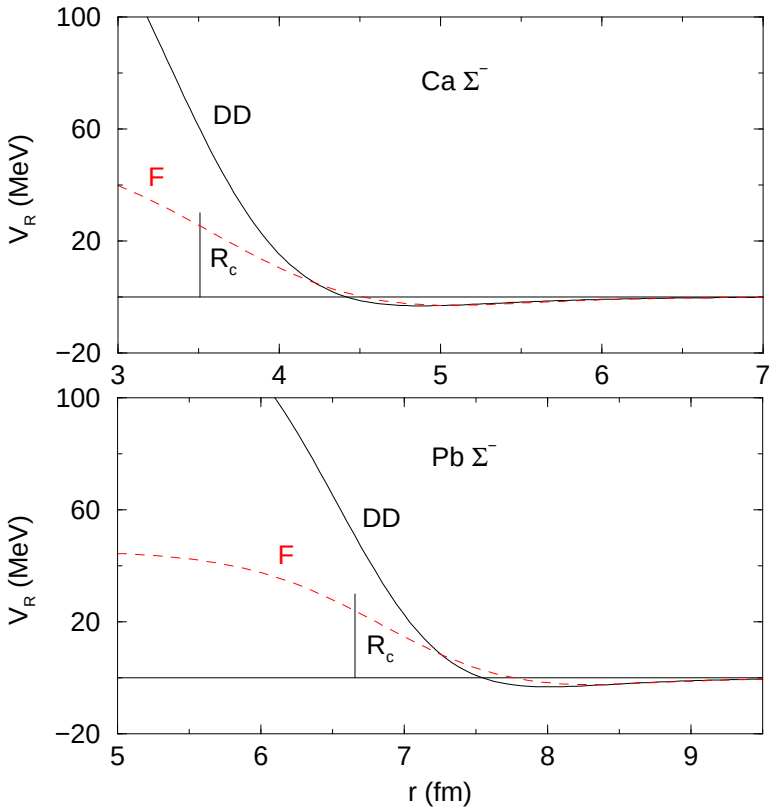

FIG. 38: Re$V_{\rm opt}$ for DD (solid) and for the geometrical model F (dashed) Σ^- nuclear potentials fitted to Σ^- atomic data. Vertical bars indicate the half-density radius of the nuclear charge distribution.

nucleus, changing into repulsion in the nuclear surface region. The precise magnitude and shape of the repulsive component within the nucleus is not determined by the atomic data. The resulting potentials are shown in Fig. 38 (DD, solid lines), where it is worth noting that the transition from attraction to repulsion occurs well outside of the nuclear radius, hence the occurrence of this transition should be largely model independent. To check this last point we have repeated the fits to the atomic data with the 'geometrical model' F of Sec. IV, using separate $t\rho$ expressions in an internal and an external region, see Eq. (48). The neutron densities used in the fits were of the skin type, with the $r_n - r_p$ parameter Eq. (8) γ=1.0 fm. The fits deteriorate significantly if the halo type is used for the neutron density. The fit to the data is equally good with this model as with the DD model, (χ^2 per degree of freedom of 0.9 here compared to 1.0 for the DD model) and the potentials are shown as the dashed lines in Fig. 38. The half-density radius of the charge distribution is indicated in the figure. It is clear that both models show weak attraction at large radii, turning into repulsion approximately one fm outside of that radius.

Further insight into the geometry of the Σ-nucleus interaction is gained by inspecting the functional derivatives (FD) of χ^2 with respect to the optical potentials, see Sec. III D 4. Figure 39 shows the FDs based on the best fit of the geometrical model F as discussed above. From the differences between the FD with respect to the full complex potential and the FD with respect to the real potential it is concluded that both real and imaginary parts play similar roles in the Σ-nucleus interaction. The bulk of |FD| is in the range of $0.5 \leq \eta \leq 6$,

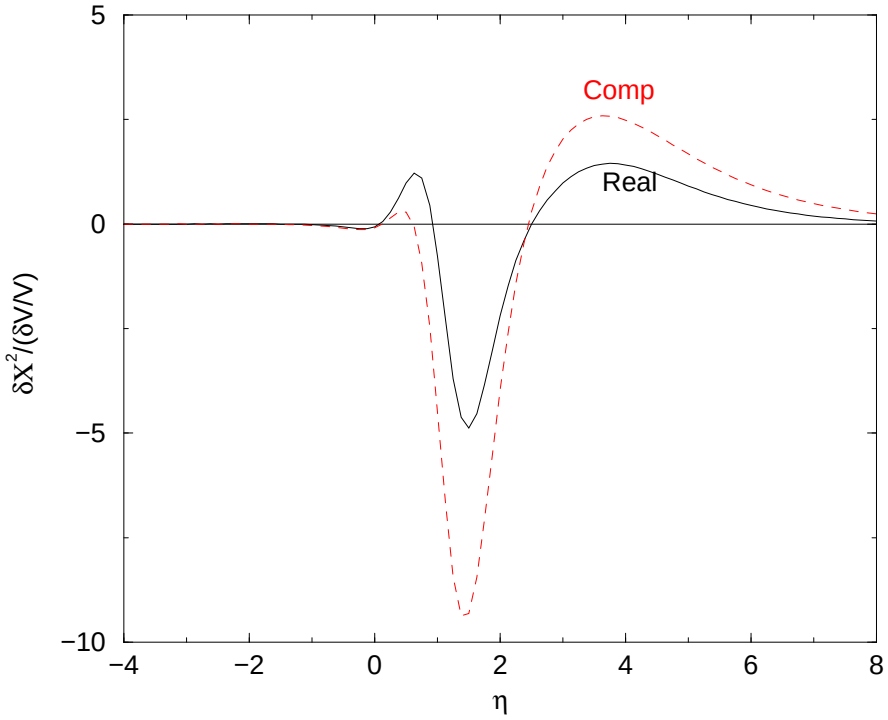

FIG. 39: Functional derivatives of χ^2 with respect to the real (solid) and with respect to the full complex (dashed) optical potentials for the best fit F potential.

covering the radial region where the weak attraction turns into repulsion. Obviously no information is obtained from Σ^- atoms on the interaction inside the nucleus. It is also interesting to note quite generally that such potentials do not produce bound states, and this conclusion is in agreement with the experimental results from BNL [202] for the absence of Σ hypernuclear peaks beyond He.

Some semi-theoretical support for this finding of inner repulsion is given by RMF calculations by Mareš et al. [208] who generated the Σ-nucleus interaction potential in terms of scalar (σ) and vector (ω, ρ) meson mean field contributions, fitting its coupling constants to the relatively accurate Σ^- atom shift and width data in Si and in Pb. The obtained potential fits very well the whole body of data on Σ^- atoms. This potential, which is generally attractive far outside the nucleus, becomes repulsive at the nuclear surface and remains so inward in most of the acceptable fits, of order 10-20 MeV. The Pb data [205] are particularly important in pinning down the isovector component of the potential which in this model is sizable and which, for Σ^-, acts against nuclear binding in core nuclei with $N - Z > 0$, countering the attractive Coulomb interaction. On the other hand, for very light nuclear cores and perhaps only for $A = 4$ hypernuclei, this isovector component (Lane term) generates binding of Σ^+ configurations. In summary, the more modern fits to Σ^- atom data [206, 207, 208] and the present fits with the geometrical model support the presence of a substantial repulsive component in the Σ-nucleus potential which excludes normal Σ-nuclear binding, except perhaps in very special cases such as ${}^{4}_{\Sigma}$He [213, 214, 215, 216].

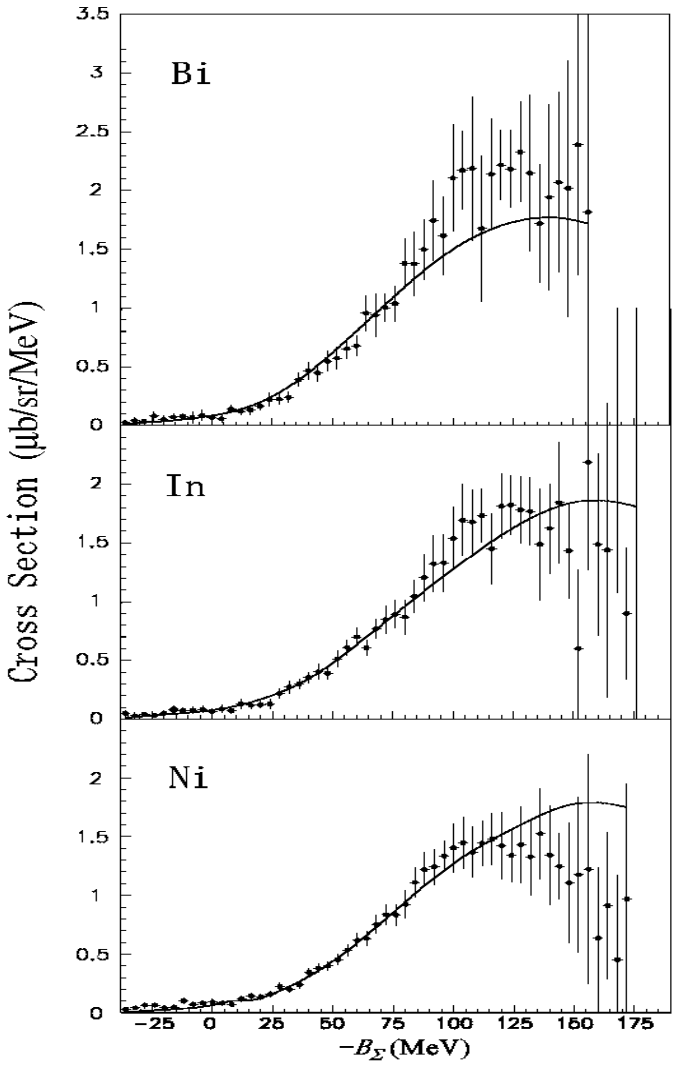

FIG. 40: Inclusive (π^-, K^+) spectra on Ni, In and Bi, fitted by a Σ-nucleus WS potential with depths $V_0 = 90$ MeV, $W_0 = -40$ MeV [51].

C. Evidence from $(\pi^-, \mathbf{K}^+)$ spectra

A more straightforward information on the nature of the Σ-nuclear interaction has been provided by recent measurements of inclusive (π^-, K^+) spectra on medium to heavy nuclear targets at KEK [51, 204]. The inclusive (π^-, K^+) spectra on Ni, In and Bi are shown in Fig. 40 together with a fit using Woods-Saxon potentials with depths $V_0 = 90$ MeV for the (repulsive) real part and $W_0 = -40$ MeV for the imaginary part. These and other spectra measured on lighter targets suggest that a strongly *repulsive* Σ-nucleus potential is required to reproduce the shape of the inclusive spectrum, while the sensitivity to the imaginary (absorptive) component is secondary. The favored strength of the repulsive potential in this analysis is about 100 MeV, of the same order of magnitude reached by the DD Σ^- atomic fit potential shown in Fig. 38 as it 'enters' the nucleus inward. The general level of agreement in the fit shown in Fig. 40 is satisfactory, but there seems to be a systematic effect calling for more repulsion, the heavier is the target. We conclude that a strong evidence has been

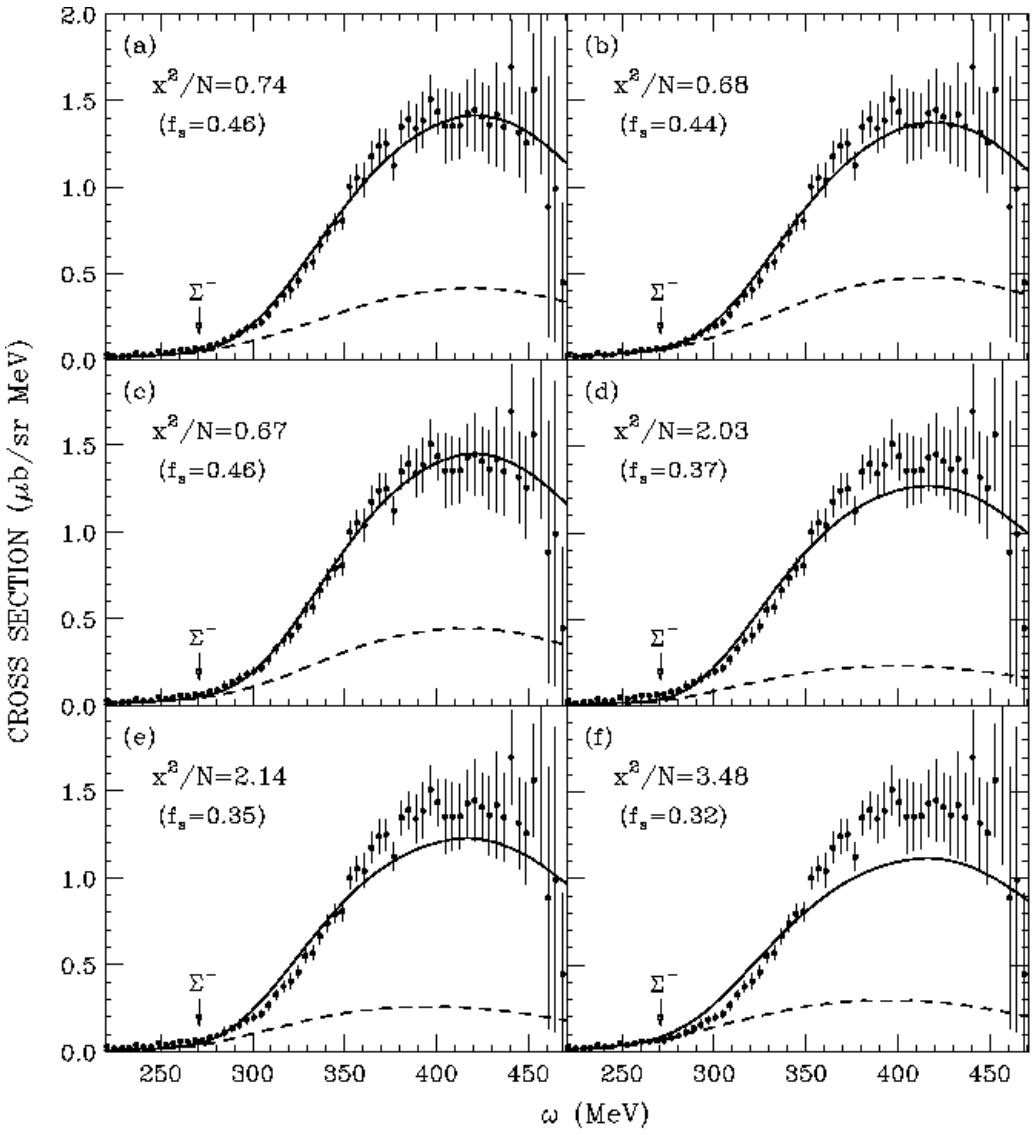

FIG. 41: Comparison between DWIA calculations [219] and the measured ^{28}Si(π^-, K^+) spectrum [51] using six Σ-nucleus potentials, (a)-(c) with inner repulsion, (d)-(f) fully attractive. The solid and dashed curves denote the inclusive and Λ conversion cross sections, respectively. Each calculated spectrum was normalized by a fraction f_s. The arrows mark the $\Sigma^- - {}^{27}\mathrm{Al}_{\mathrm{g.s.}}$ threshold at $\omega = 270.75$ MeV.

finally established for the repulsive nature of the Σ-nucleus potential.

More sophisticated theoretical analyses of these KEK (π^-, K^+) spectra [217, 218, 219, 220] have also concluded that the Σ-nuclear potential is repulsive within the nuclear volume, although they yield a weaker repulsion in the range of 10-40 MeV. An example of a recent analysis of the Si spectrum is shown in Fig. 41 from Ref. [219] where six different Σ-nucleus potentials are tested for their ability within the Distorted Wave Impulse Approximation (DWIA) to reproduce the measured ^{28}Si(π^-, K^+) spectrum [51]. This particular DWIA version was tested on the well understood ^{28}Si(π^+, K^+) quasi-free Λ hypernuclear spectrum also taken at KEK with incoming pions of the same momentum $p_{\mathrm{lab}} = 1.2$ GeV/c. Potential (a) is the DD, type A' potential of Ref. [207], (b) is one of the RMF potentials of Ref. [208],

that with $\alpha_\omega = 1$, and (c) is a local-density approximation version of a G matrix constructed from the Nijmegen model F. These three potentials are repulsive within the nucleus but differ considerably there from each other. Potentials (d)-(f) are all attractive within the nucleus, with (f) being of a $t_{\rm eff}\rho$ form. All of the six potentials are attractive outside the nucleus, as required by fits to the 'attractive' Σ^- atomic level shifts. The figure shows clearly, and judging by the associated χ^2/N values, that fully attractive potentials are ruled out by the data and that only the *'repulsive'* Σ-nucleus potentials reproduce the spectrum very well, but without giving preference to any of these potentials (a)-(c) over the other ones in this group. It was shown by Harada and Hirabayashi [220], furthermore, that the (π^-, K^+) data on targets with neutron excess, such as ^{209}Bi, also lack the sensitivity to confirm the presence of a sizable (repulsive for Σ^-) isovector component of the Σ nucleus interaction as found in the Σ^--atom fits [206, 207, 208].

VIII. Ξ HYPERONS

Experiments on exotic atoms of Ξ^- hyperons have not been reported so far but the possibilities of conducting such experiments have been discussed by Batty et al. [221] in some detail. Here we summarize only the main features of that study, within the broader context of the present Review.

A. Preview

Dedicated experiments with stopped Ξ^- hyperons had been proposed in Refs. [222, 223, 224] in order to produce some of the lightest $\Lambda\Lambda$ hypernuclei, ${}^{\;\;6}_{\Lambda\Lambda}$He and ${}^{\;\;4}_{\Lambda\Lambda}$H (if the latter is particle stable), and ${}^{12}_{\Lambda\Lambda}$B, respectively, by looking for a peak in the outgoing neutron spectrum in the two-body reaction

$$\Xi^- \; + \; {}^{A}Z \; \longrightarrow \; {}^{\;\;A}_{\Lambda\Lambda}(Z-1) \; + \; n\,. \tag{64}$$

These proposals motivated the AGS experiment E885 [225] on ^{12}C, using a diamond target to stop the Ξ^- hyperons resulting from the quasi-free peak of the $p(K^-, K^+)\Xi^-$ initial reaction. An upper bound of a few percent was established for the production of the ${}^{12}_{\Lambda\Lambda}$B hypernucleus. The experimental evidence for ${}^{\;\;6}_{\Lambda\Lambda}$He and ${}^{\;\;4}_{\Lambda\Lambda}$H had to await different techniques [226, 227], although the evidence for the latter species remains controversial. The stopped Ξ^- reaction in deuterium, $(\Xi^- d)_{\rm atom} \to Hn$, was used in the AGS experiment E813 to search for the doubly strange H dibaryon, yielding a negative result [228]. A similar search by the KEK E224 collaboration, stopping Ξ^- on a scintillating fiber active carbon target, also yielded a negative result [229]. On the positive side, following the discovery of a double-Λ hypernucleus [230] in light emulsion nuclei by the KEK stopped Ξ^- experiment E176, and its interpretation due to ${}^{13}_{\Lambda\Lambda}$B [231], this experiment gave evidence for several events, each showing a decay into a pair of known single Λ hypernuclei [232, 233]. One could then attempt to use these events in order to deduce properties of the initial Ξ^- atomic states. However, the typical error of 100 keV incurred in emulsion work is three orders of magnitude larger than the anticipated sensitivity of strong-interaction shifts and widths of Ξ^- atomic levels to the Ξ-nucleus strong interaction. This simple argument provides a major justification for pursuing a program of measuring Ξ^- X rays, in parallel to more conventional strong-interaction reactions involving Ξ hyperons, as discussed in Sec. VIII B.

Very little is established experimentally or phenomenologically on the interaction of Ξ hyperons with nuclei. Dover and Gal [234], analyzing old emulsion data which had been interpreted as due to Ξ^- hypernuclei, obtained an attractive Ξ-nucleus interaction with a nuclear potential well depth of $V_0^{(\Xi)}$= 21-24 MeV. This range of values agreed well with their theoretical prediction [197] for Ξ in nuclear matter, using model D of the Nijmegen group [235] to describe baryon-baryon interactions in an SU(3) picture, in contrast with the Ξ-nucleus repulsion obtained using model F [236]. Similar predictions were subsequently made with more detailed G matrix evaluations by Yamamoto et al. [237, 238, 239] who argued for a considerable A dependence of $V_0^{(\Xi)}$, such that the well depth for light and medium weight nuclei is significantly lower than for heavy nuclei where it approaches the value calculated for nuclear matter. It should be noted, however, that the predictions of the Nijmegen hard-core models D and F are extremely sensitive to the values assumed for the hard-core radius. The confidence in the predictive power of model D in strangeness -2 hypernuclear physics was to a large extent due to its success to yield the substantial attractive $\Lambda\Lambda$ interaction which was deemed necessary to reproduce the three known $\Lambda\Lambda$ binding energies in the 1990s. This picture has changed during the last decade for several reasons, as follows.

- Inclusive (K^-, K^+) spectra taken at the KEK-PS and at the BNL-AGS accelerators on ^{12}C, Refs. [240, 241] respectively, when fitted near the Ξ^--hypernuclear threshold yield more moderate values for the attractive Ξ well depth, $V_0^{(\Xi)} \sim 15$ MeV.

- The uniquely identified ${}^{6}_{\Lambda\Lambda}$He hypernucleus [226] implies a considerably weaker $\Lambda\Lambda$ interaction than produced by reasonable versions of Model D. In particular, the Nijmegen soft-core potentials NSC97 [242] provide a more realistic framework for reproducing the weaker strength of the $\Lambda\Lambda$ interaction, as discussed in Refs. [243, 244].

- New versions of Nijmegen extended soft-core potentials ESC04 [198, 245] predict a weak Ξ-nucleus interaction with a delicate pattern of spin and isospin dependence. Similar conclusions are also reached in spin-flavor SU(6) quark models by Fujiwara et al. [246, 247].

Looking ahead at the prospects of further research in this strangeness -2 sector, it is safe to argue that if the interaction of Ξ hyperons with nuclei is sufficiently attractive to cause binding, as has been repeatedly argued since the original work of Dover and Gal [234], then a rich source of spectroscopic information would become available and the properties of the in-medium ΞN interaction could be extracted. Bound states of Ξ hypernuclei would also be useful as a gateway to form double Λ hypernuclei [248, 249, 250, 251]. Finally, a minimum strength for $V_0^{(\Xi)}$ of about 15 MeV is required to realize the exciting possibility of 'strange hadronic matter' [252], where protons, neutrons, Λs and Ξs are held together to form a system which is stable against strong-interaction decay. The study of Ξ-nuclear interactions, as part of studying strangeness -2 hadronic and nuclear physics, is high on the agenda of two forthcoming major high-intensity hadron facilities.

- At J-PARC, Japan, the main accelerator ring is a 50-GeV proton synchronton and the proton beam, with 30 GeV energy and 9μA current initially, will produce various high-intensity beams of secondary particles. Strangeness -2 physics will be explored with a K^- beam at $p_{\rm lab} = 1.8$ GeV/c. An approved day-1 experiment is *Spectroscopic study of*

the Ξ-hypernucleus ${}^{12}_{\Xi}Be$ *via the* ${}^{12}C(K^-, K^+)$ *reaction* (T. Nagae, Spokesperson [253]). The overall energy resolution in the Ξ^- bound-state region is expected to be better than 3 MeV at FWHM, using an improved version of the existing SKS spectrometer at KEK. Another J-PARC approved experiment, although not prioritized as 'day-1', is *Measurement of X rays from* Ξ^- *atoms* (K. Tanida, Spokesperson [253]), the physics considerations and the experimental concerns of which are discussed in Sec. VIII B below, following the work of Batty et al. [221].

- A major component of the upgraded GSI facility in Darmstadt, Germany, will be the High Energy Storage Ring (HESR) for high-intensity, phase-space cooled antiprotons between 1.5 and 15 GeV/c. A general purpose detector PANDA (Proton ANtiproton at DArmstadt) will be set up at the HESR. PANDA is scheduled to provide access to high-resolution spectroscopy of $S = -2$ hypernuclei and hyper-atoms by producing abundantly Ξ^- hyperons via the reactions [254]

$$\bar{p} \; + \; p \to \Xi^- \; + \; \bar{\Xi}^+ \,, \qquad \bar{p} \; + \; n \to \Xi^- \; + \; \bar{\Xi}^0 \,, \tag{65}$$

occurring on a nuclear target at $p_{\rm lab} \sim 3$ GeV/c. The trigger for these reactions will be based on the detection of high-momentum $\bar{\Xi}$ antihyperons at small angles or of K^+ mesons produced by the absorption of antihyperons in the primary target nuclei. The Ξ^- hyperons will be slowed down and captured in a secondary nuclear target. One expects in this way to reconstruct approximately 3000 stopped Ξ^- hyperons per day in PANDA. A recent simulation is found in Ref. [255].

B. Ξ^- atoms

Conventional measurements of particle energies to investigate Ξ^- hypernuclei suffer from insufficient accuracy for providing detailed quantitative information on the interaction of Ξ^- hyperons with nuclei. Complementarily, the usual precision for measuring the energies of X-rays from transitions between levels of exotic atoms offers the possibility of obtaining further information. The successful observation and reasonably precise measurement of strong interaction effects in Σ^- atoms, which had provided significant clues to the interaction of Σ^- hyperons with nuclei, may serve as a guide in assessing the feasibility of experiments on exotic atoms of Ξ^-. Recall that the Ξ^- and the Σ^- hyperons have very similar masses and lifetimes, namely 1321.32 vs. 1197.34 MeV, and 0.1642 vs. 0.1482 nsec, for Ξ^- and Σ^- respectively. Full atomic cascade calculations were performed for Σ^- and Ξ^- atoms [221] and confirmed that the processes within these two hadronic atoms are very similar. The remaining major differences are in the production reactions. Whereas relatively slow Σ^- hyperons are produced by the $p(K^-, \pi^+)\Sigma^-$ stopped K^- reaction, the $p(K^-, K^+)\Xi^-$ in-flight reaction produces relatively fast Ξ^- hyperons, thus causing non-negligible decay losses during the slowing down time of the Ξ^- hyperon. Prior to such an experiment it is necessary to optimize the experimental setup, which includes a hydrogen production target, a heavy moderator such as Pb or W, the target to be studied and the detectors, both for X-rays and for the detection of the outgoing K^+, which is essential in order to reduce background.

When selecting targets for possible experiments on Ξ^- atoms, it must be assumed that such experiments will probably not be feasible on more than very few targets, and one must therefore ask whether it is at all likely that useful information on the interaction of Ξ^- with nuclei will be obtained from the resulting rather limited range of data. It was shown

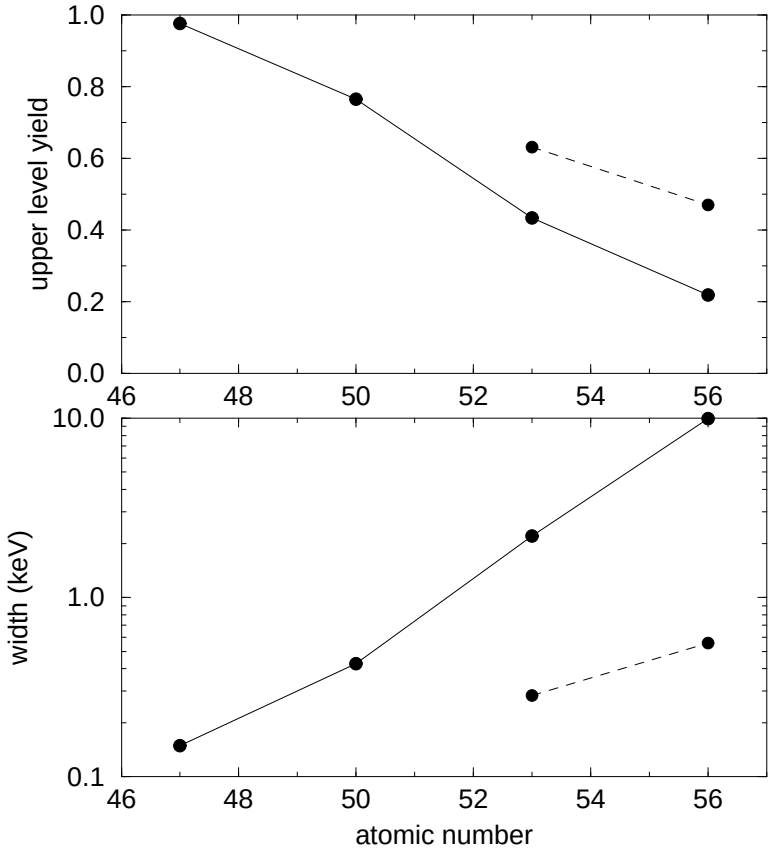

FIG. 42: Solid curves: calculated strong interaction widths and upper level relative yields for the $7i$ level in medium-heavy Ξ^- atoms as function of the atomic number Z. The dashed curves are for $b_0 = -0.25 + \mathrm{i}0.04$ fm, i.e. a repulsive real potential.

[256] that the main features of the interaction of K^- and Σ^- with nuclei, as found from analyses of all the available data, may in fact, be obtained by analyzing a small fraction of the available hadronic atom data, if the target nuclei are carefully selected. A key point here is to have target nuclei over as wide a range of the periodic table as possible. This observation suggests that experiments on Ξ^- atoms may provide useful information.

For estimating strong interaction effects in Ξ^- atoms the $t\rho$ potential Eq. (3) was adopted with $\mathrm{Re}b_0 = 0.25$ fm which yields a potential depth of about 20 MeV inside nuclei, and $\mathrm{Im}b_0 = 0.04$ fm, yielding for the imaginary potential a depth of about 3 MeV. Whereas the real potential may be regarded as 'typical', according to the above discussion, the imaginary potential is about twice as large as estimated [237] in model D. Reducing the imaginary potential will only cause the calculated widths of the states to decrease by roughly the same proportion, and the relative yields (see below) of transitions to become larger. This will not, however, change the last observed atomic level. In choosing criteria for the suitability of a transition as a source of information on the Ξ nucleus interaction, one is guided by experience with other hadronic atoms [1] and select X-ray transitions $(n+1, l+1) \to (n, l)$ between circular atomic states $(n = l + 1)$ with energies greater than 100 keV, where the strong interaction shift for the 'last' (n, l) level is at least 0.5 keV and the width less than about 10 keV. The 'upper' level relative yield, defined as the ratio of the intensity of the $(n + 1, l + 1) \to (n, l)$ X-ray transition to the summed intensity of all X-ray transitions

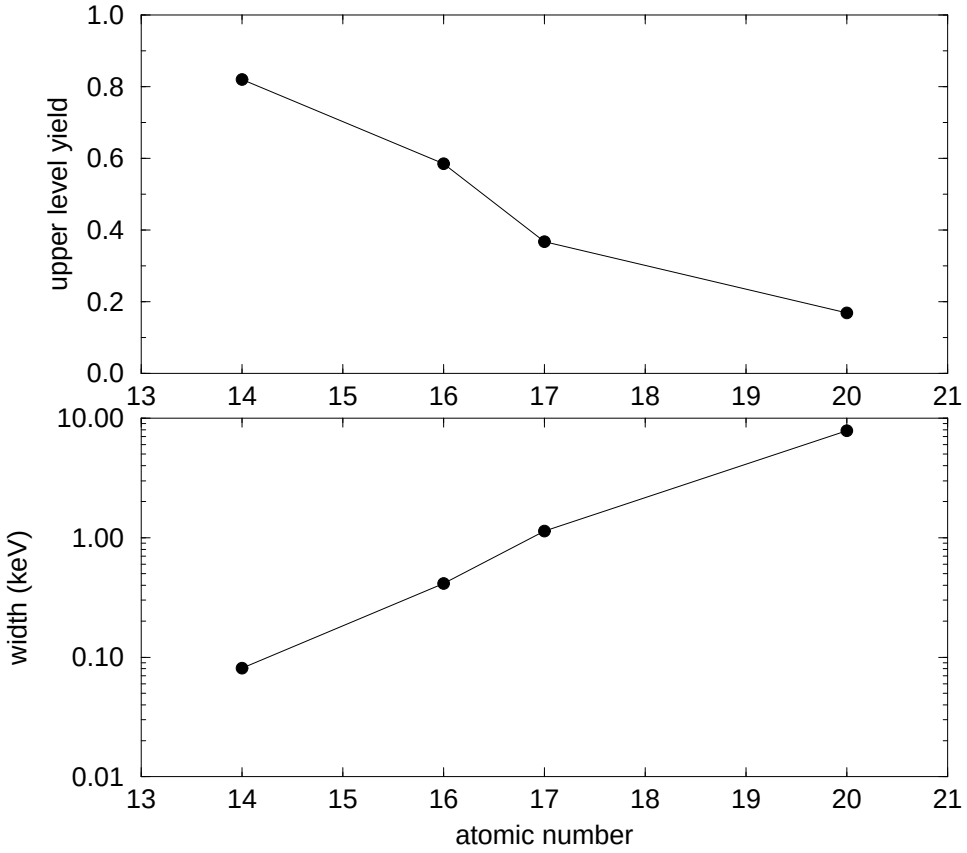

FIG. 43: Calculated strong interaction widths and upper level relative yields for the $4f$ level in Ξ^- atoms.

feeding the $(n+1, l+1)$ state, is also required to be at least 10%.

Strong interaction shifts and widths of Ξ^- atomic levels have been calculated using the above optical potential for a large number of nuclei. As the overlap of atomic wavefunctions with nuclei vary smoothly with charge number, it is to be expected that generally shifts, widths and yields will vary smoothly along the periodic table. Figure 42 shows calculated widths and 'upper' level relative yields for the $7i$ state in medium-heavy Ξ^- atoms and it is seen that a suitable target may be found near Sn or I. The dashed lines in this figure are obtained by reversing the sign of the real potential used for calculating the solid curves. It is seen that in such a case the range of suitable targets will move to between I and Ba, where the strong interaction width and relative yield are more acceptable. The sign of the strong interaction shift will be reversed in this case, but it has no experimental consequences. This exemplifies a general property of hadronic atoms, which are dominated by the Coulomb interaction, namely, that large variations in the strong interaction potential will move the proposed targets only a few units of charge along the periodic table.

Figure 43 shows results for the $4f$ state of Ξ^- atoms, where it is seen that for a Si target the effects could be too small to measure, whereas for Ca the width could be too large and the relative yield too small. In this region a Cl target may be appropriate, perhaps in the form of the liquid CCl_4. More detailed results for Cl are shown in Fig. 44 where the sensitivities to assumptions regarding the optical potential are also typical of results for other targets. The solid curves connect points obtained within the $t\rho$ potential for fixed

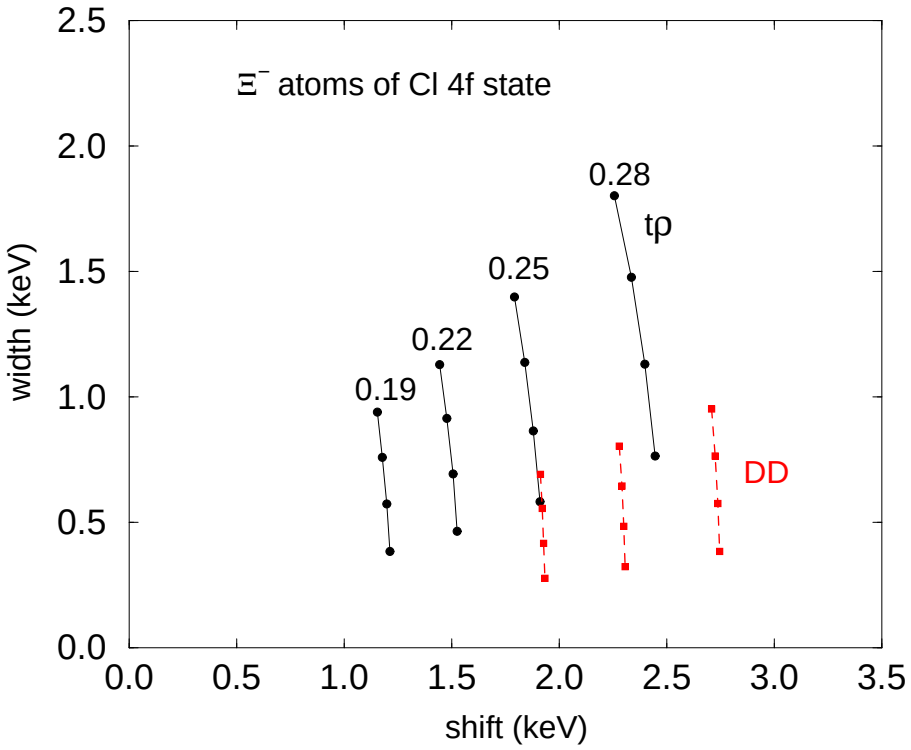

FIG. 44: Calculated strong interaction shifts and widths for the $4f$ level in Ξ^- atoms of Cl for different optical potentials, see text for detail.

TABLE VIII: Predictions for likely targets for a Ξ^- atoms experiment. Calculations are based on a $t\rho$ potential with $b_0 = 0.25 + \mathrm{i}0.04$ fm. E_x is the transition energy, Y is the upper level relative yield.

target	F	Cl	Sn	I	Pb
transition	$4f \rightarrow 3d$	$5g \rightarrow 4f$	$8j \rightarrow 7i$	$8j \rightarrow 7i$	$10l \rightarrow 9k$
E_x (keV)	131.29	223.55	420.25	474.71	558.47
Y	0.31	0.37	0.76	0.43	0.58
shift (keV)	1.56	1.84	0.67	2.79	1.73
width (keV)	0.99	1.14	0.43	2.21	1.26

values of $\mathrm{Re}b_0$, listed above the lines. The four points along each line correspond to values of $\mathrm{Im}b_0$ from 0.05 fm down to 0.02 fm in steps of 0.01 fm. Departures from this $t\rho$ potential are represented by the dashed lines, calculated from phenomenological density dependent (DD) real potentials similar to those found from analyses of experimental results for K^- and Σ^- atoms, as discussed in Secs. IV and VII, respectively. The imaginary part of the potential is of the $t\rho$ type and the points along the dotted lines correspond to the same values of $\mathrm{Im}b_0$ as above. The real potentials in these calculations are similar to the real potential for Σ^- atoms, having an attractive pocket about 5-10 MeV deep outside the nuclear surface, with a repulsive potential of about 20-30 MeV in the nuclear interior. The results in the figure serve only to illustrate the expected range of strong interaction effects. If the actual values of shift and width turn out to be within the area covered by the lines, these effects will most likely be measurable.

Table VIII summarizes results for possible targets for Ξ^- atom experiments [221]. It should be kept in mind that due to the discrete nature of quantum numbers it is not always possible to 'fine-tune' one's choice of a target, considering widths and yields, in spite of their smooth variation with Z. Furthermore, as mentioned above, the main difficulty is likely to be associated with the efficient slowing down of Ξ^- hyperons.

Acknowledgments

We would like to acknowledge and thank our long-time collaborators Chris Batty and Jiří Mareš for making significant contributions to the present Review, and Wolfram Weise for stimulating discussions and valuable criticism in recent years. We are pleased to acknowledge the helpful advice and useful communications obtained on various related topics from Tullio Bressani, Bob Chrien, Toru Harada and Paul Kienle. Special thanks go to Elisabeth Friedman for her dedicated proofreading of the manuscript. This work was supported in part by the Israel Science Foundation, Jerusalem, grant 757/05.

---

[1] C.J. Batty, E. Friedman, A. Gal, Phys. Rep. **287** (1997) 385.
[2] G.E. Brown, M. Rho, Phys. Rep. **363** (2002) 85.
[3] P. Kienle, T. Yamazaki, Prog. Part. Nucl. Phys. **52** (2004) 85.
[4] M.F.M. Lutz, Prog. Part. Nucl. Phys. **53** (2004) 125.
[5] V. Metag, Prog. Part. Nucl. Phys. **55** (2005) 35.
[6] C. Fuchs, Prog. Part. Nucl. Phys. **56** (2006) 1.
[7] K. Saito, K. Tsushima, A.W. Thomas, Prog. Part. Nucl. Phys. **58** (2007) 1.
[8] T.E.O. Ericson, W. Weise, *Pions and Nuclei*, Clarendon Press, Oxford (1988).
[9] R. Schmidt, F.J. Hartmann, T. von Egidy, T. Czosnyka, J. Iwanicki, J. Jastrzębski, M. Kisieliński, P. Lubiński, P. Napiorkowski, L. Pieńkowski, A. Trzcińska, J. Kulpa, R. Smolańczuk, S. Wycech, B. Kłos, K. Gulda, W. Kurcewicz, E. Widmann, Phys. Rev. C **58** (1998) 3195.
[10] G. Fricke, C. Bernhardt, K. Heilig, L.A. Schaller, L. Schellenberg, E.B. Shera, C.W. De Jager, Atom. Data Nucl. Data Tables **60** (1995) 177.
[11] C.J. Batty, E. Friedman, H.J. Gils, H. Rebel, Adv. Nucl. Phys. **19** (1989) 1.
[12] C. García-Recio, J. Nieves, E. Oset, Nucl. Phys. A **547** (1992) 473.
[13] V.E. Starodubsky, N.M. Hintz, Phys. Rev. C **49** (1994) 2118.
[14] A. Krasznahorkay, M. Fujiwara, P. van Aarle, H. Akimune, I. Daito, H. Fujimura, Y. Fujita, M.N. Harakeh, T. Inomata, J. Jänecke, S. Nakayama, A. Tamii, M. Tanaka, H. Toyokawa, W. Uijen, M. Yosoi, Phys. Rev. Lett. **82** (1999) 3216.
[15] B.C. Clark, L.J. Kerr, S. Hamma, Phys. Rev. C **67** (2003) 054605.
[16] J. Jastrzębski, A. Trzcińska, P. Lubiński, B. Kłos, F.J. Hartmann, T. von Egidy, S. Wycech, Int. J. Mod. Phys. E **13** (2004) 343.
[17] E. Friedman, A. Gal, Nucl. Phys. A **724** (2003) 143.
[18] A. Trzcińska, J. Jastrzębski, P. Lubiński, F.J. Hartmann, R. Schmidt, T. von Egidy, B. Kłos, Phys. Rev. Lett. **87** (2001) 082501.
[19] E. Friedman, A. Gal, J. Mareš, Nucl. Phys. A **761** (2005) 283.
[20] G.A. Lalazissis, S. Raman, P. Ring, Atom. Data Nucl. Data Tables **71** (1999) 1.

[21] T. Nikšić, D. Vretenar, P. Finelli, P. Ring, Phys. Rev. C **66** (2002) 024306.
[22] G.A. Lalazissis, T. Nikšić, D. Vretenar, P. Ring, Phys. Rev. C **71** (2005) 024312.
[23] R.H. Dalitz, A. Deloff, J. Phys. G **17** (1991) 289.
[24] A. Cieplý, E. Friedman, A. Gal, J. Mareš, Nucl. Phys. A **696** (2001) 173.
[25] V. Koch, Phys. Lett. B **337** (1994) 7.
[26] T. Waas, N. Kaiser, W. Weise, Phys. Lett. B **365** (1996) 12.
[27] M.F.M. Lutz, Phys. Lett. B **426** (1998) 12.
[28] D. Gotta, Prog. Part. Nucl. Phys. **52** (2004) 133.
[29] L.M. Simons, Int. J. Mod. Phys. A **20** (2005) 1644.
[30] T. Yamazaki, R.S. Hayano, K. Itahashi, K. Oyama, A. Gillitzer, H. Gilg, M. Knülle, M. Münch, P. Kienle, W. Schott, H. Geissel, N. Iwasa, G. Münzenberg, Z. Phys. A **355** (1996) 219.
[31] K. Suzuki, M. Fujita, H. Geissel, H. Gilg, A. Gillitzer, R.S. Hayano, S. Hirenzaki, K. Itahashi, M. Iwasaki, P. Kienle, M. Matos, G. Münzenberg, T. Ohtsubo, M. Sato, M. Shindo, T. Suzuki, H. Weick, M. Winkler, T. Yamazaki, T. Yoneyama, Phys. Rev. Lett. **92** (2004) 072302.
[32] E. Friedman, M. Bauer, J. Breitschopf, H. Clement, H. Denz, E. Doroshkevich, A. Erhardt, G.J. Hofman, R. Meier, G.J. Wagner, G. Yaari, Phys. Rev. Lett. **93** (2004) 122302.
[33] E. Friedman, M. Bauer, J. Breitschopf, H. Clement, H. Denz, E. Doroshkevich, A. Erhardt, G.J. Hofman, S. Kritchman, R. Meier, G.J. Wagner, G. Yaari, Phys. Rev. C **72** (2005) 034609.
[34] M. Iwasaki, R.S. Hayano, T.M. Ito, S.N. Nakamura, T.P. Terada, D.R. Gill, L. Lee, A. Olin, M. Salomon, S. Yen, K. Bartlett, G.A. Beer, G. Mason, G. Trayling, H. Outa, T. Taniguchi, Y. Tamashita, R. Seki, Phys. Rev. Lett. **78** (1997) 3067.
[35] G. Beer, A.M. Bragadireanu, M. Cargnelli, C. Curceanu-Petrascu, J.-P. Egger, H. Fuhrmann, C. Guaraldo, M. Iliescu, T. Ishiwatari, K. Itahashi, M. Iwasaki, P. Kienle, T. Koike, B. Lauss, V. Lucherini, L. Ludhova, J. Marton, F. Mulhauser, T. Ponta, L.A. Schaller, R. Seki, D.L. Sirghi, F. Sirghi, J. Zmeskal, Phys. Rev. Lett. **94** (2005) 212302.
[36] S. Okada, G. Beer, H. Bhang, M. Cargnelli, J. Chiba, S. Choi, C. Curceanu, Y. Fukuda, T. Hanaki, R.S. Hayano, M. Lio, T. Ishikawa, S. Ishimoto, T. Ishiwatari, K. Itahashi, M. Iwai, M. Iwasaki, B. Juhász, P. Kienle, J. Marton, Y. Matsuda, H. Ohnishi, H. Outa, M. Sato, P. Schmid, S. Suzuki, T. Suzuki, H. Tatsuno, D. Tomono, E. Widmann, T. Yamazaki, H. Yim, J. Zmeskal, arXiv:0707.0448 [nucl-ex], submitted to Phys. Lett. B.
[37] T. Suzuki, H. Bhang, G. Franklin, K. Gomikawa, R.S. Hayano, T. Hayashi, K. Ishikawa, S. Ishimoto, K. Itahashi, M. Iwasaki, T. Katayama, Y. Kondo, Y. Matsuda, T. Nakamura, S. Okada, H. Outa, B. Quinn, M. Sato, M. Shindo, H. So, P. Strasser, T. Sugimoto, K. Suzuki, S. Suzuki, D. Tomono, A.M. Vinodkumar, E. Widmann, T. Yamazaki, T. Yoneyama, Phys. Lett. B **597** (2004) 263.
[38] T. Suzuki, H. Bhang, G. Franklin, K. Gomikawa, R.S. Hayano, T. Hayashi, K. Ishikawa, S. Ishimoto, K. Itahashi, M. Iwasaki, T. Katayama, Y. Kondo, Y. Matsuda, T. Nakamura, S. Okada, H. Outa, B. Quinn, M. Sato, M. Shindo, H. So, P. Strasser, T. Sugimoto, K. Suzuki, S. Suzuki, D. Tomono, A.M. Vinodkumar, E. Widmann, T. Yamazaki, T. Yoneyama, Nucl. Phys. A **754** (2005) 375c.
[39] T. Kishimoto, T. Hayakawa, S. Ajimura, S. Minami, A. Sakaguchi, Y. Shimizu, R.E. Chrien, M. May, P. Pile, A. Rusek, R. Sutter, H. Noumi, H. Tamura, M. Ukai, Y. Miura, K. Tanida, Nucl. Phys. A **754** (2005) 383c.
[40] M. Agnello, G. Beer, L. Benussi, M. Bertani, S. Bianco, E. Botta, T. Bressani, L. Busso,

D. Calvo, P. Camerini, P. Cerello, B. Dalena, F. De Mori, G. D'Erasmo, D. Di Santo, F.L. Fabbri, D. Faso, A. Feliciello, A. Filippi, V. Filippini, E.M. Fiore, H. Fujioka, P. Gianotti, N. Grion, V. Lucherini, S. Marcello, T. Maruta, N. Mirfakhrai, O. Morra, T. Nagae, A. Olin, H. Outa, E. Pace, M. Palomba, A. Pantaleo, A. Panzarasa, V. Paticchio, S. Piano, F. Pompili, R. Rui, G. Simonetti, H. So, S. Tomassini, A. Toyoda, R. Wheadon, A. Zenoni, Phys. Rev. Lett. **94** (2005) 212303.

[41] E. Friedman, A. Gal, R. Weiss, J. Aclander, J. Alster, I. Mardor, Y. Mardor, S. May-Tal Beck, E. Piasetzky, A.I. Yavin, S. Bart, R.E. Chrien, P.H. Pile, R. Sawafta, R.J. Sutter, M. Barakat, K. Johnston, R.A. Krauss, H. Seyfarth, R.L. Stearns, Phys. Rev. C **55** (1997) 1304.

[42] E. Friedman, A. Gal, J. Mareš, Phys. Lett. B **396** (1997) 21.

[43] E. Friedman, A. Gal, J. Mareš, Nucl. Phys. A **625** (1997) 272.

[44] A. Zenoni, A. Bianconi, G. Bonomi, M. Corradini, A. Donzella, E. Lodi Rizzini, L. Venturelli, A. Bertin, M. Bruschi, M. Capponi, S. De Castro, R. Don, D. Galli, B. Giacobbe, U. Marconi, I. Massa, M. Piccinini, N. Semprini Cesari, R. Spighi, V. Vagnoni, S. Vecchi, M. Villa, A. Vitale, A. Zoccoli, M. Poli, C. Cical, A. Masoni, S. Mauro, G. Puddu, S. Serci, G. Usai, O.E. Gorchakov, S.N. Prakhov, A.M. Rozhdestvensky, V.I. Tretyak, P. Gianotti, C. Guaraldo, A. Lanaro, V. Lucherini, C. Petrascu, U. Gastaldi, L. Vannucci, R.A. Ricci, G. Bendiscioli, A. Fontana, P. Montagna, A. Rotondi, P. Salvini, N. Mirfakhrai, F. Balestra, M.P. Bussa, L. Busso, P. Cerello, O.Y. Denisov, L. Ferrero, R. Garfagnini, A. Grasso, A. Panzarasa, D. Panzieri, F. Tosello, E. Botta, T. Bressani, D. Calvo, S. Costa, F. D'Isep, A. Feliciello, A. Filippi, S. Marcello, M. Agnello, F. Iazzi, B. Minetti, S. Tessaro, Phys. Lett. B **461** (1999) 413.

[45] A. Bianconi, G. Bonomi, M.P. Bussa, E. Lodi Rizzini, L. Venturelli, A. Zenoni, G.B. Pontecorvo, C. Guaraldo, F. Balestra, L. Busso, M.L. Colantoni, A. Ferrero, L. Ferrero, A. Grasso, A. Maggiora, M. Maggiora, G. Piragino, F. Tosello, Phys. Lett. B **481** (2000) 194.

[46] A. Zenoni, A. Bianconi, F. Bocci, G. Bonomi, M. Corradini, A. Donzella, E. Lodi Rizzini, L. Venturelli, A. Bertin, M. Bruschi, M. Capponi, S. De Castro, R. Don, D. Galli, B. Giacobbe, U. Marconi, I. Massa, M. Piccinini, N. Semprini Cesari, R. Spighi, V. Vagnoni, S. Vecchi, M. Villa, A. Vitale, A. Zoccoli, C. Cical, A. Masoni, S. Mauro, G. Puddu, S. Serci, G. Usai, O.E. Gorchakov, S.N. Prakhov, A.M. Rozhdestvensky, V.I. Tretyak, M. Poli, P. Gianotti, C. Guaraldo, A. Lanaro, V. Lucherini, C. Petrascu, V.G. Ableev, U. Gastaldi, L. Vannucci, G. Bendiscioli, A. Fontana, P. Montagna, A. Rotondi, P. Salvini, N. Mirfakhrai, F. Balestra, E. Botta, T. Bressani, M.P. Bussa, L. Busso, D. Calvo, P. Cerello, S. Costa, O.Y. Denisov, F. D'Isep, A. Feliciello, L. Ferrero, A. Filippi, R. Garfagnini, A. Grasso, A. Maggiora, S. Marcello, A. Panzarasa, F. Tosello, M. Agnello, F. Iazzi, B. Minetti, S. Tessaro, Phys. Lett. B **461** (1999) 405.

[47] F. Iazzi, A. Feliciello, M. Agnello, M. Astrua, E. Botta, T. Bressani, D. Calvo, S. Costa, F. D'Isep, A. Filippi, S. Marcello, B. Minetti, N. Mirfakhraee, F. Balestra, M.P. Bussa, L. Busso, P. Cerello, O. Denisov, L. Ferrero, R. Garfagnini, A. Maggiora, A. Panzarasa, D. Panzieri, F. Tosello, A. Bertin, M. Bruschi, M. Capponi, S. De Castro, R. Dona, D. Galli, B. Giacobbe, U. Marconi, I. Massa, M. Piccinini, M. Poli, N. Semprini Cesari, R. Spighi, V. Vagnoni, S. Vecchi, M. Villa, A. Vitale, A. Zoccoli, A. Bianconi, G. Bonomi, E. Lodi Rizzini, L. Venturelli, A. Zenoni, C. Cicalo, A. Masoni, S. Mauro, G. Puddu, S. Serci, G. Usai, O.E. Gorchakov, S.N. Prakhov, A.M. Rozhdestvensky, V.I. Tretyak, P. Gianotti,

C. Guaraldo, A. Lanaro, V. Lucherini, C. Petrascu, M. Lombardi, R.A. Ricci, L. Vannucci, G. Bendiscioli, A. Fontana, P. Montagna, A. Rotondi, P. Salvini, S. Tessaro, Phys. Lett. B **475** (2000) 378.

[48] A. Trzcińska, J. Jastrzębski, T. Czosnyka, T. von Egidy, K. Gulda, F.J. Hartmann, J. Iwanicki, B. Ketzer, M. Kisieliński, B. Kłos, W. Kurcewicz, P. Lubiński, P.J. Napiorkowski, L. Pieńkowski, R. Schmidt, E. Widmann, Nucl. Phys. A **692** (2001) 176c.

[49] P. Lubiński, J. Jastrzębski, A. Trzcińska, W. Kurcewicz, F.J. Hartmann, R. Schmidt, T. von Egidy, R. Smolańczuk, S. Wycech, Phys. Rev. C **57** (1998) 2962.

[50] R. Schmidt, F.J. Hartmann, B. Ketzer, T. von Egidy, T. Czosnyka, J. Jastrzębski, M. Kisieliński, P. Lubiński, P. Napiorkowski, L. Pieńkowski, A. Trzcińska, B. Kłos, R. Smolańczuk, S. Wycech, W. Pöschl, K. Gulda, W. Kurcewicz, E. Widmann, Phys. Rev. C **60** (1999) 054309.

[51] P.K. Saha, H. Noumi, D. Abe, S. Ajimura, K. Aoki, H.C. Bhang, K. Dobashi, T. Endo, Y. Fujii, T. Fukuda, H.C. Guo, O. Hashimoto, K. Imai, E.H. Kim, J.H. Kim, T. Kishimoto, A. Krutenkova, K. Maeda, T. Nagae, M. Nakamura, H. outa, T. Saito, A. Sakaguchi, Y. Sato, R. Sawafta, M. Sekimoto, Y. Shimizu, T. Takahashi, H. Tamura, L. Tang, K. Tanida, T. Watanabe, H.H. Xia, S.H. Zhou, X.F. Zhu, L.H. Zhu, Phys. Rev. C **70** (2004) 044613.

[52] L.S. Kisslinger, Phys. Rev. **98** (1955) 761.

[53] E. Friedman, Phys. Rev. C **28** (1983) 1264.

[54] M.B. Johnson, G.R. Sachtler, Ann. Phys. [NY] **248** (1996) 134.

[55] M. Ericson, T.E.O. Ericson, Ann. Phys. [NY] **36** (1966) 323.

[56] E. Friedman, A. Gal, Nucl. Phys. A **345** (1980) 457.

[57] K. Stricker, J.A. Carr, H. McManus, Phys. Rev. C **22** (1980) 2043.

[58] L.W. Fullerton, G.A. Rinker, Phys. Rev. A **13** (1976) 1283.

[59] J. Konijn, C.T.A.M. de Laat, A. Taal, J.H. Koch, Nucl. Phys. A **519** (1990) 773.

[60] B.H. Olaniyi, G.A. Beer, A. Fry, J.A. Macdonald, G.R. Mason, A. Olin, R.M. Pearce, P.R. Poffenberger, Nucl. Phys. A **384** (1982) 345.

[61] D.J. Britton, G.A. Beer, J.A. Macdonald, G.R. Mason, T. Numao, A. Olin, P.R. Poffenberger, A.R. Kunselman, B.H. Olaniyi, Nucl. Phys. A **461** (1987) 571.

[62] A. Taal, P. David, H. Hänscheid, J.H. Koch, C.T.A.M. de Laat, W. Lourens, F. Risse, Ch.F.G. Rösel, A. van der Schaaf, W. Schrieder, J. Konijn, Nucl. Phys. A **511** (1990) 573.

[63] H. Geissel, H. Gilg, A. Gillitzer, R.S. Hayano, S. Hirenzaki, K. Itahashi, M. Iwasaki, P. Kienle, M. Münch, G. Münzenberg, W. Schott, K. Suzuki, D. Tomono, H. Weick, T. Yamazaki, T. Yoneyama, Phys. Rev. Lett. **88** (2002) 122301.

[64] G.de Chambrier, W. Beer, F.W.N. de Boer, K. Boss, A.I. Egorov, M. Eckhause, K.L. Giovanetti, P.F.A. Goudsmit, B. Jeckelmann, K.E. Kir'yanov, L.N. Kondurova, L. Lapina, H.J. Leisi, V.I. Masrushenko, A.F. Mezentsev, A.A. Petrunin, A.G. Sergeev, A.I. Smirnov, G. Strassner, V.M. Suvorov, A. Vacchi, D. Wieser, Nucl. Phys. A **442** (1985) 637.

[65] C.J. Batty, S.F. Biagi, S.D. Hoath, J.D. Davies, G.J. Pyle, G.T.A. Squier, D.M. Asbury, A. Guberman, Nucl. Phys. A **322** (1979) 445.

[66] C.J. Batty, S.F. Biagi, E. Friedman, S.D. Hoath, J.D. Davies, G.J. Pyle, G.T.A. Squier, D.M. Asbury, M. Leon, Phys. Lett. **81B** (1979) 165.

[67] R.J. Powers, K.-C. Wang, M.V. Hoehn, E.B. Shera, W.D. Wohlfahrt, A.R. Kunselman, Nucl. Phys. A **336** (1980) 475.

[68] R. Kunselman, R.J. Powers, M.V. Hoehn, E.B. Shera, Nucl. Phys. A **405** (1983) 627.

[69] R. Abela, P. Blüm, R. Guigas, H. Koch, G. Backenstoss, M. Brandao d'Oliveira, M. Izycki,

L. Tauscher, P. Pavlopoulos, K. Zioutas, Zeit. Phys. A **282** (1977) 93.
[70] D.A. Jenkins, R.J. Powers, A.R. Kunselman, Phys. Rev. C **2** (1970) 429.
[71] A.R. Kunselman, P. Roberson, R.J. Powers, F. Boehm, J.P. Miller, A. Zehnder, Phys. Rev. C **15** (1977) 1801.
[72] Y. Tanaka, R.M. Steffen, E.B. Shera. W. Reuter, M.V. Hoehn, J.D. Zumbro, Phys. Lett. **143B** (1984) 347.
[73] C.T.A.M. de Laat, P. David, H. Hänscheid, J. Konijn, C. Petitjean, F. Risse, Ch.F.G. Rösel, W. Schrieder, A. Taal, Nucl. Phys. A **523** (1991) 453.
[74] C.J. Batty, S.F. Biagi, R.A.J. Riddle, B.L. Roberts, G.J. Pyle, G.T.A. Squier, D.M. Asbury, A.S. Clough, Nucl. Phys. A **355** (1981) 383.
[75] E. Friedman, G. Soff, J. Phys. G: Nucl. Phys. **11** (1985) L37.
[76] C.J. Batty, E. Friedman, A. Gal, Nucl. Phys. A **402** (1983) 411.
[77] H. Toki, T. Yamazaki, Phys. Lett. B **213** (1988) 129.
[78] T.E.O. Ericson, K. Kilian, PANIC 1984 abstract N9.
[79] R. Seki, K. Masutani, Phys. Rev. C **27** (1983) 2799.
[80] E. Friedman, Int. J. Mod. Phys. A **22** (2007) 213.
[81] E. Friedman, A. Gal, Phys. Lett. B **432** (1998) 235.
[82] J. Chai, D.O. Riska, Nucl. Phys. A **329** (1979) 429.
[83] L.L. Salcedo, K. Holinde, E. Oset, C. Schütz, Phys. Lett. B **353** (1995) 1.
[84] J. Marton, Nucl. Phys. A **790** (2007) 328c.
[85] W. Weise, Acta Phys. Pol. B **31** (2000) 2715.
[86] W. Weise, Nucl. Phys. A **690** (2001) 98c.
[87] Y. Tomozawa, Nuovo Cimento A **46** (1966) 707.
[88] S. Weinberg, Phys. Rev. Lett. **17** (1966) 616.
[89] E.G. Drukarev, E.M. Levin, Prog. Part. Nucl. Phys. **27** (1991) 77.
[90] V. Thorsson, A. Wirzba, Nucl. Phys. A **589** (1995) 633.
[91] U.-G. Meissner, J.A. Oller, A. Wirzba, Ann. Phys. [NY] **297** (2002) 27.
[92] J. Gasser, H. Leutwyler, M.E. Sainio, Phys. Lett. B **253** (1991) 252).
[93] P. Kienle, T. Yamazaki, Phys. Lett. B **514** (2001) 1.
[94] E. Friedman, Phys. Lett. B **524** (2002) 87.
[95] E.E. Kolomeitsev, N. Kaiser, W. Weise, Phys. Rev. Lett. **90** (2003) 092501.
[96] E.E. Kolomeitsev, N. Kaiser, W. Weise, Nucl. Phys. A **721** (2003) 835c.
[97] T.E.O. Ericson, L. Tauscher, Phys. Lett. B **112** (1982) 425.
[98] E. Friedman, A. Gal, Phys. Lett. B **578** (2004) 85.
[99] T.E.O. Ericson, Phys. Lett. B **321** (1994) 312.
[100] D. Agassi, A. Gal, Ann. Phys. [NY] **75** (1973) 56.
[101] N. Barnea, E. Friedman, Phys. Rev. C **75** (2007) 022202(R).
[102] A simple and convenient introduction to the concept of functional derivative can be found in the wikipedia web site: *http://en.wikipedia.org/wiki/Functional_derivative.*
[103] K. Stricker, H. McManus, J.A. Carr, Phys. Rev. C **19** (1979) 929.
[104] D.H. Wright, M. Blecher, B.G. Ritchie, D. Rothenberger, R.L. Burman, Z. Weinfeld, J.A. Escalante, C.S. Mishra, C.S. Whisnant, Phys. Rev. C **37** (1988) 1155.
[105] E. Friedman, A. Gal, C.J. Batty, Phys. Lett. B **308** (1993) 6.
[106] E. Friedman, A. Gal, C.J. Batty, Nucl. Phys. A **579** (1994) 518.
[107] E. Friedman, A. Gal, J. Mareš, A. Cieplý, Phys. Rev. C **60** (1999) 024314.
[108] J. Mareš, E. Friedman, A. Gal, Nucl. Phys. A **770** (2006) 84.

[109] J. Schaffner-Bielich, V. Koch, M. Effenberger, Nucl. Phys. A **669** (2000) 153.
[110] A. Ramos, E. Oset, Nucl. Phys. A **671** (2000) 481.
[111] L.Tolos, A.Ramos, A.Polls, T.T.S.Kuo, Nucl. Phys. A **690** (2001) 547.
[112] L. Tolós, A. Ramos, E. Oset, Phys. Rev. C **74** (2006) 015203.
[113] N. Kaiser, P.B. Siegel, W. Weise, Nucl. Phys. A **594** (1995) 325.
[114] E. Oset, A. Ramos, Nucl. Phys. A **635** (1998) 99.
[115] D.N. Tovee, D.H. Davis, J. Simonović, G. Bohm, J. Klabuhn, F. Wysotzki, M. Csejthey-Barth, J.H. Wickens, T. Cantwell, C. Ni Ghógáin, A. Montwill, K. Garbowska-Pniewska, T. Pniewski, J. Zakrzewski, Nucl. Phys. B **33** (1971) 493.
[116] R.J. Nowak, J. Armstrong, D.H. Davis, D.J. Miller, D.N. Tovee, D. Bertrand, M. Goossens, G. Vanhomwegen, G. Wilquet, M. Abdullah, N.H. Bedford, J. Ciborowski, J.V. Major, J.A. Zakrzewski, D. Kielczewska, T. Tymieniecka, E. Rondio, Nucl. Phys. B **139** (1978) 61.
[117] U.-G. Meißner, U. Raha, A. Rusetsky, Eur. Phys. J. C **35**, 349 (2004).
[118] B. Borasoy, R. Nißler, W. Weise, Phys. Rev. Lett. **94** (2005) 213401.
[119] B. Borasoy, R. Nißler, W. Weise, Eur. Phys. J. A **25** (2005) 79.
[120] B. Borasoy, R. Nißler, W. Weise, Phys. Rev. Lett. **96** (2006) 199201.
[121] B. Borasoy, U.-G. Meißner, R. Nißler, Phys. Rev. C **74** (2006) 055201.
[122] J.A. Oller, J. Prades, M. Verbeni, Eur. Phys. J. A **31** (2007) 527.
[123] R.H. Dalitz, S.F. Tuan, Phys. Rev. Lett. **2** (1959) 425.
[124] W. Weise, plenary talk at HYP06, Mainz, October 2006, arXiv:nucl-th/0701035.
[125] T. Waas, M. Rho, W. Weise, Nucl. Phys. A **617** (1997) 449, and references therein.
[126] E.G. Drukarev, private communication, May 2006.
[127] J. Schaffner, A. Gal, I.N. Mishustin, H. Stöcker, W. Greiner, Phys. Lett. B **334** (1994) 268.
[128] G.E. Brown, M. Rho, Nucl. Phys. A **596** (1996) 503.
[129] W. Scheinast, I. Bottcher, M. Debowski, F. Dohrmann, A. Forster, E. Grosse, P. Koczon, B. Kohlmeyer, F. Laue, M. Menzel, L. Naumann, E. Schwab, P. Senger, Y. Shin, H. Strobele, C. Sturm, G. Surowka, F. Uhlig, A. Wagner, W. Walus, B. Kampfer, H.W. Barz, Phys. Rev. Lett. **96** (2006) 072301, and references therein.
[130] H. Tamura, R.S. Hayano, H. Outa, T. Yamazaki, Prog. Theor. Phys. Suppl. **117** (1994) 1.
[131] M.W. Ahmed, X. Cui, A. Empl, E.V. Hungerford, K.J. Lan, M. Youn, R.E. Chrien, R. Gill, P. Pile, A. Rusek, R. Sutter, J. Bjoraker, D. Dehnhard, J.M. O'Donnell, J. Gerald, H. Juengst, J.H. Liu, J.C. Peng, C.L. Morris, C.M. Riedel, H.A. Thiessen, D. Androic, I. Bertovic, M. Furic, T. Petkovic, M. Planinic, L. Tang, V. Zeps, Phys. Rev. C **68** (2003) 064004.
[132] A. Baca, C. García-Recio, J. Nieves, Nucl. Phys. A **673** (2000) 335.
[133] E. Friedman, A. Gal, Phys. Lett. B **459** (1999) 43.
[134] E. Friedman, A. Gal, Nucl. Phys. A **658** (1999) 345.
[135] Y. Nogami, Phys. Lett. **7** (1963) 288.
[136] T. Yamazaki, Y. Akaishi, Phys. Lett. B **535** (2002) 70.
[137] A. Doté, W. Weise, presented at HYP06, Mainz, October 2006, arXiv:nucl-th/0701050.
[138] N.V. Shevchenko, A. Gal, J. Mareš, Phys. Rev. Lett. **98** (2007) 082301.
[139] N.V. Shevchenko, A. Gal, J. Mareš, J. Révai, submitted to Phys. Rev. C, arXiv:0706.4393 [nucl-th].
[140] Y. Ikeda, T. Sato, presented at HYP06, Mainz, October 2006, arXiv:nucl-th/0701001.
[141] Y. Ikeda, T. Sato, submitted to Phys. Rev. C, arXiv:0704.1978 [nucl-th].
[142] T. Koike, T. Harada, submitted to Phys. Lett. B, arXiv:nucl-th/0703037.
[143] T. Kishimoto, Phys. Rev. Lett. **83** (1999) 4701.

[144] Y. Akaishi, T. Yamazaki, in: S. Bianconi, et al. (Eds.), Proc. III Int. DAΦNE Workshop, Frascati Physics Series vol. XVI, LNF, Frascati, 1999, pp. 59-74.
[145] Y. Akaishi, T. Yamazaki, Phys. Rev. C **65** (2002) 044005.
[146] S. Wycech, Nucl. Phys. A **450** (1986) 399c.
[147] M. Iwasaki, H. Bhang, J. Chiba, S. Choi, Y. Fukuda, T. Hanaki, R.S. Hayano, M. Lio, T. Ishikawa, S. Ishimoto, T. Ishiwatari, K. Itahashi, M. Iwai, P. Kienle, J.H. Kim, Y. Matsuda, H. Ohnishi, S. Okada, H. Outa, M. Sato, S. Suzuki, T. Suzuki, D. Tomono, E. Widmann, T. Yamazaki, H. Yim, arXiv:0706.0297 [nucl-ex], plenary talk given by M. Iwasaki at HYP06, Mainz, October 2006.
[148] T. Kishimoto et al., KEK E548 collaboration, Prog. Theor. Phys. **118** (2007) 181.
[149] V.K. Magas, E. Oset, A. Ramos, H. Toki, Phys. Rev. C **74** (2006) 025206.
[150] M. Agnello, G. Beer, L. Benussi, M. Bertani, H.C. Bhang, S. Bianco, G. Bonomi, E. Botta, M. Bregant, T. Bressani, S. Bufalino, L. Busso, D. Calvo, P. Camerini, P. Cerello, B. Dalena, F. De Mori, G. D'Erasmo, D. Di Santo, D. Elia, F.L. Fabbri, D. Faso, A. Feliciello, A. Filippi, V. Filippini, R.A. Fini, E.M. Fiore, H. Fujioka, P. Gianotti, N. Grion, O. Hartmann, A. Krasnoperov, V. Lenti, V. Lucherini, V. Manzari, S. Marcello, T. Maruta, N. Mirfakhrai, O. Morra, T. Nagae, A. Olin, H. Outa, E. Pace, M. Pallota, M. Palomba, A. Pantaleo, A. Panzarasa, V. Paticchio, S. Piano, F. Pompili, R. Rui, G. Simonetti, H. So, V. Tereshchenko, S. Tomassini, A. Toyoda, R. Wheadon, A. Zenoni, Nucl. Phys. A **775** (2006) 35.
[151] G. Bendiscioli, T. Bressani, A. Fontana, L. Lavezzi, A. Panzarasa, A. Rotondi, Nucl. Phys. A **789** (2007) 222, presented by T. Bressani at HYP06, Mainz, October 2006.
[152] T. Nagae, plenary talk at HYP06, Mainz, October 2006.
[153] M. Agnello, G. Beer, L. Benussi, M. Bertani, H.C. Bhang, S. Bianco, G. Bonomi, E. Botta, M. Bregant, T. Bressani, S. Bufalino, L. Busso, D. Calvo, P. Camerini, M. Caponero, P. Cerello, B. Dalena, F. De Mori, G. D'Erasmo, D. Di Santo, R. Dona, D. Elia, F.L. Fabbri, D. Faso, A. Feliciello, A. Filippi, V. Filippini, R.A. Fini, E.M. Fiore, H. Fujioka, P. Gianotti, N. Grion, A. Krasnoperov, V. Lucherini, V. Lenti, V. Manzari, S. Marcello, T. Maruta, N. Mirfakhrai, O. Morra, T. Nagae, A. Olin, H. Outa, E. Pace, M. Pallota, M. Palomba, A. Pantaleo, A. Panzarasa, V. Paticchio, S. Piano, F. Pompili, R. Rui, G. Simonetti, H. So, V. Tereshchenko, S. Tomassini, A. Toyoda, R. Wheadon, A. Zenoni, presented by S. Piano at HYP06, Mainz, October 2006.
[154] J. Mareš, E. Friedman, A. Gal, Phys. Lett. B **606** (2005) 295.
[155] D. Gazda, E. Friedman, A. Gal, J. Mareš, submitted to Phys. Rev. C.
[156] C.B. Dover, G.E. Walker, Phys. Rep. **89** (1982) 1.
[157] D.V. Bugg, R.S. Gilmore, K.M. Knight, D.C. Salter, G.H. Stafford, E.J.N. Wilson, J.D. Davies, J.D. Dowell, P.M. Hattersley, R.J. Homer, A.W. O'dell, A.A. Carter, R.J. Tapper, K.F. Riley, Phys. Rev. **168** (1968) 1466.
[158] D. Marlow, P.D. Barnes, N.J. Colella, S.A. Dytman, R.A. Eisenstein, R. Grace, F. Takeutchi, W.R. Wharton, S. Bart, D. Hancock, R. Hackenberg, E. Hungerford, W. Mayes, L. Pinsky, T. Williams, R. Chrien, H. Palevsky, R. Sutter, Phys. Rev. C **25** (1982) 2619.
[159] P.B. Siegel, W.B. Kaufmann, W.R. Gibbs, Phys. Rev. C **31** (1985) 2184.
[160] R.J. Peterson, Phys. Rev. C **60** (1999) 022201.
[161] G.E. Brown, C.B. Dover, P.B. Siegel, W. Weise, Phys. Rev. Lett. **60** (1988) 2723.
[162] J.C. Caillon, J. Labarsouque, Phys. Rev. C **53** (1996) 1993, and references cited therein to earlier works.
[163] M.F. Jiang, D.S. Koltun, Phys. Rev. C **46** (1992) 2462.

[164] C. García-Recio, J. Nieves, E. Oset, Phys. Rev. C **51** (1995) 237.
[165] R.A. Krauss, J. Alster, D. Ashery, S. Bart, R.E. Chrien, J.C. Hiebert, R.R. Johnson, T. Kishimoto, I. Mardor, Y. Mardor, M.A. Moinester, R. Olshevsky, E. Piasetzky, P.H. Pile, R. Sawafta, R.L. Stearns, R.J. Sutter, R. Weiss, A.I. Yavin, Phys. Rev. C **46** (1992) 655.
[166] R. Sawafta, R. Weiss, J. Aclander, J. Alster, M. Barakat, S. Bart, R.E. Chrien, R.A. Krauss, K. Johnston, I. Mardor, Y. Mardor, S. MayTal-Beck, E. Piasetzky, P.H. Pile, H. Seyfarth, R.L. Stearns, R.J. Sutter, I.A. Yavin, Phys. Lett. B **307** (1993) 293.
[167] R. Weiss, J. Aclander, J. Alster, M. Barakat, S. Bart, R.E. Chrien, R.A. Krauss, K. Johnston, I. Mardor, Y. Mardor, S. May Tal-beck, E. Piasetzky, P.H. Pile, R. Sawafta, H. Seyfarth, R.L. Stearns, R.J. Sutter, A.I. Yavin, Phys. Rev. C **49** (1994) 2569.
[168] C.M. Kormanyos, R.J. Peterson, J.R. Shepard, J.E. Wise, S. Bart, R.E. Chrien, L. Lee, B.L. Clausen, J. Piekarewicz, M.B. Barakat, E.V. Hungerford, R.A. Michael, K.H. Hicks, T. Kishimoto, Phys. Rev. C **51** (1995) 669.
[169] R. Michael, M.B. Barakat, S. Bart, R.E. Chrien, B.C. Clark, D.J. Ernst, S. Hama, K.H. Hicks, Wendy Hinton, E.V. Hungerford, M.F. Jiang, T. Kishimoto, C.M. Kormanyos, L.J. Kurth, L. Lee, B. Mayes, R.J. Peterson, L. Pinsky, R. Sawafta, R. Sutter, L. Tang, J.E. Wise, Phys. Lett. B **382** (1996) 29.
[170] R.E. Chrien, R. Sawafta, R.J. Peterson, R.A. Michael, E.V. Hungerford, Nucl. Phys. A **625** (1997) 251.
[171] A. Gal, E. Friedman, Phys. Rev. Lett. **94** (2005) 072301.
[172] A. Gal, E. Friedman, Phys. Rev. C **73** (2006) 015208.
[173] L. Tolós, D. Cabrera, A. Ramos, A. Polls, Phys. Lett. B **632** (2006) 219.
[174] H.F. Arellano, H.V. von Geramb, Phys. Rev. C **72** (2005) 025203.
[175] R.A. Arndt, W.J. Briscoe, R.L. Workman, I.I. Strakovsky, CNS DAC [SAID], Phys, Dept. GWU, http://gwdac.phys.gwu.edu.
[176] R.J. Peterson, Nucl. Phys. A **740** (2004) 119.
[177] R.A. Schumacher, in Particles and Nuclei, Proc. PANIC05, AIP Conf. Proc **842** (2006) 409.
[178] F.J. Llanes-Estrada, E. Oset, V. Mateu, Phys. Rev. C **69** (2004) 055203.
[179] D. Ashery, J.P. Schiffer, Annu. Rev. Nucl. Part. Sci. **36** (1986) 207.
[180] A.S. Goldhaber, *Proceedings of the Second LAMPF II Workshop*, edited by H.A. Thiessen, T.S. Bhatia, R.D. Carlini, and N. Hintz, LA-9572-C, Vol. I (1982) 171.
[181] C.J. Batty, E. Friedman, A. Gal, Nucl. Phys. A **592** (1995) 487.
[182] J. Côté, M. Lacombe, B. Loiseau, B. Moussallam, R. Vinh Mau, Phys. Rev. Lett. **48** (1982) 1319.
[183] M. Pignone, M. Lacombe, B. Loiseau, R. Vinh Mau, Phys. Rev. C **50** (1994) 2710.
[184] B. El-Bennich, M. Lacombe, B. Loiseau, R. Vinh Mau, Phys. Rev. C **59** (1999) 2313.
[185] R. Schmidt, A. Trzcińska, T. Czosnyka, T. von Egidy, K. Gulda, F.J. Hartmann, J. Jastrzębski, B. Ketzer, M. Kisieliński, B. Kłos, W. Kurcewicz, P. Lubiński, P. Napiorkowski, L. Pieńkowski, R. Smolańczuk, E. Widmann, S. Wycech, Phys. Rev. C **67** (2003) 044308.
[186] B. Kłos, S. Wycech, A. Trzcińska, J. Jastrzębski, T. Czosnyka, M. Kisieliński, P. Lubiński, P. Napiorkowski, L. Pieńkowski, F.J. Hartmann, B. Ketzer, R. Schmidt, T. von Egidy, J. Cugnon, K. Gulda, W. Kurcewicz, E. Widmann, Phys. Rev. C **69** (2004) 044311.
[187] J. Jastrzębski, H. Daniel, T. von Egidy, A. Grabowska, Y.S. Kim, W. Kurcewicz, P. Lubiński, G. Riepe, W. Schmid, A. Stolarz, W. Wycech, Nucl. Phys. A **558** (1993) 405c.
[188] S. Wycech, Nucl. Phys. A **692** (2001) 29c.
[189] S. Wycech, F.J. Hartmann, J. Jastrzębski, B. Kłos, A. Trzcińska, T. von Egidy,

arXiv:nucl-th/0702029.
[190] B. Kłos, A. Trzcińska, J. Jastrzębski, T. Czosnyka, M. Kisieliński, P. Lubiński, P. Napiorkowski, L. Pieńkowski, F.J. Hartmann, B. Ketzer, P. Ring, R. Schmidt, T. von Egidy, R. Smolańczuk, S. Wycech, K. Gulda, W. Kurcewicz, E. Widmann, B.A. Brown, arXiv:nucl-ex/0702016.
[191] S. Wycech, J. Skalski, R. Smolańczuk, J. Dobaczewski, J. Rook, Phys. Rev. C **54** (1996) 1832.
[192] C.C. Batty, E. Friedman, J. Lichtenstadt, Phys. Lett. B **142** (1984) 241.
[193] A. Gal, E. Friedman, C.J. Batty, Phys. Lett. B **491** (2000) 219.
[194] C.J. Batty, E. Friedman, A. Gal, Nucl. Phys. A **689** (2001) 721.
[195] B. Loiseau, S. Wycech, Phys. Rev. C **72** (2005) 011001(R).
[196] S. Wycech, B. Loiseau, AIP Conf. Proc. **796** (2005) 131 (LEAP05).
[197] C.B. Dover, A. Gal, Prog. Part. Nucl. Phys. **12** (1984) 171.
[198] Th.A. Rijken, Y. Yamamoto, Phys. Rev. C **73** (2006) 044008.
[199] C.J. Batty, Phys. Lett. **87B** (1979) 324.
[200] C.J. Batty, A. Gal, G. Toker, Nucl. Phys. A **402** (1983) 349.
[201] C.B. Dover, D.J. Millener, A. Gal, Phys. Rep. **184** (1989) 1.
[202] S. Bart, R.E. Chrien, W.A. Franklin, T. Fukuda, R.S. Hayano, K. Hicks, E.V. Hungerford, R. Michael, T. Miyachi, T. Nagae, J. Nakano, W. Naing, K. Omata, R. Sawafta, Y. Shimizu, L. Tang, S.W. Wissink, Phys. Rev. Lett. **83** (1999) 5238.
[203] J. Dabrowski, Phys. Rev. C **60** (1999) 025205.
[204] H. Noumi, P.K. Saha, D. Abe, S. Ajimura, K. Aoki, H.C. Bhang, T. Endo, Y. Fujii, T. Fukuda, H.C. Guo, K. Imai, O. Hashimoto, H. Hotchi, E.H. Kim, J.H. Kim, T. Kishimoto, A. Krutenkova, K. Maeda, T. Nagae, M. Nakamura, H. Outa, M. Sekimoto, T. Saito, A. Sakaguchi, Y. Sato, R. Sawafta, Y. Shimizu, T. Takahashi, L. Tang, H. Tamura, K. Tanida, T. Watanabe, H.H. Xia, S.H. Zhou, L.H. Zhu, X.F. Zhu, Phys. Rev. Lett. **89** (2002) 072301; ibid. **90** (2003) 049902(E).
[205] R.J. Powers, M. Eckhause, P.P. Guss, A.D. Hancock, D.W. Hertzog, D. Joyce, J.R. Kane, W.C. Phillips, W.F. Vulcan, R.E. Welsh, R.J. Whyley, R.G. Winter, E. Austin, G.W. Dodson, J.P. Miller, F. O'Brien, B.L. Roberts, D.R. Tieger, R.B. Sutton, R. Kunselman, Phys. Rev. C **47** (1993) 1263.
[206] C.J. Batty, E. Friedman, A. Gal, Phys. Lett. B **335** (1994) 273.
[207] C.J. Batty, E. Friedman, A. Gal, Prog. Theor. Phys. Suppl. **117** (1994) 227.
[208] J. Mareš, E. Friedman, A. Gal, B.K. Jennings, Nucl. Phys. A **594** (1995) 311.
[209] S. Balberg, A. Gal, Nucl. Phys. A **625** (1997) 435.
[210] J. Haidenbauer, Ulf-G. Meissner, Phys. Rev. C **72** (2005) 044005.
[211] M. Kohno, Y. Fujiwara, T. Fujita, C. Nakamoto, Y. Suzuki, Nucl. Phys. A **674** (2000) 229.
[212] N. Kaiser, Phys. Rev. C **71** (2005) 068201.
[213] R.S. Hayano, T. Ishikawa, M. Iwasaki, H. Outa, E. Takada, H. Tamura, A. Sakaguchi, M. Aoki, T. Yamazaki, Phys. Lett. B **231** (1989) 355.
[214] T. Harada, S. Shinmura, Y. Akaishi, H. Tanaka, Nucl. Phys. A **507** (1990) 715.
[215] T. Nagae, T. Miyachi, T. Fukuda, H. Outa, T. Tamagawa, J. Nakano, R.S. Hayano, H. Tamura, Y. Shimizu, K. Kubota, R.E. Chrien, R. Sutter, A. Rusek, W.J. Briscoe, R. Sawafta, E.V. Hungerford, A. Empl, W. Naing, C. Neerman, K. Johnston, M. Planinic, Phys. Rev. Lett. **80** (1998) 1605.
[216] T. Harada, Phys. Rev. Lett. **81** (1998) 5287.

[217] M. Kohno, Y. Fujiwara, Y. Watanabe, K. Ogata, M. Kawai, Prog. Theor. Phys. **112** (2004) 895.
[218] M. Kohno, Y. Fujiwara, Y. Watanabe, K. Ogata, M. Kawai, Phys. Rev. C **74** (2006) 064613.
[219] T. Harada, Y. Hirabayashi, Nucl. Phys. A **759** (2005) 143.
[220] T. Harada, Y. Hirabayashi, Nucl. Phys. A **767** (2006) 206.
[221] C.J. Batty, E. Friedman, A. Gal, Phys. Rev. C **59** (1999) 295.
[222] D. Zhu, C.B. Dover, A. Gal, M. May, Phys. Rev. Lett. **67** (1991) 2268.
[223] I. Kumagai-Fuse, T. Koike, Y. Akaishi, Nucl. Phys. A **585** (1995) 367c.
[224] T. Yamada, K. Ikeda, Phys. Rev. C **56** (1997) 3216.
[225] P. Khaustov, et al. [BNL E885 Collaboration], Phys. Rev. C **61** (2000) 027601.
[226] H. Takahashi, J.K. Ahn, H. Akikawa, S. Aoki, K. Arai, S.Y. Bahk, K.M. Baik, B. Bassaleck, J.H. Chung, M.S. Chung, D.H. Davis, T. Fukuda, K. Hoshino, A. Ichikawa, M. Ieiri, K. Imai, Y.H. Iwata, Y.S. Iwata, H. Kanda, M. Kaneko, T. Kawai, M. Kawasaki, C.O. Kim, J.Y. Kim, S.J. Kim, S.H. Kim, Y. Kondo, T. Kouketsu, Y.L. Lee, J.W.C. McNabb, M. Mitsuhara, Y. Nagase, C. Nagoshi, K. Nakasawa, H. Noumi, S. Ogawa, H. Okabe, K. Oyama, H.M. Park, I.G. Park, J. Parker, Y.S. Ra, J.T. Rhee, A. Rusek, H. Shibuya, K.S. Sim, P.K. Saha, D. Seki, M. Sekimoto, J.S. Song, T. Takahashi, F. Takeutchi, H. Tanaka, K. Tanida, J. Tojo, H. Torii, S. Torikai, D.N. Tovee, N. Ushida, K. Yamamoto, N. Yasuda, J.T. Yang, C.J. Yoon, C.S Yoon, M. Yosoi, T. Yoshida, L. Zhu, Phys. Rev. Lett. **87** (2001) 212502.
[227] J.K. Ahn, S. Ajimura, H. Akikawa, B. Bassaleck, A. Berdoz, D. Carman, R.E. Chrien, C.A. Davis, P. Eugenio, H. Fischer, G.B. Franklin, J. Franz, T. Fukuda, L. Gan, H. Hotchi, A. Ichikawa, K. Imai, S.H. Kahana, P. Khaustov, T. Kishimoto, P. Koran, H. Kohri, A. Kourepin, K. Kubota, M. Landry, M. May, C. Meyer, Z. Meziani, S. Minami, T. Miyachi, T. Nagae, J. Nakano, H. Outa, K. Paschke, P. Pile, M. Prokhabatilov, B.P. Quinn, V. Rasin, A. Rusek, H. Schmitt, R.A. Schumacher, M. Sekimoto, K. Sileev, Y. Shimizu, R. Sutter, T. Tamagawa, L. Tang, K. Tanida, K. Yamamoto, L. Yuan, Phys. Rev. Lett. **87** (2001) 132504.
[228] F. Merrill, et al. [BNL E813 Collaboration], Phys. Rev. C **63** (2001) 035206.
[229] J.K. Ahn, et al. [KEK E224 Collaboration], Phys. Lett. B **378** (1996) 53.
[230] S. Aoki, et al. [KEK E176 Collaboration], Prog. Theor. Phys. **85** (1991) 1287.
[231] C.B. Dover, D.J. Millener, A. Gal, D.H. Davis, Phys. Rev. C **44** (1991) 1905.
[232] S. Aoki, et al. [KEK E176 Collaboration], Prog. Theor. Phys. **89** (1993) 493.
[233] S. Aoki, et al. [KEK E176 Collaboration], Phys. Lett. B **355** (1995) 45.
[234] C.B. Dover, A. Gal, Ann. Phys. [NY] **146** (1983) 309.
[235] M.M. Nagels, T.A. Rijken, J.J. de Swart, Phys. Rev. D **15** (1977) 2547.
[236] M.M. Nagels, T.A. Rijken, J.J. de Swart, Phys. Rev. D **20** (1979) 1633.
[237] Y. Yamamoto, T. Motoba, H. Himeno, K. Ikeda, S. Nagata, Prog. Theor. Phys. Suppl. **117** (1994) 361.
[238] Y. Yamamoto, in *Nuclear and Particle Physics with Meson Beams in the 1 GeV/c Region*, edited by S. Sugimoto and O. Hashimoto (Universal Academy Press, Inc. Tokyo, 1995), p. 267.
[239] Y. Yamamoto, Few-Body Syst. Suppl. **9** (1995) 145.
[240] T. Fukuda, et al. [KEK E224 Collaboration], Phys. Rev. C **58** (1998) 1306.
[241] P. Khaustov, et al. [BNL E885 Collaboration], Phys. Rev. C **61** (2000) 054603.
[242] V.G.J. Stoks, Th.A. Rijken, Phys. Rev. C **59** (1999) 3009.
[243] I.N. Filikhin, A. Gal, Phys. Rev. C **65** (2002) 041001.

[244] I.N. Filikhin, A. Gal, Nucl. Phys. A **707** (2002) 491.
[245] Th.A. Rijken, Y. Yamamoto, arXiv:nucl-th/0608074.
[246] Y. Fujiwara, Y. Suzuki, C. Nakamoto, Prog. Part. Nucl. Phys. **58** (2007) 439, and references cited therein.
[247] Y. Fujiwara, M. Kohno, Y. Suzuki, Nucl. Phys. A **784** (2007) 161.
[248] D.J. Millener, C.B. Dover, A. Gal, Prog. Theor. Phys. Suppl. **117** (1994) 307.
[249] C.B. Dover, A. Gal, D.J. Millener, Nucl. Phys. A **572** (1994) 85.
[250] K. Ikeda, T. Fukuda, T. Motoba, M. Takahashi, Y. Yamamoto, Prog. Theor. Phys. **91** (1994) 747.
[251] Y. Yamamoto, T. Motoba, T. Fukuda, M. Takahashi, K. Ikeda, Prog. Theor. Phys. Suppl. **117** (1994) 281.
[252] J. Schaffner-Bielich, A. Gal, Phys. Rev. C **62** (2000) 034311, and references cited therein.
[253] T. Nagae, in *Topics in Strangeness Nuclear Physics*, Eds. P. Bydzovsky, A. Gal and J. Mares, Lecture Notes in Physics **724** (Springer, Heidelberg, 2007).
[254] J. Pochodzalla, Nucl. Phys. A **754** (2005) 430c.
[255] F. Ferro, M. Agnello, F. Iazzi, K. Szymańska, Nucl. Phys. A **789** (2007) 209.
[256] E. Friedman, Nucl. Phys. A **639** (1998) 511c.